

The Vera C. Rubin Observatory Data Preview 1

VERA C. RUBIN OBSERVATORY TEAM,¹ TATIANA ACERO-CUELLAR ,² EMILY ACOSTA ,¹ CHRISTINA L. ADAIR ,³
PRAKRUTH ADARI ,⁴ JENNIFER K. ADELMAN-MCCARTHY ,⁵ ANASTASIA ALEXOV ,¹ RUSS ALLBERRY ,¹
ROBYN ALLSMAN,¹ YUSRA ALSAYYAD ,⁶ JHONATAN AMADO ,⁵ NATHAN AMOUROUX ,⁷ PIERRE ANTILOGUS,⁸
ALEXIS ARACENA ALCAYAGA,⁹ GONZALO ARAVENA-ROJAS ,⁹ CLAUDIO H. ARAYA CORTES,⁹ ÉRIC AUBOURG ,¹⁰
TIM S. AXELROD ,¹¹ JOHN BANOVETZ ,¹² CARLOS BARRÍA,⁹ AMANDA E. BAUER ,¹³ BRIAN J. BAUMAN,¹⁴
ELLEN BECHTOL ,¹⁵ KEITH BECHTOL ,¹⁶ ANDREW C. BECKER ,¹⁷ VALERIE R. BECKER ,¹⁸ MARK G. BECKETT ,¹⁹
ERIC C. BELL ,²⁰ PEDRO H. BERNARDINELLI ,²¹ FEDERICA B. BIANCO ,^{2,22,23} ROBERT D. BLUM ,¹⁸
JOANNE BOGART,²⁴ ADAM BOLTON ,³ MICHAEL T. BOOTH,¹ JAMES F. BOSCH ,⁶ ALEXANDRE BOUCAUD ,²⁵
DOMINIQUE BOUTIGNY ,⁷ ROBERT A. BOVILL,¹ ANDREW BRADSHAW,^{3,24} JOHAN BREGEON ,²⁶ BRIAN J. BRONDEL ,²⁷
ALEX BROUGHTON ,²⁴ AUDREY BUDLONG,²⁸ DIMITRI BUFFAT,²⁶ RODOLFO CANESTRARI ,²⁹ NEVEN CAPLAR ,²⁰
JEFFREY L. CARLIN ,¹ ROSS CEBALLO ,¹⁸ COLIN ORION CHANDLER ,^{30,20,31} CHIHWAY CHANG ,³²
GLENAYER CHARLES-EMERSON,¹ HSIN-FANG CHIANG ,³ JAMES CHIANG ,²⁴ YUMI CHOI ,³³ ERIC J. CHRISTENSEN,⁹
CHARLES F. CLAVER,¹ ANDY W. CLEMENTS,¹ JOSEPH J. COCKRUM,¹ FRANCO COLLEONI,⁹ CÉLINE COMBET ,²⁶
ANDREW J. CONNOLLY ,²¹ JULIO EDUARDO CONSTANZO CÓRDOVA ,⁹ HANS E CONTRERAS,⁹
JOHN FRANKLIN CRENSHAW ,²¹ SYLVIE DAGORET-CAMPAGNE ,³⁴ SCOTT F. DANIEL,²⁰ FELIPE DARUICH,⁹
GUILLAUME DAUBARD ,⁸ GREG DAUES,³⁵ ERIK DENNHY ,¹ STEPHANIE JH DEPPE ,¹⁸ SETH W. DIGEL ,³
PETER E. DOHERTY,³⁶ ALEX DRLICA-WAGNER ,⁵ GREGORY P. DUBOIS-FELSMANN ,³⁷ FROSSIE ECONOMOU ,¹
ORION EIGER ,^{3,24} LUKAS EISERT ,³ ALAN M. EISNER ,³⁸ ANTHONY ENGLERT ,³⁹ BADEN ERB,⁹ JUAN A. FABREGA,⁹
PARKER FAGRELIUS,¹ KEVIN FANNING ,³ ANGELO FAUSTI NETO ,¹ PETER S. FERGUSON ,^{21,16} AGNÈS FERTÉ ,³
MERLIN FISHER-LEVINE ,⁴⁰ GLORIA FONSECA ALVAREZ ,³³ MICHAEL D. FOSS,³ DOMINIQUE FOUCHEZ ,⁴¹
DAN C. FUCHS ,³ EMMANUEL GANGLER ,⁴² IGOR GAPONENKO,³ JULEN GARCIA ,⁴³ JOHN H. GATES,³
RANPAL K. GILL ,²⁷ ENRICO GIRO ,⁴⁴ THOMAS GLANZMAN ,³ ROBINSON GODOY,⁹ IAIN GOODENOW,¹
MIRANDA R. GORSUCH ,¹⁶ MICHELLE GOWER ,³⁵ MIKAEL GRANVIK ,^{45,46} SARAH GREENSTREET ,³³ WEN GUAN ,¹²
THIBAULT GUILLEMIN ,⁷ LEANNE P. GUY ,⁹ DIANE HASCALL,³ AREN NATHANIEL HEINZE ,²¹ FABIO HERNANDEZ ,⁴⁷
KENNETH HERNER ,⁵ ARDIS HERROLD,¹ CLARE R. HIGGS ,¹⁸ JOSHUA HOBLITT ,¹ ERIN LEIGH HOWARD ,²⁰
MINHEE HYUN ,⁹ PATRICK INGRAHAM ,¹¹ DAVID H. IRVING ,¹⁸ ŽELJKO IVEŽIĆ ,^{1,20} SUZANNE H. JACOBY,¹
BUELL T. JANNUZI ,⁴⁸ SREEVANI JARUGULA ,⁵ M. JAMES JEE ,^{49,50} TIM JENNESS ,¹ TOBY C. JENNINGS ,³
ANDREA JEREMIE ,⁷ GARRETT JERNIGAN,^{51,*} DAVID JIMÉNEZ MEJÍAS,⁹ ANTHONY S. JOHNSON ,³ R. LYNNE JONES ,²⁰
ROGER WILLIAM LEWIS JONES ,⁵² CLAIRE JURAMY-GILLES ,⁸ MARIO JURIĆ ,²¹ STEVEN M. KAHN ,⁵³
J. BRYCE KALMBACH ,³ YIJUNG KANG ,^{24,9} ARUN KANNAWADI ,^{54,6} JEFFREY P. KANTOR,¹ EDWARD KARAVAKIS ,¹²
KSHITIJA KELKAR ,⁹ LEE S. KELVIN ,⁶ IVAN V. KOTOV,¹² GÁBOR KOVÁCS ,²¹ MIKOŁAJ KOWALIK ,³⁵
VICTOR L. KRABBENDAM,¹ K. SIMON KRUGHOFF ,^{1,*} PETR KUBÁNEK ,⁹ JACOB A. KURLANDER ,²¹ MILE KUSULJA,²⁶
CRAIG S. LAGE ,⁵⁰ P. J. A. LAGO ,²⁷ KATHERINE LALIOTIS ,⁵⁵ TRAVIS LANGE ,³ DIDIER LAPORTE,⁸
RYAN M. LAU ,³³ JUAN CARLOS LAZARTE,³ QUENTIN LE BOULC'H ,⁴⁷ PIERRE-FRANÇOIS LÉGET ,⁶
LAURENT LE GUILLOU ,⁸ BENJAMIN LEVINE ,⁴ MING LIANG,¹ SHUANG LIANG,³ KIAN-TAT LIM ,³
ANJA VON DER LINDEM ,⁴ HUAN LIN ,⁵ MARGAUX LOPEZ ,³ JUAN J. LOPEZ TORO,⁹ PETER LOVE,⁵²
ROBERT H. LUPTON ,⁶ NATE B. LUST ,⁶ LAUREN A. MACARTHUR ,⁶ SEAN PATRICK MACBRIDE ,⁵⁶
GREG M. MADEJSKI,²⁴ GABRIELE MAINETTI ,⁴⁷ STEVEN J. MARGHEIM ,²⁷ THOMAS W. MARKIEWICZ ,³
PHIL MARSHALL ,³ STUART MARSHALL,²⁴ GUIDO MAULEN,⁹ MORGAN MAY,^{57,12} JEREMY MCCORMICK ,³
DAVID MCKAY ,⁵⁸ ROBERT MCKERCHER,¹ GUILLEM MEGIAS HOMAR ,^{59,24} AARON M. MEISNER ,³³
FELIPE MENANTEAU,³⁵ HEATHER R. MENTZER ,³⁸ KRISTEN METZGER,¹⁸ JOSHUA E. MEYERS ,²⁴ MICHELLE MILLER,³³
DAVID J. MILLS,¹ JOACHIM MOEYENS ,²¹ MARC MONIEZ,³⁴ FRED E. MOOLEKAMP ,⁶⁰ C. A. L. MORALES MARÍN ,⁹
FRITZ MUELLER ,³ JAMES R. MULLANEY ,⁶¹ FREDDY MUÑOZ ARANCIBIA,¹ KATE NAPIER ,²⁴ HOMER NEAL,³
ERIC H. NEILSEN, JR. ,⁵ JEREMY NEVEU ,³⁴ TIMOTHY NOBLE,⁶² ERFAN NOURBAKHS ,⁶ KNUT OLSEN ,³³
WILLIAM O'MULLANE ,⁹ DMITRY ONOPRIENKO,³ MARCO ORIUNNO ,³ SHAWN OSIER,³ RUSSELL E. OWEN,²⁰
AASHAY PAI ,³² JOHN K. PAREJKO ,²⁰ HYE YUN PARK ,⁵⁴ JAMES B. PARSONS,^{35,*} MARIA T. PATTERSON ,²⁰
MARINA S. PAVLOVIC ,⁹ KARLA PEÑA RAMÍREZ ,⁹ JOHN R. PETERSON ,⁶³ STEPHEN R. PIETROWICZ ,³⁵
ANDRÉS A. PLAZAS MALAGÓN ,^{3,24} REBEKAH POLEN,⁵⁴ HANNAH MARY MARGARET POLLEK,³ PAUL A. PRICE ,⁶

50 BRUNO C. QUINT ,¹ JOSÉ MIGUEL QUINTERO MARIN,⁹ MARKUS RABUS ,⁶⁴ BENJAMIN RACINE ,⁴¹ VELJKO RADEKA,¹²
 51 MANON RAMEL,²⁶ ARIANNA RANABHAT ,⁶⁵ ANDREW P. RASMUSSEN ,²⁴ DAVID A. RATHFELDER,⁶⁶
 52 MEREDITH L. RAWLS ,^{20,21} SOPHIE L. REED ,⁶ KEVIN A. REIL ,³ DAVID J. REISS,²⁰ MICHAEL A. REUTER ,¹
 53 TIAGO RIBEIRO ,¹ MICKAEL RIGAULT ,⁶⁷ VINCENT J. RIOT ,¹⁴ STEVEN M. RITZ ,³⁸ MARIO F. RIVERA,⁹
 54 BRANT E. ROBERTSON ,³⁸ WILLIAM ROBY ,³⁷ GABRIELE RODEGHIERO ,⁶⁸ AARON ROODMAN ,²⁴
 55 LUCA ROSIGNOLI ,^{69,68} CÉCILE ROUCELLE ,²⁵ MATTHEW R. RUMORE ,¹² STEFANO RUSSO,⁸ ELI S. RYKOFF ,²⁴
 56 ANDREI SALNIKOV ,³ BRUNO O. SÁNCHEZ ,⁴¹ DAVID SANMARTIM ,⁹ CLARE SAUNDERS ,⁶ RAFE H. SCHINDLER,²⁴
 57 SAMUEL J. SCHMIDT ,⁵⁰ JACQUES SEBAG,⁹ BRIAN SELVY,¹ EDGARD ESTEBAN SEPULVEDA VALENZUELA,⁹
 58 GONZALO SERICHE ,⁹ JACQUELINE C. SERON-NAVARRETE ,⁹ IGNACIO SEVILLA-NOARBE ,⁷⁰ ALYSHA SHUGART ,⁹
 59 JONATHAN SICK ,^{71,1} CRISTIÁN SILVA ,⁹ MATHEW C. SIMS ,⁷² JALADH SINGHAL ,³⁷ KEVIN BENJAMIN SIRUNO,⁹
 60 COLIN T. SLATER ,²⁰ BRIANNA M. SMART ,²⁰ ADAM SNYDER ,⁵⁰ CHRISTINE SOLDAHL,³
 61 IOANA SOTUELA ELORRIAGA ,⁹ BRIAN STALDER ,¹ HERNAN STOCKEBRAND ,⁹ ALAN L. STRAUSS ,¹⁸
 62 MICHAEL A. STRAUSS ,⁶ KRZYSZTOF SUBERLAK ,²⁰ IAN S. SULLIVAN ,²⁰ JOHN D. SWINBANK ,^{73,6} DIEGO TAPIA ,⁹
 63 ALESSIO TARANTO ,^{68,69} DAN S. TARANU ,⁶ JOHN GREGG THAYER ,³ SANDRINE THOMAS ,¹
 64 ADAM J. THORNTON ,¹ ROBERTO TIGHE,⁹ LAURA TORIBIO SAN CIPRIANO,⁷⁰ TE-WEI TSAI ,¹ DOUGLAS L. TUCKER ,⁵
 65 MAX TURRI,³ J. ANTHONY TYSON ,⁵⁰ ELANA K. URBACH ,⁷⁴ YOUSUKE UTSUMI ,⁷⁵ BRIAN VAN KLAVEREN,³
 66 WOUTER VAN REEVEN ,⁹ PETER ANTHONY VAUCHER ,³ PAULINA VENEGAS,⁹ APRAJITA VERMA ,⁷⁶
 67 ANTONIA SIERRA VILLARREAL ,³ STELIOS VOUTSINAS ,¹ CHRISTOPHER W. WALTER ,⁵⁴ YUANKUN (DAVID) WANG ,²¹
 68 CHRISTOPHER Z. WATERS ,⁶ CHRISTINA C. WILLIAMS ,³³ BETH WILLMAN ,⁷⁷ MATTHIAS WITTGEN ,³
 69 W. M. WOOD-VASEY ,⁷⁸ WEI YANG ,³ ZHAOYU YANG ,¹² BRIAN P. YANNY ,⁵ PETER YOACHIM ,²⁰
 70 TIANQING ZHANG ,⁷⁸ AND CONGHAO ZHOU ,³⁸

¹ *Vera C. Rubin Observatory Project Office, 950 N. Cherry Ave., Tucson, AZ 85719, USA*

² *Department of Physics and Astronomy, University of Delaware, Newark, DE 19716-2570, USA*

³ *SLAC National Accelerator Laboratory, 2575 Sand Hill Rd., Menlo Park, CA 94025, USA*

⁴ *Department of Physics and Astronomy, Stony Brook University, Stony Brook, NY 11794, USA*

⁵ *Fermi National Accelerator Laboratory, P. O. Box 500, Batavia, IL 60510, USA*

⁶ *Department of Astrophysical Sciences, Princeton University, Princeton, NJ 08544, USA*

⁷ *Université Savoie Mont-Blanc, CNRS/IN2P3, LAPP, 9 Chemin de Bellevue, F-74940 Annecy-le-Vieux, France*

⁸ *Sorbonne Université, Université Paris Cité, CNRS/IN2P3, LPNHE, 4 place Jussieu, F-75005 Paris, France*

⁹ *Vera C. Rubin Observatory, Avenida Juan Cisternas #1500, La Serena, Chile*

¹⁰ *Université Paris Cité, CNRS/IN2P3, CEA, APC, 4 rue Elsa Morante, F-75013 Paris, France*

¹¹ *Steward Observatory, The University of Arizona, 933 N. Cherry Ave., Tucson, AZ 85721, USA*

¹² *Brookhaven National Laboratory, Upton, NY 11973, USA*

¹³ *Yerkes Observatory, 373 W. Geneva St., Williams Bay, WI 53191, USA*

¹⁴ *Lawrence Livermore National Laboratory, 7000 East Avenue, Livermore, CA 94550, USA*

¹⁵ *Wisconsin IceCube Particle Astrophysics Center, University of Wisconsin—Madison, Madison, WI 53706, USA*

¹⁶ *Department of Physics, University of Wisconsin-Madison, Madison, WI 53706, USA*

¹⁷ *Amazon Web Services, Seattle, WA 98121, USA*

¹⁸ *Vera C. Rubin Observatory/NSF NOIRLab, 950 N. Cherry Ave., Tucson, AZ 85719, USA*

¹⁹ *Institute for Astronomy, University of Edinburgh, Royal Observatory, Blackford Hill, Edinburgh EH9 3HJ, UK*

²⁰ *University of Washington, Dept. of Astronomy, Box 351580, Seattle, WA 98195, USA*

²¹ *Institute for Data-intensive Research in Astrophysics and Cosmology, University of Washington, 3910 15th Avenue NE, Seattle, WA 98195, USA*

²² *Joseph R. Biden, Jr., School of Public Policy and Administration, University of Delaware, Newark, DE 19717 USA*

²³ *Data Science Institute, University of Delaware, Newark, DE 19717 USA*

²⁴ *Kavli Institute for Particle Astrophysics and Cosmology, SLAC National Accelerator Laboratory, 2575 Sand Hill Rd., Menlo Park, CA 94025, USA*

²⁵ *Université Paris Cité, CNRS/IN2P3, APC, 4 rue Elsa Morante, F-75013 Paris, France*

²⁶ *Université Grenoble Alpes, CNRS/IN2P3, LPSC, 53 avenue des Martyrs, F-38026 Grenoble, France*

²⁷ *Vera C. Rubin Observatory/NSF NOIRLab, Casilla 603, La Serena, Chile*

²⁸ *University of Washington, Dept. of Physics, Box 351580, Seattle, WA 98195, USA*

²⁹ *INAF Istituto di Astrofisica Spaziale e Fisica Cosmica di Palermo, Via Ugo la Malfa 153, 90146, Palermo, Italy*

³⁰ *LSST Interdisciplinary Network for Collaboration and Computing, Tucson, USA*

³¹ *Department of Astronomy and Planetary Science, Northern Arizona University, P.O. Box 6010, Flagstaff, AZ 86011, USA*

³² *Department of Astronomy and Astrophysics, University of Chicago, 5640 South Ellis Avenue, Chicago, IL 60637, USA*

³³ *NSF NOIRLab, 950 N. Cherry Ave., Tucson, AZ 85719, USA*

106 ³⁴Université Paris-Saclay, CNRS/IN2P3, IJCLab, 15 Rue Georges Clemenceau, F-91405 Orsay, France
 107 ³⁵NCSA, University of Illinois at Urbana-Champaign, 1205 W. Clark St., Urbana, IL 61801, USA
 108 ³⁶Smithsonian Astrophysical Observatory, 60 Garden St., Cambridge MA 02138, USA
 109 ³⁷Caltech/IPAC, California Institute of Technology, MS 100-22, Pasadena, CA 91125-2200, USA

110 ³⁸Santa Cruz Institute for Particle Physics and Physics Department, University of California-Santa Cruz, 1156 High St., Santa Cruz,
 111 CA 95064, USA

112 ³⁹Department of Physics, Brown University, 182 Hope Street, Providence, RI 02912, USA

113 ⁴⁰D4D CONSULTING LTD., Suite 1 Second Floor, Everdene House, Deansleigh Road, Bournemouth, UK BH7 7DU

114 ⁴¹Aix Marseille Université, CNRS/IN2P3, CPPM, 163 avenue de Luminy, F-13288 Marseille, France

115 ⁴²Université Clermont Auvergne, CNRS/IN2P3, LPCA, 4 Avenue Blaise Pascal, F-63000 Clermont-Ferrand, France

116 ⁴³C. Iñaki Goenaga, 5, 20600, Guipúzcoa, Spain

117 ⁴⁴INAF Osservatorio Astronomico di Trieste, Via Giovan Battista Tiepolo 11, 34143, Trieste, Italy

118 ⁴⁵Department of Physics, P.O. Box 64, 00014 University of Helsinki, Finland

119 ⁴⁶Asteroid Engineering Laboratory, Luleå University of Technology, Box 848, SE-981 28 Kiruna, Sweden

120 ⁴⁷CNRS/IN2P3, CC-IN2P3, 21 avenue Pierre de Coubertin, F-69627 Villeurbanne, France

121 ⁴⁸University of Arizona, Department of Astronomy and Steward Observatory, 933 N. Cherry Ave, Tucson, AZ 85721, USA

122 ⁴⁹Department of Astronomy, Yonsei University, 50 Yonsei-ro, Seoul 03722, Republic of Korea

123 ⁵⁰Physics Department, University of California, One Shields Avenue, Davis, CA 95616, USA

124 ⁵¹Space Sciences Lab, University of California, 7 Gauss Way, Berkeley, CA 94720-7450, USA

125 ⁵²Lancaster University, Lancaster, UK

126 ⁵³Physics Department, University of California, 366 Physics North, MC 7300 Berkeley, CA 94720, USA

127 ⁵⁴Department of Physics, Duke University, Durham, NC 27708, USA

128 ⁵⁵Center for Cosmology and Astro-Particle Physics, The Ohio State University, Columbus, OH 43210, USA

129 ⁵⁶Physik-Institut, University of Zurich, Winterthurerstrasse 190, 8057 Zurich, Switzerland

130 ⁵⁷Department of Physics Columbia University, New York, NY 10027, USA

131 ⁵⁸EPCC, University of Edinburgh, 47 Potterrow, Edinburgh, EH8 9BT, UK

132 ⁵⁹Department of Aeronautics and Astronautics, Stanford University, Stanford, CA 94305, USA

133 ⁶⁰soZen Inc., 105 Clearview Dr, Penfield, NY 14526

134 ⁶¹Astrophysics Research Cluster, School of Mathematical and Physical Sciences, University of Sheffield, Sheffield, S3 7RH, United
 135 Kingdom

136 ⁶²Science and Technology Facilities Council, Rutherford Appleton Laboratory, Harwell, UK

137 ⁶³Department of Physics and Astronomy, Purdue University, 525 Northwestern Ave., West Lafayette, IN 47907, USA

138 ⁶⁴Departamento de Matemática y Física Aplicadas, Facultad de Ingeniería, Universidad Católica de la Santísima Concepción, Alonso de
 139 Rivera 2850, Concepción, Chile

140 ⁶⁵Australian Astronomical Optics, Macquarie University, North Ryde, NSW, Australia

141 ⁶⁶AURA, 950 N. Cherry Ave., Tucson, AZ 85719, USA

142 ⁶⁷Université Claude Bernard Lyon 1, CNRS/IN2P3, IP2I, 4 Rue Enrico Fermi, F-69622 Villeurbanne, France

143 ⁶⁸INAF Osservatorio di Astrofisica e Scienza dello Spazio Bologna, Via P. Gobetti 93/3, 40129, Bologna, Italy

144 ⁶⁹Department of Physics and Astronomy (DIFA), University of Bologna, Via P. Gobetti 93/2, 40129, Bologna, Italy

145 ⁷⁰Centro de Investigaciones Energéticas, Medioambientales y Tecnológicas, Av. Complutense 40, 28040 Madrid, Spain

146 ⁷¹J.Sick Codes Inc., Penetanguishene, Ontario, Canada

147 ⁷²Science and Technology Facilities Council, UK Research and Innovation, Polaris House, North Star Avenue, Swindon, SN2 1SZ, UK

148 ⁷³ASTRON, Oude Hoogeveensedijk 4, 7991 PD, Dwingeloo, The Netherlands

149 ⁷⁴Department of Physics, Harvard University, 17 Oxford St., Cambridge MA 02138, USA

150 ⁷⁵National Astronomical Observatory of Japan, Chile Observatory, Los Abedules 3085, Vitacura, Santiago, Chile

151 ⁷⁶Department of Physics, University of Oxford, Denys Wilkinson Building, Keble Road, Oxford, OX1 3RH, UK

152 ⁷⁷LSST Discovery Alliance, 933 N. Cherry Ave., Tucson, AZ 85719, USA

153 ⁷⁸Department of Physics and Astronomy, University of Pittsburgh, 3941 O'Hara Street, Pittsburgh, PA 15260, USA

154 (Dated: January 13, 2026)

ABSTRACT

155 We present Rubin Data Preview 1 (DP1), the first data from the NSF-DOE Vera C. Rubin Observatory, comprising raw and calibrated single-epoch images, coadds, difference images, detection
 156 catalogs, and ancillary data products. DP1 is based on 1792 optical/near-infrared exposures ac-
 157 quired over 48 distinct nights by the Rubin Commissioning Camera, LSSTComCam, on the Si-

159 Simonyi Survey Telescope at the Summit Facility on Cerro Pachón, Chile in late 2024. DP1 covers
 160 ~ 15 deg 2 distributed across seven roughly equal-sized non-contiguous fields, each independently ob-
 161 served in six broad photometric bands, *ugrizy*. The median FWHM of the point-spread function
 162 across all bands is approximately 1''.14, with the sharpest images reaching about 0''.58. The 5 σ point
 163 source depths for coadded images in the deepest field, Extended Chandra Deep Field South, are:
 164 $u = 24.55, g = 26.18, r = 25.96, i = 25.71, z = 25.07, y = 23.1$. Other fields are no more than 2.2
 165 magnitudes shallower in any band, where they have nonzero coverage. DP1 contains approximately
 166 2.3 million distinct astrophysical objects, of which 1.6 million are extended in at least one band in
 167 coadds, and 431 solar system objects, of which 93 are new discoveries. DP1 is approximately 3.5 TB
 168 in size and is available to Rubin data rights holders via the Rubin Science Platform, a cloud-based
 169 environment for the analysis of petascale astronomical data. While small compared to future LSST
 170 releases, its high quality and diversity of data support a broad range of early science investigations
 171 ahead of full operations in late 2025.

172 *Keywords:* Rubin Observatory – LSST

1. INTRODUCTION

174 The National Science Foundation (NSF)–Department
 175 of Energy (DOE) Vera C. Rubin Observatory is a
 176 ground-based, wide-field optical/near-infrared facility
 177 located on Cerro Pachón in northern Chile. Named in
 178 honor of Vera C. Rubin, a pioneering astronomer whose
 179 groundbreaking work in the 20th century provided the
 180 first convincing evidence for the existence of dark matter
 181 (V. C. Rubin & W. K. Ford 1970; V. C. Rubin et al.
 182 1980), the observatory’s prime mission is to carry out the
 183 Legacy Survey of Space and Time (formerly Large Syn-
 184 optic Survey Telescope) (LSST) (Ž. Ivezić et al. 2019a).
 185 This 10-year survey is designed to obtain rapid-cadence,
 186 multi-band imaging of the entire visible southern sky
 187 approximately every 3–4 nights. Over its main 18,000
 188 deg 2 footprint, the LSST is expected to reach a depth
 189 of ~ 27 magnitude in the r-band, with ~ 800 visits per
 190 pointing in all filters (F. B. Bianco et al. 2022).

191 The Rubin Observatory system consists of four main
 192 components: the Simonyi Survey Telescope, featuring
 193 an 8.4 m diameter (6.5 m effective aperture) primary
 194 mirror that delivers a wide field of view; a 3.2-gigapixel
 195 camera, capable of imaging 9.6 square degrees per ex-
 196 posure⁷⁹ with seeing-limited quality in six broadband
 197 filters, *ugrizy* (320–1050 nm); an automated Data Man-
 198 agement System that processes and archives tens of ter-
 199 abytes of data per night, generating science-ready data
 200 products within minutes for a global community of sci-
 201 entists; and an Education and Public Outreach (EPO)

202 program that provides real-time data access, interactive
 203 tools, and educational content to engage the public. The
 204 integrated system’s étendue⁸⁰ of 319 m 2 deg 2 , is over an
 205 order of magnitude larger than that of any previous op-
 206 tical observatory, enabling a fast, large-scale survey with
 207 exceptional depth in a fraction of the time compared to
 208 other observatories.

209 The observatory’s design is driven by four key science
 210 themes: probing dark energy and dark matter; taking
 211 an inventory of the solar system; exploring the tran-
 212 sient and variable optical sky; and mapping the Milky
 213 Way (Ž. Ivezić et al. 2019a). These themes inform the
 214 optimization of a range of system parameters, includ-
 215 ing image quality, photometric and astrometric accu-
 216 racy, the depth of a single visit and the co-added survey
 217 depth, the filter complement, the total number of visits
 218 per pointing as well as the distribution of visits on the
 219 sky, and total sky coverage. Additionally, they inform
 220 the design of the data processing and access systems.
 221 By optimizing the system parameters to support a wide
 222 range of scientific goals, we maximize the observatory’s
 223 scientific output across all areas, making Rubin a pow-
 224 erful discovery machine capable of addressing a broad
 225 range of astrophysical questions.

226 Throughout the duration of the LSST, Rubin Obser-
 227 vatory will issue a series of Data Releases, each repre-
 228 senting a complete reprocessing of all LSST data col-
 229 lected up to that point. Prior to the start of the LSST
 230 survey, commissioning activities will generate a signifi-
 231 cant volume of science-grade data. To make this early
 232 data available to the community, the Rubin Early Sci-
 233 ence Program (L. P. Guy et al. 2026) was established.

^{*} Author is deceased

⁷⁹ We define an “exposure” as the process of exposing all detectors in the focal plane. It is synonymous with the term “visit” in DP1. By contrast, an “image” is the output of a single detector following an exposure.

⁸⁰ The product of the primary mirror area and the angular area of its field of view for a given set of observing conditions.

234 One key component of this program is a series of Data
 235 Previews; early versions of the [LSST](#) Data Releases.
 236 These previews include preliminary data products de-
 237 rived from both simulated and commissioning data,
 238 which, together with early versions of the data access
 239 services, are intended to support high-impact early sci-
 240 ence, facilitate community readiness, and inform the de-
 241 velopment of Rubin’s operational capabilities ahead of
 242 the start of full survey operations. All data and services
 243 provided through the Rubin Early Science Program are
 244 offered on a shared-risk basis ⁸¹.

245 This paper describes Rubin’s second of three planned
 246 Data Previews: [Data Preview 1 \(DP1\) \(NSF-DOE Vera](#)
 247 [C. Rubin Observatory 2025a\)](#). The first, [Data Preview](#)
 248 [0 \(DP0\)](#)⁸², contained data products produced from the
 249 processing of simulated [LSST](#)-like data sets. These were
 250 released together with a very early version of the Rubin
 251 [Science Platform \(M. Jurić et al. 2019\)](#), which provided
 252 the data access services. [DP0](#) was released in multiple
 253 phases; DP0.1, DP0.2, and DP0.3, each building upon
 254 the previous one and incorporating new data and func-
 255 tionalities. DP0.1 and DP0.2 used data from the cos-
 256 moDC2 simulations ([LSST Dark Energy Science Collab-](#)
 257 [oration \(LSST DESC\) et al. 2021\)](#) prepared by the Dark
 258 Energy Science Collaboration (DESC), whereas DP0.3
 259 is based on simulated datasets from the Solar System
 260 Science Collaboration (SSSC).

261 [DP1](#) contains data products derived from the repro-
 262 cessing of science-grade exposures acquired by the [Ru-](#)
 263 [bin Commissioning Camera \(LSSTComCam\)](#), in late
 264 2024. The third and final Data Preview, [Data Preview](#)
 265 [2 \(DP2\)](#), is planned to be based on a reprocessing of all
 266 science-grade data taken with the Rubin’s [LSST Science](#)
 267 [Camera \(LSSTCam\)](#) during commissioning.

268 All Rubin Data Releases and Previews are subject
 269 to a two-year proprietary period, with immediate ac-
 270 cess granted exclusively to LSST data rights holders ([R.](#)
 271 [Blum & the Rubin Operations Team 2020](#)). Data rights
 272 holders⁸³ are individuals or institutions with formal au-
 273 thorization to access proprietary data collected by the
 274 Vera C. Rubin Observatory. After the two-year propri-
 275 etary period, [DP1](#) will be made public. However, even
 276 once the data become public, access for non-data rights
 277 holders will not be provided through Rubin Data Access
 278 Centers in the US and Chile ([R. Blum & the Rubin Op-](#)

81 Shared risk means early access with caveats: the community benefits from getting a head start on science, preparing analyses, and providing feedback, while also accepting that the system may not work as well as it will during full operations.

82 See <https://dp0.lsst.io>

83 See <https://www.lsst.org/scientists/international-drh-list>

279 [erations Team 2020](#)). Alternative access mechanisms are
 280 still under discussion and have not yet been finalized.

281 In this paper, we describe the contents and valida-
 282 tion of Rubin [DP1](#), the first Data Preview to deliver
 283 data derived from observations conducted by the Vera
 284 C. Rubin Observatory, as well as the data-access mecha-
 285 nisms and community-support services that accompany
 286 it. [DP1](#) is based on the reprocessing of 1792 science-
 287 grade exposures acquired during the first on-sky com-
 288 missioning campaign, conducted over 48 nights between
 289 2024-10-24 and 2024-12-11. It covers a total area of
 290 approximately ~ 15 deg² distributed across seven dis-
 291 tinct non-contiguous fields. The data products include
 292 raw and calibrated single-epoch images, coadded images,
 293 difference images, detection catalogs, and other derived
 294 data products. [DP1](#) is about 3.5 TB in size and con-
 295 tains around 2.3 million distinct astronomical objects,
 296 detected in 2644 coadded images. Full [DP1](#) release doc-
 297 documentation is available at <https://dp1.lsst.io>. Despite
 298 Rubin Observatory still being in commissioning and not
 299 yet complete at the time the observations were acquired,
 300 Rubin [DP1](#) provides an important first look at the data,
 301 showcasing its characteristics and capabilities.

302 The structure of this paper is as follows. In section
 303 [2](#) we describe the observatory system and overall con-
 304 struction and commissioning status at the time of data
 305 acquisition, the seven fields included in [DP1](#), and the
 306 observing strategy used. Section [3](#) summarizes the con-
 307 tents of [DP1](#) and the data products contained in the
 308 release. The data processing pipelines are described in
 309 section [4](#), followed by a description of the data valida-
 310 tion and performance assessment in section [5](#). Section
 311 [6](#) describes the Rubin [Science Platform \(RSP\)](#), a [cloud](#)-
 312 based data science infrastructure that provides tools and
 313 services to Rubin data rights holders to access, visual-
 314 ize and analyze peta-scale data generated by the [LSST](#).
 315 Section [7](#) presents the Rubin Observatory’s model for
 316 community support, which emphasizes self-help via doc-
 317 umentation and tutorials, and employs an open platform
 318 for issue reporting that enables crowd-sourced solutions.
 319 Finally, a summary of the [DP1](#) release and information
 320 on expected future releases of data is given in section [8](#).
 321 The appendix contains a useful glossary of terms used
 322 throughout this paper.

323 All magnitudes quoted are in the AB system ([J. B.](#)
 324 [Oke & J. E. Gunn 1983](#)), unless otherwise specified.

325 2. ON-SKY COMMISSIONING CAMPAIGN

326 The first Rubin on-sky commissioning campaign was
 327 conducted using the [LSSTComCam](#). The campaign’s
 328 primary objective was to optically align the Simonyi
 329 Survey Telescope and verify its ability to deliver accept-

able image quality using **LSSTComCam**. In addition, the campaign provided valuable operations experience to facilitate commissioning the full **LSSTCam** (T. Lange et al. 2024; A. Roodman et al. 2024). We note that commissioning **LSSTComCam** was not an objective of the campaign. Instead, **LSSTComCam** was used as a tool to support broader observatory commissioning, including early testing of the **Active Optics System (AOS)** and the **LSST Science Pipelines**. As a result, many artifacts present in the data are specific to **LSSTComCam** and will be addressed only if they persist with **LSSTCam**. Accordingly, the image quality achieved during this campaign, and in the **DP1** data, may not reflect the performance ultimately expected from **LSSTCam**.

Approximately 16,000 exposures⁸⁴ were collected during this campaign, the majority in support of **AOS** commissioning, system-level verification, and end-to-end testing of the telescope’s hardware and software. This included over 10000 exposures for **AOS** commissioning, more than 2000 bias and dark calibration frames, and over 2000 exposures dedicated to commissioning the **LSST Science Pipelines**. For **DP1**, we have selected a subset of 1792 science-grade exposures from this campaign that are most useful for the community to begin preparing for early science.

At the time of the campaign, the observatory was still under construction, with several key components, such as dome thermal control, full mirror control, and the final **AOS** configuration either incomplete or still undergoing commissioning. As a result, image quality varied widely throughout the campaign and exhibited a broader distribution than is expected with **LSSTCam**. Despite these limitations, the campaign successfully demonstrated system integration and established a functional observatory.

2.1. Simonyi Survey Telescope

The Simonyi Survey Telescope (B. Stalder et al. 2024) features a unique three-mirror design, including an 8.4-meter **Primary Mirror Tertiary Mirror (M1M3)** fabricated from a single substrate and a 3.5-meter **Secondary Mirror (M2)**. This compact configuration supports a wide 3.5-degree field of view while enabling exceptional stability, allowing the telescope to slew and settle in under five seconds. To achieve the scientific goals of the 10-year **LSST**, the Observatory must maintain high image quality across its wide field of view (Ž. Ivezić et al.

⁸⁴ We define an exposure as the process of exposing all **LSSTComCam** detectors. It is synonymous with visit in **DP1**. By contrast, an image is the output of a single **LSSTComCam** detector following an exposure.

2019b). This is accomplished through the **AOS** (B. Xin et al. 2015; G. Megias Homar et al. 2024), which corrects, between successive exposures, wavefront distortions caused by optical misalignments and mirror surface deformations, primarily due to the effect of gravitational and thermal loads.

The **AOS**, which comprises an open-loop component and a closed-loop component, optimizes image quality by aligning the camera and **M2** relative to **M1M3**, as well as adjusting the shapes of all three mirrors to nanometer precision. The **AOS** open-loop component corrects for predictable distortions and misalignments, while the closed-loop component addresses unpredictable or slowly varying aberrations using feedback from the corner wavefront sensors. The closed-loop wavefront sensing technique is curvature wavefront sensing, which infers wavefront errors in the optical system by analyzing extra- and intra-focal star images (S. Thomas et al. 2023). Since **LSSTComCam** lacks dedicated wavefront sensors, wavefront errors were instead estimated by defocusing the telescope ± 1.5 mm on either side of focus and applying the curvature wavefront sensing pipeline to the resulting images. Each night began with an initial alignment correction using a laser tracker to position the system within the capture range of the closed-loop algorithm (G. Megias Homar et al. 2024). Once this coarse alignment was complete, the **AOS** refined the optical alignment and applied mirror surfaces corrections to optimize the image quality across the **LSSTComCam** field of view.

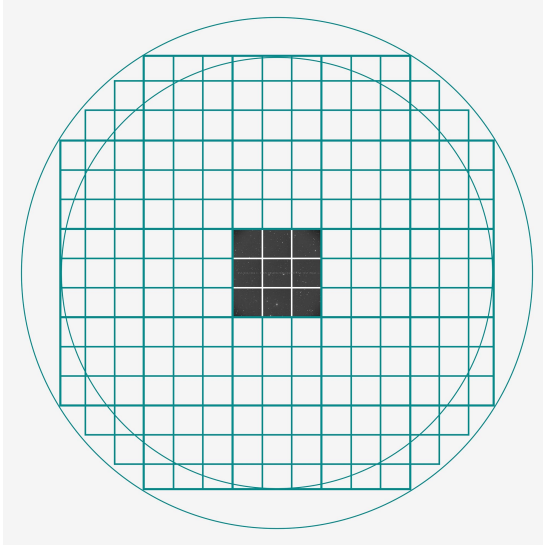
During **LSST Science Pipelines** commissioning (§2.4), observations were conducted using the **AOS** in open-loop mode only, without closed-loop corrections between exposures. Closed-loop operation, which requires additional intra- and extra-focal images with **LSSTComCam**, was not compatible with the continuous data acquisition needed by the pipelines. The image quality for these data was monitored by measuring the **Point Spread Function (PSF) Full Width at Half-Maximum (FWHM)**, and closed-loop sequences were periodically run when image quality degradation was observed.

2.2. The LSST Commissioning Camera

LSSTComCam (B. Stalder et al. 2022, 2020; J. Howard et al. 2018; SLAC National Accelerator Laboratory & NSF-DOE Vera C. Rubin Observatory 2024) is a 144-megapixel version of the 3.2-gigapixel **LSSTCam**. It covers approximately 5% of the **LSSTCam** focal plane area, with a field of view of $\sim 0.5 \text{ deg}^2$ ($40' \times 40'$), compared to **LSSTCam**’s 9.6 deg^2 . It was developed to validate camera interfaces with other observatory components and evaluate overall system performance prior to

427 the start of **LSSTCam** commissioning. Although **LSSTComCam** has a smaller imaging area, it shares the same
 428 plate scale of $0''.2$ per pixel and is housed in a support
 429 structure that replicates the mass, center of gravity,
 430 and physical dimensions of **LSSTCam**. All mechanical
 431 and utility interfaces to the telescope are implemented
 432 identically, enabling full end-to-end testing of observatory
 433 systems, including readout electronics, image ac-
 434 quisition, and data pipelines. While the **LSSTComCam**
 435 cryostat employs a different cooling system (Cryotels) to
 436 that of **LSSTCam**, it included a refrigeration pathfinder
 437 to validate the cryogenic system intended for **LSSTCam**.
 438

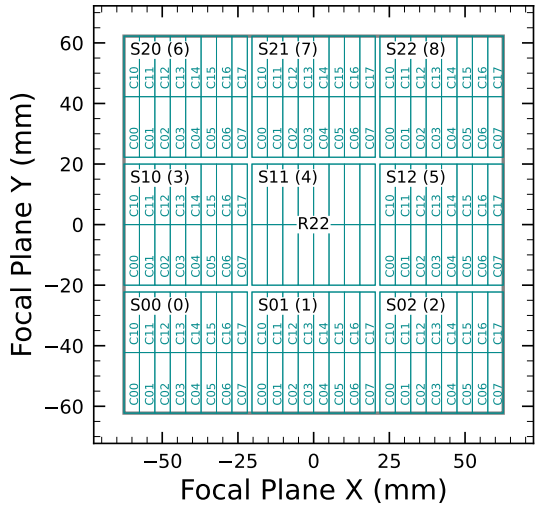
439 The **LSSTCam** focal plane comprises 25 modular rafts
 440 arranged in a 5×5 grid, of which 21 are science rafts dedi-
 441 cated to imaging and 4 are corner rafts used for guid-
 442 ing and wavefront sensing. **LSSTCam** employs CCD
 443 sensors from two vendors: Imaging Technology Labora-
 444 tory, University of Arizona (UA) (ITL) and Teledyne
 445 (E2V). In contrast, **LSSTComCam** contains only a sin-
 446 gle science raft equipped exclusively with ITL sensors.
 447 Figure 1 presents a schematic of the **LSSTCam** focal
 448 plane, with the **LSSTComCam** raft positioned at the
 449 center, corresponding to the **LSSTCam** central science
 450 raft location. The perspective is from above, looking
 451 down through the **LSSTComCam** lenses onto the focal
 452 plane.



453
 454
 455
 456
 457 **Figure 1.** Schematic showing the single LSSTComCam sci-
 ence raft positioned at the center of the full LSSTCam focal
 plane. The perspective is from above, looking down through
 the LSSTComCam lenses onto the focal plane. Credit: Ru-
 binObs/NOIRLab/SLAC/NSF/DOE/AURA.

458 with integrated readout electronics and cooling systems.
 459 Each sensor is subdivided into 16 segments arranged in
 460 a 2×8 layout, with each segment consisting of 512×2048
 461 pixels and read out in parallel using individual ampli-
 462 fiers. This design is identical across all science rafts, and
 463 to maintain uniform performance and calibration, each
 464 raft is populated exclusively with sensors from a single
 465 vendor.

466 **LSSTComCam** consists of a single science raft, design-
 467 ated Raft 22 (R22), equipped solely with ITL sensors.
 468 These sensors were selected from the best-performing re-
 469 maining ITL devices after the **LSSTCam** rafts were fully
 470 populated. Some exhibit known issues such as high read-
 471 out noise (e.g., Detector 8) and elevated Charge Transfer
 472 Inefficiency (CTI) (e.g., Detector 5). Consequently, cer-
 473 tain image artifacts present in the DP1 dataset may be
 474 specific to **LSSTComCam**. Figure 2 shows the **LSST-**
 475 **ComCam** R22 focal plane layout and the placement and
 476 numbering scheme of sensors (S) and amplifiers (C). This
 477 configuration is identical across all science rafts in
 478 **LSSTCam**. The **LSSTCam** and **LSSTComCam** focal
 479 planes are described in detail in A. A. Plazas Malagón
 480 et al. (2025).



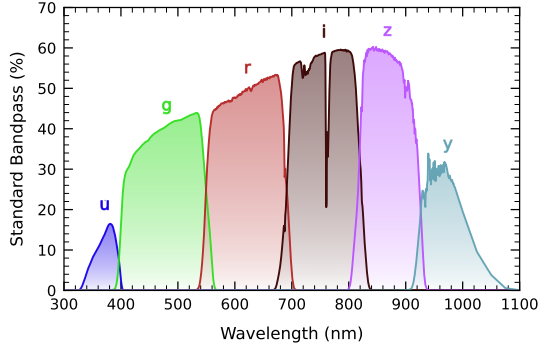
481
 482
 483
 484
 485
 486 **Figure 2.** **LSSTComCam** focal plane layout, showing Raft
 22 (R22) and the placement and numbering scheme of sen-
 sors (S) and amplifiers (C). The view is from above, looking
 through the **LSSTComCam** lenses onto the focal plane. Each
 sensor contains 16 amplifiers, and each raft is composed of a
 3×3 array of sensors. The detector number for each sensor
 is indicated in parentheses.

2.2.1. Filter Complement

487 Each science raft is a self-contained unit comprising
 488 nine $4K \times 4K$ Charge-Coupled Device (CCD) (G. E.
 489 Smith 2010) sensors arranged in a 3×3 mosaic, complete
 490 with integrated readout electronics and cooling systems.
 491 Each sensor is subdivided into 16 segments arranged in
 492 a 2×8 layout, with each segment consisting of 512×2048
 493 pixels and read out in parallel using individual ampli-
 494 fiers. This design is identical across all science rafts, and
 495 to maintain uniform performance and calibration, each
 496 raft is populated exclusively with sensors from a single
 497 vendor.

498 **LSSTComCam** supports imaging with six broadband
 499 filters *ugrizy* spanning 320–1050 nm, identical in de-
 500 sign to **LSSTCam**. However, its filter exchanger can

487 hold only three filters at a time, compared to five in
 488 LSSTCam. The full-system throughput of the six LSST-
 489 ComCam filters, which encompasses contributions from
 490 a standard atmosphere at airmass 1.2, telescope optics,
 491 camera surfaces, and the mean ITL detector quantum
 492 efficiency is shown in Figure 3.



493
 494
 495 **Figure 3.** LSSTComCam standard bandpasses, illustrating
 496 full system throughput. The bandpasses include a standard
 497 atmosphere at airmass 1.2, telescope optics, camera surfaces,
 498 and mean ITL detector quantum efficiency.

2.2.2. Timing Calibration

499 The absolute time accuracy of data taken with LSST-
 500 ComCam relies on the Network Time Protocol (NTP)
 501 for clock synchronization, which should be accurate
 502 to approximately 1 millisecond. In order to evaluate
 503 the absolute timing accuracy of the entire system we
 504 observed the geosynchronous satellite EUTELSAT 117
 505 West B with a set of 10 usable 10-second exposures over
 506 two nights. EUTELSAT 117 West B is part the GPS
 507 system and serves as one of WAAS (Wide Area Augmen-
 508 tation System) satellites operated for the U.S. Federal
 509 Aviation Administration (FAA) and used to broadcast
 510 GPS corrections to air traffic.

511 As these satellites are part of the GPS system, their
 512 positions are tracked very precisely and the record of
 513 their locations is published after the fact and can be
 514 downloaded. Following the technique previously em-
 515 ployed by other surveys, (J. L. Tonry et al. 2018), we
 516 observed the satellite while tracking the sky and then
 517 downloaded the data-files with its precise locations from
 518 the National Satellite Test Bed web site⁸⁵. By compar-
 519 ing the measured and predicted locations of the start of
 520 the satellite track on the sky, we determined that (rela-
 521 tive to the start of integration-time recorded in the FITS
 522 headers) our time was accurate to 53.6 ± 11.0 millisec-
 523 onds.

85 <https://www.nstb.tc.faa.gov/nstarchive.html>

524 This work continues to be an area of ongoing study,
 525 with the exact timing of when the shutter open com-
 526 mand is issued, and the complete profile of the shutter
 527 movement not yet determined. However the open com-
 528 mand is on average near 29 milliseconds later. Incorpor-
 529 ating the delays into the fit reduces the offset to 24.8 ± 11.0 milliseconds.

530 The full shutter takes approximately 396 milliseconds
 531 to completely open. As the LSSTComCam sensors are
 532 centered in the aperture, the center of the focal plane
 533 should be exposed about half-way through the shutter
 534 open procedure, 198 milliseconds after the open com-
 535 mand. There are uncertainties on the full motion pro-
 536 file, and the blade direction motions are currently not
 537 known, but the fraction of the shutter aperture sub-
 538 tended by the focal plane is 52%. This implies that the
 539 shutter will pass any pixel between 198 ± 103 mil-
 540 liseconds. Subtracting this from the fitted delay of 24.8
 541 milliseconds and adding the fitted error of 11.0 millisec-
 542 onds in quadrature, results in a current conservative esti-
 543 mate of the delay of -173.2 ± 104.1 milliseconds, consist-
 544 ent with and smaller than the constraints on the tim-
 545 ing offset determined using astrometric residuals from
 546 known asteroid associations presented in §5.10.2.

2.3. Flat Field System

547 During the on-sky campaign, key components of the
 548 Rubin calibration system (P. Ingraham et al. 2022),
 549 including the flat field screen, had not yet been in-
 550 stalled. As a result, flat fielding for DP1 relied en-
 551 tirely on twilight flats. While twilight flats pose chal-
 552 lenges such as non-uniform illumination and star print-
 553 through, they were the only available option during
 554 LSSTComCam commissioning and for DP1 processing.
 555 To mitigate these limitations, dithered, tracked expo-
 556 surees were taken over a broad range of azimuth and rota-
 557 tor angles to construct combined flat calibration frames.
 558 Exposure times were dynamically adjusted to reach tar-
 559 get signal levels of between 10,000 and 20,000 electrons.
 560 Future campaigns will benefit from more stable and uni-
 561 form flat fielding using the Rubin flat field system, de-
 562 scribed in P. Fagrelius & E. S. Rykoff (2025).

2.4. LSST Science Pipelines Commissioning

563 Commissioning of the LSST Science Pipelines, (Rubin
 564 Observatory Science Pipelines Developers 2025), began
 565 once the telescope was able to routinely deliver sub-
 566 arcsecond image quality. The goals included testing the
 567 internal astrometric and photometric calibration across
 568 a range of observing conditions, validating the difference
 569 image analysis and Prompt Processing (K.-T. Lim 2023)
 570 framework, and accumulating over 200 visits per band to

evaluate deep coadded images with integrated exposure times roughly equivalent to those of the planned LSST WFD 10-year depth. To support these goals, seven target fields were selected that span a range of stellar densities, overlap with external reference datasets, and collectively span the full breadth of the four primary LSST science themes. These seven fields form the basis of the DP1 dataset. Figure 4 shows the locations of these seven fields on the sky, overlaid on the LSST baseline survey footprint (R. L. Jones et al. 2021; P. Yoachim 2022; Rubin’s Survey Cadence Optimization Committee et al. 2022, 2023, 2025), along with sky coverage of both the LSSTCam and LSSTComCam focal planes. Each of the seven target fields was observed repeatedly in multiple bands over many nights. A typical observing epoch on a given target field consisted of 5-20 visits in each of the three loaded filters. Only images taken as 1x30 second exposures have been included in DP1. All images were acquired using the Rubin Feature-Based Scheduler (FBS), version 3.0 (E. Naghib et al. 2019; P. Yoachim et al. 2024). Table 1 lists the seven DP1 fields and their pointing centers, and provides a summary of the band coverage in each.

The temporal sampling distribution of observations per band and per night is shown in Figure 5. Gaps in coverage across some bands arise from the fact that LSSTComCam can only accommodate three filters at a time (see §2.2). As the campaign progressed, the temporal sampling became denser across all fields, reflecting improved efficiency and increased time allocated for science observations. The Extended Chandra Deep Field-South Survey (ECDFS) field received the most consistent and densest temporal sampling. It is important to note that the time sampling in the DP1 dataset differs significantly from what will be seen in the final LSST data. All fields except for the low ecliptic latitude field, Rubin_SV_38_7, used a small random dithering pattern. The random translational dithers of the telescope boresight were applied for each visit, with offsets of up to 0.2 degrees around the pointing center (Table 1). The rotational dithers of the camera rotator were typically approximately 1 degree per visit, with larger random offsets at each filter change, which worked to keep operational efficiency high. The Rubin_SV_38_7 field used a different dither pattern to optimize coverage of Solar System Objects and test Solar System Object linking across multiple nights. These observations used a 2x2 grid of LSSTComCam pointings to cover an area of about 1.3 degree x 1.3 degrees. The visits cycled between the grid’s four pointing centers, using small random translational dithers to fill chip gaps with the goal

of acquiring 3-4 visits per pointing center per band in each observing epoch.

Figure 6 shows sky coverage maps showing the distribution of visits in each of the seven DP1 fields, color coded by band. The images clearly show the focal plane chip gaps and dithering pattern. Only the detectors for which single frame processing succeeded are included in the plots, which explains why the central region of 47-Tuc looks thinner than the other fields. Table 2 reports the 5σ point source depths for coadded images per field and per band, where coverage in a band is non-zero, together with the expected 10-year LSST depths derived from the baseline simulated survey (F. B. Bianco et al. 2022).

2.5. Delivered Image Quality

The delivered image quality is influenced by contributions from both the observing system (i.e., dome, telescope and camera) and the atmosphere. During the campaign, the Rubin Differential Image Motion Monitor (DIMM) was not operational, so atmospheric seeing was estimated using live data from the Southern Astrophysical Research Telescope (SOAR) Ring-Image Next Generation Scintillation Sensor (RINGSS) seeing monitor, also located on Cerro Pachón. Although accelerometers mounted on the mirror cell and top-end assembly were available to track dynamic optics effects, such as mirror oscillations that can degrade optical alignment, this data was not used during the campaign. Mount encoder data were used to measure the mount jitter in every image, with a measured median contribution of 0.004 arcseconds to image degradation. As the pointing model was not fine tuned, tracking errors could range from 0.2 to 0.4 arcseconds per image, depending on RA and Dec. Dome and mirror-induced seeing were not measured during the campaign.

The DP1 median delivered image quality, quantified as the PSF at FWHM across all filters and target fields, is $1''14$. The best images achieve a PSF FWHM of approximately $0''58$. Both the per-sensor PSF FWHM and the overall median vary depending on the filter and the specific target field. The median delivered image quality per band and target field is provided in Table 3.

Figure 7 shows the distribution of PSF FWHM (arcsec) over all 16071 individual sensors images. Ongoing efforts aim to quantify all sources of image degradation, including contributions from the camera system; static and dynamic optical components; telescope mount motion; observatory-induced seeing from the dome and primary mirror; and atmospheric conditions. For the LSST, the design specification for the median delivered image quality, referenced to the zenith and 550 nm, is

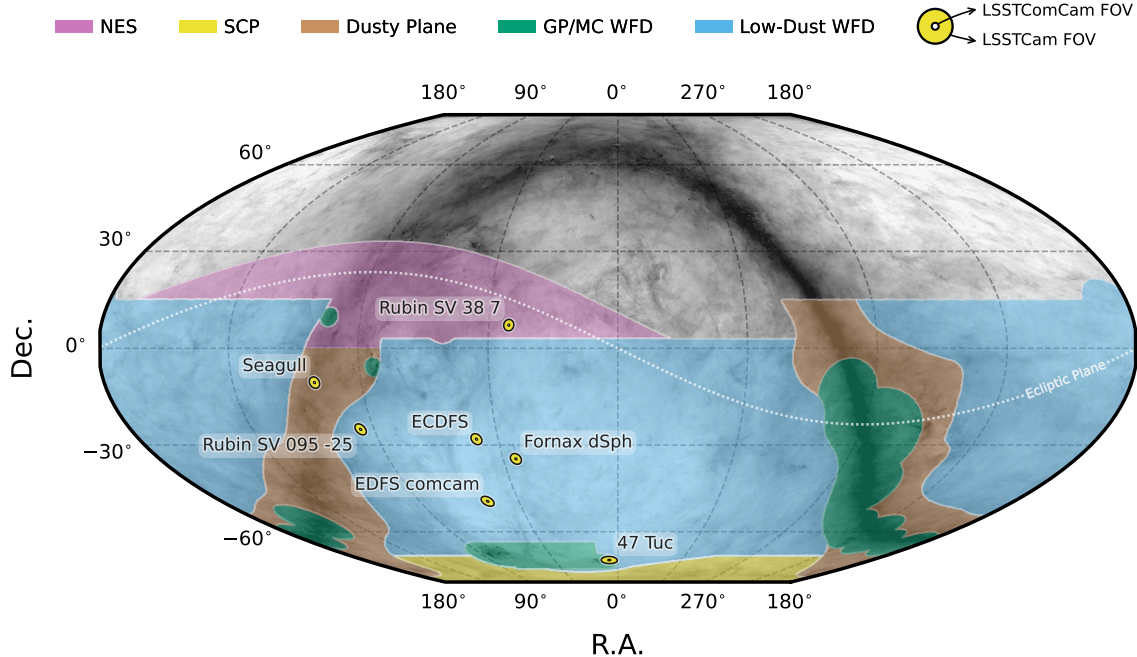


Figure 4. Locations of the seven DP1 fields overlaid on the LSST baseline survey footprint. NES: North Ecliptic Spur, SCP: South Celestial Pole, Low-Dust WFD: regions away from the Galactic Plane (GP) observed with a WFD cadence, GP/MC WFD: Galactic Plane and Magellanic Clouds regions observed with a WFD cadence. The FOV covered by the LSSTCam and LSSTComCam focal planes is shown as concentric yellow circles about the pointing center of each field.

Table 1. DP1 fields and pointing centers with the number of exposures in each band per field. ICRS coordinates are in units of decimal degrees, and are specified as J2000.

Field Code	Field Name	RA	DEC	Band						Total	
				deg	deg	<i>u</i>	<i>g</i>	<i>r</i>	<i>i</i>	<i>z</i>	
47_Tuc	47 Tucanae Globular Cluster	6.128	-72.090	6	10	32	19	0	5		72
ECDFS	Extended Chandra Deep Field South	53.160	-28.100	43	230	237	162	153	30		855
EDFS_comcam	Rubin SV Euclid Deep Field South	59.150	-48.730	20	61	87	42	42	20		272
Fornax_dSph	Fornax Dwarf Spheroidal Galaxy	40.080	-34.450	0	5	25	12	0	0		42
Rubin_SV_095_-25	Rubin SV Low Galactic Latitude Field	95.040	-25.000	33	82	84	23	60	10		292
Rubin_SV_38_7	Rubin SV Low Ecliptic Latitude Field	37.980	7.015	0	44	40	55	20	0		159
Seagull	Seagull Nebula	106.300	-10.510	10	37	43	0	10	0		100
Total				112	469	548	313	285	65		1792

0''.7. This value corresponds to the measured median atmospheric seeing at the Cerro Pachón site and a system contribution to delivered image quality of 0''.35 added in quadrature.

The DP1 median delivered image quality across all bands is 1''.14, as measured by the [PSF FWHM](#). The best images achieved a [PSF FWHM](#) of approximately 0''.58.

3. OVERVIEW OF THE CONTENTS OF RUBIN DP1

Here we describe Rubin DP1 data products and provide summary statistics for each, but we also refer the reader to the DOI-registered DP1 release documentation available at <https://dp1.lsst.io> and the catalog schemas

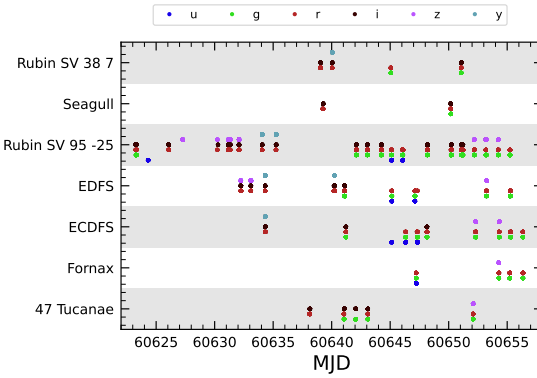


Figure 5. Distribution of DP1 observations by date grouped by field as a function of MJD. Each dot represents a single 30-second exposure, color-coded by filter.

Table 2. DP1 median 5σ coadded point-source detection limits per field and band, compared with the expected 10-year LSST values derived from the baseline simulated survey (F. B. Bianco et al. 2022).

Field Code	Band					
	<i>u</i>	<i>g</i>	<i>r</i>	<i>i</i>	<i>z</i>	<i>y</i>
47_Tuc	-	24.03	24.24	23.90	-	21.79
ECDFS	24.55	26.18	25.96	25.71	25.07	23.10
EDFS_comcam	23.42	25.77	25.72	25.17	24.47	23.14
Fornax_dSph	-	24.53	25.07	24.64	-	-
Rubin_SV_095_-25	24.29	25.46	24.95	24.86	24.32	22.68
Rubin_SV_38_7	-	25.46	25.15	24.86	23.52	-
Seagull	23.51	24.72	24.19	-	23.30	-
LSST 10-year	25.73	26.86	26.88	26.34	25.63	24.87

Table 3. DP1 Median image quality per field and per band quantified as the PSF at FWHM in arcseconds.

Field Code	Band						All
	<i>u</i>	<i>g</i>	<i>r</i>	<i>i</i>	<i>z</i>	<i>y</i>	
47_Tuc	-	1.27	1.25	1.11	-	1.33	1.22
ECDFS	1.40	1.14	1.08	1.00	1.00	1.07	1.08
EDFS_comcam	1.88	1.25	1.20	1.10	1.18	0.99	1.19
Fornax_dSph	-	1.16	0.82	0.93	-	-	0.85
Rubin_SV_095_-25	1.40	1.25	1.14	0.97	1.17	0.82	1.19
Rubin_SV_38_7	-	1.13	1.13	1.10	1.22	-	1.13
Seagull	1.50	1.34	1.19	-	1.19	-	1.25
All	1.48	1.17	1.12	1.03	1.11	1.01	1.13

The data products that comprise DP1 provide an early preview of future LSST data releases and are strongly dependent on the type and quality of the data that was collected during the LSSTComCam on-sky campaign (§2.4). Consequently not all anticipated LSST data products, as described in the Data Product Definition Document (DPDD) (M. Jurić et al. 2023), were produced for the DP1 dataset.

Rubin Observatory has adopted the convention by which single-epoch detections are referred to as Sources. By contrast, the astrophysical object associated with a given detection is referred to as an Object⁸⁷. As such, a given Object will likely have multiple associated Sources, since it will be observed in multiple epochs.

At the highest level, the DP1 data products fall into one of five types:

- **Images**, including single-epoch images, deep and template coadded images, and difference images (§3.1);
- **Catalogs** of astrophysical Sources and Objects detected and measured in the aforementioned images. We also provide the astrometric and photometric reference catalog generated from external sources that was used during processing to generate the DP1 data products (§3.2);
- **Maps**, which provide non-science-level visualizations of the data within the release. They include, for example, zoomable multi-band images and coverage maps (§3.3);

⁸⁶ Searchable catalog schemas are also available to Data Rights Holders via the Rubin Science Platform at <https://data.lsst.cloud>.

⁸⁷ We caution that this nomenclature is not universal; for example, some surveys call “detections” what we call “sources”, and use the term “sources” for what we call “objects”.

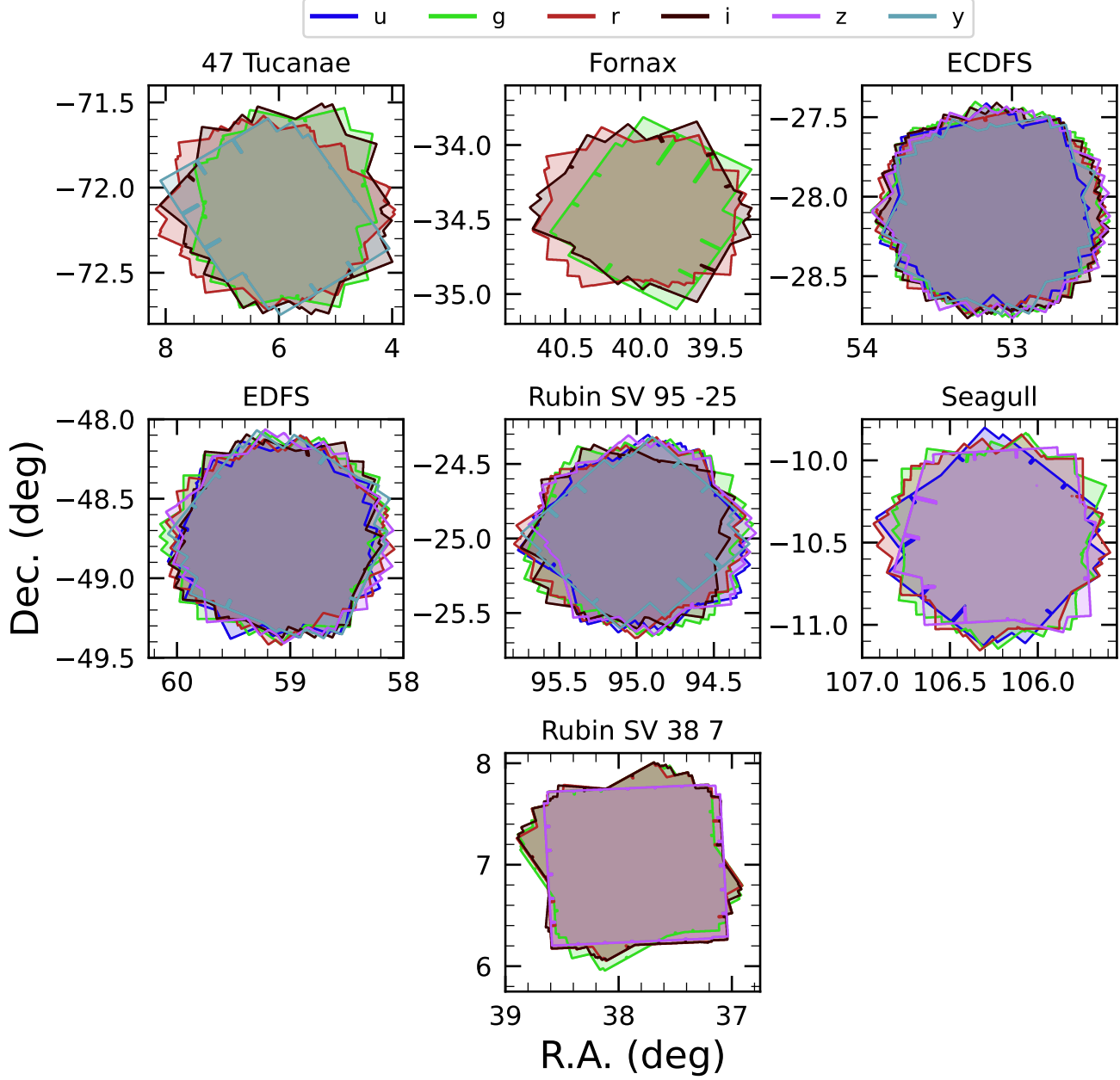
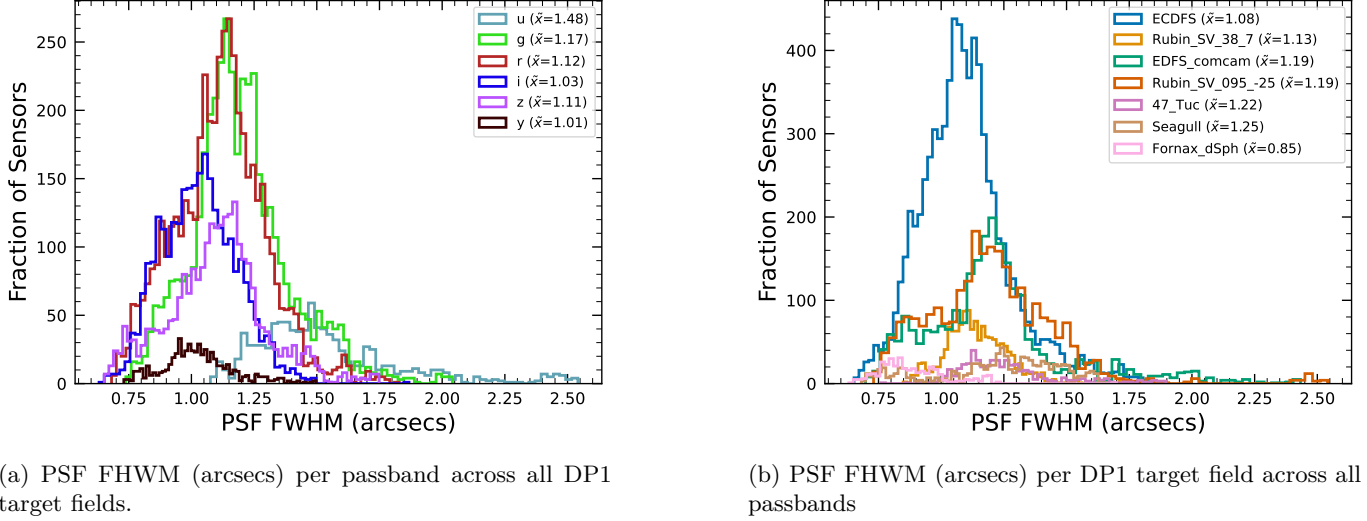


Figure 6. Sky coverage maps showing the distribution of visits in each field, color coded by band. The images clearly show the focal plane chip gaps and dithering pattern. Only the detectors for which single frame processing succeeded are included in the plots, which explains why the central region of 47_Tuc looks thinner than the other fields.

732 • **Ancillary data products**, including, for exam-
 733 ple, the parameters used to configure the data pro-
 734 cessing pipelines, log and processing performance
 735 files, and [calibration](#) data products ([§3.6](#));

740 While images and catalogs are expected to be the pri-
 741 mary data products for scientific research, we also rec-
 742 ognize the value of providing access to other data types
 743 to support investigations and ensure transparency.

736 • **Metadata** in the form of tables containing infor-
 737 mation about each visit and processed image, such
 738 as pointing, exposure time, and a range of image
 739 quality summary statistics ([§3.5](#)).



(a) PSF FWHM (arcsecs) per passband across all DP1 target fields.

(b) PSF FWHM (arcsecs) per DP1 target field across all passbands

Figure 7. Histograms showing the distribution of delivered image quality for all 16071 single-epoch individual sensors in the DP1 dataset per passband (a) and per field (b). The median values are given in the legend.

To facilitate processing, Rubin DP1 uses a single skymap⁸⁸ that covers the entire sky area encompassing the seven DP1 fields. The DP1 skymap divides the entire celestial sphere into 18938 tracts, each covering approximately 2.8 deg^2 . The tracts are arranged in rings of declination, ordered from south to north, then with increasing right ascension within a ring. Each tract is further subdivided into 10×10 equally-sized patches. Both tracts and patches overlap with their neighboring regions. The amount of overlap between tracts changes with declination, with tracts nearest the poles having the greatest degree of overlap; the minimum overlap between tracts is 1.0 . By contrast, the amount of overlap between patches is constant, with each patch overlapping each of its neighbouring patches by $80''.0$. Each patch covers 0.036 deg^2 which, due to the patch overlap, is slightly larger than the tract area divided by the number of patches in a tract. The aerial coverage of a patch is comparable to, but somewhat smaller than, the 0.058 deg^2 field-of-view of a single LSSTComCam or LSSTCam detector, meaning each detector image spans multiple patches. The size of a tract is larger than the LSSTComCam field of view. However, since each observed field extends across more than one tract, each field covers multiple tracts.

The skymap is integral to the production of co-added images. To create a coadded image, the processing pipeline selects all calibrated science images in a given

field that meet specific quality thresholds (§3.1 and §4.5.1) for a given patch, warps them onto a single consistent pixel grid for that patch, as defined by the skymap, then coadds them. Each individual coadd image therefore covers a single patch.

Throughout this section, the data product names are indicated using monospace font. Data products are accessed via either the IVOA Services (§6.2.1) or the Data Butler (§6.2.2).

3.1. Science Images

Science images are exposures of the night sky, as distinct from calibration images (§3.6.3). Although the release includes calibration images, thereby allowing users to reprocess the raw images if needed, this is expected to be necessary only in rare cases. Users are strongly encouraged to start from the visit_image provided. The data product names shown here are those used by the Data Butler, but the names used in the IVOA Services differ only slightly in that they are prepended by “lsst.”.

- raw images (NSF-DOE Vera C. Rubin Observatory 2025b) are unprocessed data received directly from the camera. Each raw corresponds to a single CCD from a single LSSTComCam exposure of 30 s duration. Each LSSTComCam exposure typically produces up to nine raws, one per sensor in the focal plane. However, a small number of exposures resulted in fewer than nine raw images due to temporary hardware issues or readout faults.

In total, DP1 includes 16125 raw images. Table 4 provides a summary by target and band. A raw contains 4608×4096 pixels, including pres-

⁸⁸ A skymap is a tiling of the celestial sphere, organizing large-scale sky coverage into manageable sections for processing and analysis. While the skymap described here is specific to DP1, we do not anticipate major changes to the skymap in future data releases.

Table 4. Number of `raw` images per field and band. Each `raw` image corresponds to a single 30-second LSSTComCam exposure on one CCD. Most exposures produce nine raw images, one per sensor in the focal plane, however some yield fewer due to occasional hardware or readout issues.

Field Code	Band						Total
	<i>u</i>	<i>g</i>	<i>r</i>	<i>i</i>	<i>z</i>	<i>y</i>	
47_Tuc	54	90	288	171	0	45	648
ECDFS	387	2070	2133	1455	1377	270	7692
EDFS_comcam	180	549	783	378	378	180	2448
Fornax_dSph	0	45	225	108	0	0	378
Rubin_SV_095_-25	297	738	756	207	540	90	2628
Rubin_SV_38_7	0	396	360	495	180	0	1431
Seagull	90	333	387	0	90	0	900
Total	1008	4221	4932	2814	2565	585	16125

can and overscan, and occupies around 18 MB of disk space.⁸⁹ The field of view of a single `raw`, excluding prescan and overscan regions, is roughly $0.23 \times 0.22 \approx 0.051 \text{ deg}^2$, corresponding to a plate scale of $0.^{\prime\prime}2$ per pixel.

- `visit_images` (NSF-DOE Vera C. Rubin Observatory 2025c) are fully-calibrated processed images. They have undergone instrument signature removal (§4.2.1) and all the single frame processing steps described in §4.2 which are, in summary: **PSF** modeling, **background** subtraction, and astrometric and photometric **calibration**. As with `raws`, a `visit_image` contains processed data from a single **CCD** resulting from a single 30 s **LSST-ComCam** exposure. As a consequence, a single **LSSTComCam** exposure typically results in nine `visit_images`. The handful of exposures with fewer than nine `raw` images also have fewer than nine `visit_images`, but there are an additional 153 `raw` that failed processing and for which there is thus no corresponding `visit_image`. The majority of failures – 131 in total – were due to challenges with astrometric fits or **PSF** models in the 47_Tuc crowded field. The other failures were in the Rubin_SV_095_-25 (9 failures), ECDFS (8), Fornax_dSph (3), and EDFS_comcam (2) fields.

⁸⁹ Each amplifier image contains 3 and 64 columns of serial prescan and overscan pixels, respectively, and 48 rows of parallel overscan pixels, meaning a `raw` contains 4072×4000 exposed pixels.

In total, there are 15972 `visit_images` in **DP1**. Each `visit_image` comprises three images: a calibrated science image, a variance image, and a pixel-level bitmask that flags issues such as saturation, cosmic rays, or other artifacts. Each `visit_image` also contains a position-dependent **PSF** model, **World Coordinate System (WCS)** information, and various **metadata** providing information about the observation and processing. The science and variance images and the pixel mask each contain 4072×4000 pixels. In total, a single `visit_image`, including all extensions and **metadata**, occupies around 110 MB of disk space. A plot showing the normalized cumulative histogram of the 5σ depths of all the `visit_images` in **DP1** is shown in Figure 8.

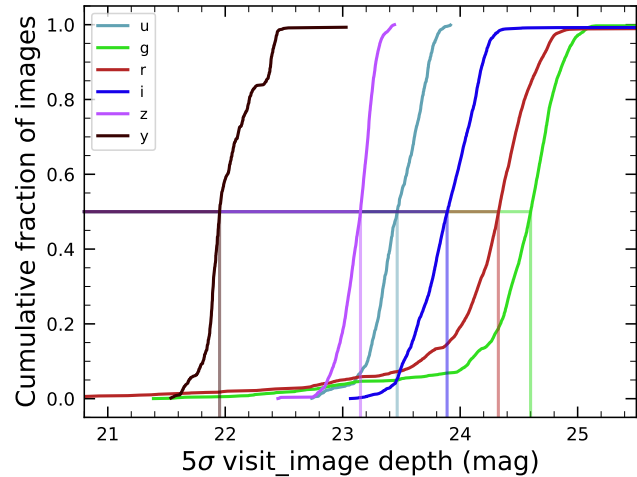


Figure 8. Normalized cumulative histograms of the 5σ depths of all `visit_images` in each band. The vertical lines indicate the 50th percentiles for each band (see legend).

- `deep_coadds` (NSF-DOE Vera C. Rubin Observatory 2025d) are the product of warping and co-adding multiple `visit_images` covering a given `patch`, as defined by the skymap. `deep_coadds` are created on a per-band basis, meaning only data from exposures taken with a common filter are coadded. As such, there are up to six `deep_coadds` covering each `patch` – one for each of the six **LSSTComCam** bands. The process of producing `deep_coadds` is described in §4.5 but, to summarize, it involves the selection of suitable `visit_images` (both in terms of `patch` coverage, band, and image quality), the warping of those `visit_images` onto a common pixel grid, and the co-adding of the warped `visit_images`. To be included in a **DP1** `deep_coadd`, a `visit_image` needed to have

863 a **PSF FWHM** smaller than $1.^{\circ}7$. Of the 15972
 864 **visit_images**, 15375 satisfied this criterion and
 865 were therefore used to create **deep_coadds**.

866 There are a total of 2644 **deep_coadds** in **DP1**.
 867 As mentioned above, a single **deep_coadd** covers
 868 one **patch**, and includes a small amount of over-
 869 lap with its neighboring **patch**. The skymap used
 870 for **DP1** defines a **patch** as having an on-sky area
 871 of 0.028 deg^2 excluding overlap, and 0.036 deg^2
 872 including overlap. A single **deep_coadd** – includ-
 873 ing overlap – contains 3400×3400 equal-sized
 874 pixels, corresponding to a platescale of $0.^{\circ}2$ per
 875 pixel. Each **deep_coadd** contains the science im-
 876 age (i.e., the coadd), a variance image, and a pixel
 877 mask; all three contain the same number of pix-
 878 els. Each **deep_coadd** also contains a position-
 879 dependent **PSF** model (which is the weighted sum
 880 of the **PSF** models of the input **visit_images**),
 881 **WCS** information, plus various **metadata**.

882 The number of **visit_images** that contributed to
 883 a given **deep_coadd** varies across the patch; the
 884 Survey Property Maps can be consulted to gain in-
 885 sights into the total exposure time at all locations
 886 covered by the survey. Similarly, since coadds al-
 887 ways cover an entire **patch**, it is common for a
 888 **deep_coadd** to contain regions that were not cov-
 889 ered by any of the selected **visit_images**, partic-
 890 ularly if the **patch** is on the outskirts of a field
 891 and was thus not fully observed. By the nature of
 892 how coadds are produced, such regions may con-
 893 tain seemingly valid **flux** values (i.e., not necessar-
 894 ily zeros or NaNs), but will instead be flagged with
 895 the **NO_DATA** flag in the pixel mask. It is therefore
 896 crucial that the pixel mask be referred to when
 897 analyzing **deep_coadds**.

- 898 • **template_coadds** ([NSF-DOE Vera C. Rubin Observatory 2025e](#)) are those created to use as tem-
 899 plates for difference imaging, i.e., the process of
 900 subtracting a template image from a **visit_im-
 901 age** to identify either variable or **transient**
 902 objects. It should be noted, however, that **tem-
 903 plete_coadds** are not themselves subtracted from
 904 **visit_images** but are, instead, warped to match
 905 the **WCS** of a **visit_image**. It is this warped
 906 template that is subtracted from the **visit_image**
 907 to create a difference image.⁹⁰ As with **deep_**
 908 **coadds**, **template_coadds** are produced by warp-

910 ing and co-adding multiple **visit_images** cover-
 911 ing a given skymap-defined **patch**. The process
 912 of building **template_coadds** is the same as that
 913 for **deep_coadds**, but the selection criteria dif-
 914 fer between the two types of coadd. In the case
 915 of **template_coadds**, one third of **visit_images**
 916 covering the **patch** in question with the narrow-
 917 est **PSF FWHM** are selected. If one third cor-
 918 responds to fewer than twelve **visit_images** (i.e.,
 919 there are fewer than 36 **visit_images** covering the
 920 **patch**), then the twelve **visit_images** with the
 921 narrowest **PSF FWHM** are selected. Finally, if
 922 there are fewer than twelve **visit_images** cover-
 923 ing the **patch**, then all **visit_images** are selected.
 924 Of the 15972 **visit_images**, 13113 were used to
 925 create **template_coadds**. This selection strategy
 926 is designed to optimize for **seeing** when a **patch**
 927 is well-covered by **visit_images**, yet still enable
 928 the production of **template_coadds** for poorly-
 929 covered patches. As with **deep_coadds**, the num-
 930 ber of **visit_images** that contributed to a **tem-
 931 plate_coadd** varies across the patch.

932 DP1 contains a total of 2730 **template_coadds**.⁹¹
 933 As with **deep_coadds**, a single **template_coadd**
 934 covers a single **patch**. Since the same skymap is
 935 used when creating both **deep_coadd** and **tem-
 936 plate_coadds**, the on-sky area and pixel count of
 937 **template_coadds** are the same as that of a **deep_**
 938 **coadd** (see above). Similarly, **template_coadds**
 939 contain the science image (i.e., the coadd), a vari-
 940 ance image, and a pixel mask; all three contain the
 941 same number of pixels. Also included are the **PSF**
 942 model, **WCS** information, and **metadata**. As is
 943 the case for **deep_coadd**, those pixels within **tem-
 944 plate_coadds** that are not covered by any of the
 945 selected **visit_images** may still have seemingly
 946 valid values, but are indicated with the **NO_DATA**
 947 flag within the pixel mask.

- 948 • **difference_images** ([NSF-DOE Vera C. Rubin Observatory 2025f](#)) are generated by the subtrac-
 949 tion of the warped, scaled, and **PSF**-matched **tem-
 950 plate_coadd** from the **visit_image** (see §4.6.1).
 951 In principle, only those sources whose **flux** has
 952 changed relative to the **template_coadd** should be
 953 apparent (at a significant level) within a **differ-
 954 ence_image**. In practice, however, there are nu-
 955 merous spurious sources present in **difference_**
 956

⁹⁰ For storage space reasons, warped templates are not retained for **DP1**, as they can be readily and reliably recreated from the **template_coadds**.

⁹¹ The difference in the number of **deep_coadds** and **template_coadds** is due to the difference in the **visit_image** selection criteria for each coadd.

957 images due to unavoidably imperfect template
 958 matching.

959 In total, there are 15972 `difference_images` in
 960 `DP1`, one for each `visit_image`.

961 Like `visit_images`, `difference_images` contain
 962 the science (i.e., difference) image, a variance im-
 963 age, and a pixel mask; all three contain the same
 964 number of pixels, which is the same as that of
 965 the input `visit_image`. Also included is the `PSF`
 966 model, `WCS` information, and `metadata`.

- 967 • Background images contain the model `background`
 968 that has been generated and removed from a
 969 science image. `visit_images`, `deep_coadds` and
 970 `template_coadds` all have associated `background`
 971 images.⁹² Background images contain the same
 972 number of pixels as their respective science im-
 973 age, and there is one `background` image for each
 974 `visit_image`, `deep_coadd`, and `template_coadd`.
 975 Difference imaging analysis also measures and sub-
 976 tracts a `background` model, but the `difference_`
 977 `background` data product is not written out by
 978 default and is not part of `DP1`.

979 Background images are not available via the `IVOA`
 980 Service; they can only be accessed via the `Butler`
 981 Data Service.

982 3.2. Catalogs

983 Here we describe science-ready tables produced by the
 984 science pipelines. All but one of the catalogs described
 985 here contain data for detections in the images described
 986 in §3.1, the exception being the `Calibration` catalog,
 987 which contains reference data obtained from previous
 988 surveys. Observatory-produced `metadata` tables are de-
 989 scribed in §3.5. Each type of catalog contains mea-
 990 surements for either Sources detected in `visit_images`
 991 and `difference_images`, or Objects detected in `deep_`
 992 `coadds`.

993 While the `Source`, `Object`, `ForcedSource`, `Dia-`
 994 `Source`, `DiaObject`, and `ForcedSourceOnDiaObject`
 995 catalogs described below each differ in terms of their
 996 specific columns, in general they each contain: one or
 997 more unique identification numbers, positional infor-
 998 mation, one or more types of `flux` measurements (e.g., aper-
 999 ture fluxes, `PSF` fluxes, Gaussian fluxes, etc.), and a se-
 1000 ries of boolean flags (indicating, for example, whether
 1001 the source/object is affected by saturated pixels, cosmic
 1002 rays, etc.) for each source/object. The Solar System

1003 catalogs `SSObject` and `SSSource` deviate from this gen-
 1004 eral structure in that they instead contain orbital pa-
 1005 rameters for all known asteroids. Where applicable, all
 1006 measured properties are reported with their associated
 1007 1σ uncertainties.

1008 Since `DP1` is a preview, it does not include all the
 1009 catalogs expected in a full `LSST Data Release`. Addi-
 1010 tionally, the catalogs it does include may be missing
 1011 some columns planned for future releases. Where this is
 1012 known to be the case, we note what data are missing in
 1013 the catalog descriptions that follow.

1014 Catalog data are stored in the `Qserv` database (§6.5.1)
 1015 and are accessible via `Table Access Protocol (IVOA`
 1016 `standard)` (IVOA), and an online `DP1` catalog schema
 1017 is available at <https://sdm-schemas.lsst.io/dp1.html>.
 1018 Catalog data are also accessible via the Data Butler (see
 1019 §6.2.2).

- 1020 • The `Source` catalog (NSF-DOE Vera C. Rubin
 1021 Observatory 2025g) contains data on all sources
 1022 which are, prior to deblending (§4.5.2), detected
 1023 with a greater than 5σ significance in each individ-
 1024 ual visit. The detections reported in the `Source`
 1025 catalog have undergone deblending; in the case of
 1026 blended detections, only the deblended sources are
 1027 included in the `Source` catalog. It is important
 1028 to note that while the criterion for inclusion in a
 1029 `Source` catalog is a $> 5\sigma$ detection in a `visit_im-`
 1030 `age` prior to deblending, the positions and fluxes
 1031 are reported post-deblending. Hence, it is possible
 1032 for the `Source` catalog to contain sources whose
 1033 `flux`-to-error ratios – potentially of all types (i.e.,
 1034 aperture `flux`, `PSF flux`, etc.) – are less than 5.

1035 In addition to the general information mentioned
 1036 above (i.e., IDs, positions, fluxes, flags), the
 1037 `Source` catalog also includes basic `shape` and ex-
 1038 tendedness information.

1039 The `Source` catalog contains data for 46 million
 1040 sources in `DP1`.

1041 A cumulative histogram showing the `PSF` magni-
 1042 tudes of all `sources` contained within the `Source`
 1043 catalogue is presented in the top panel of Figure 9

- 1044 • The `Object` catalog (NSF-DOE Vera C. Rubin
 1045 Observatory 2025h) contains data on all objects
 1046 detected with a greater than 5σ significance in the
 1047 `deep_coadds`. With coadd images produced on a
 1048 per-band basis, a $> 5\sigma$ detection in one or more of
 1049 the bands will result in an object being included in
 1050 the `Object` catalog. For cases where an object is
 1051 detected at $> 5\sigma$ in more than one band, a cross-
 1052 matching has been performed between bands to

⁹² In future data releases, `background` images may be included as part of their respective science image data product.

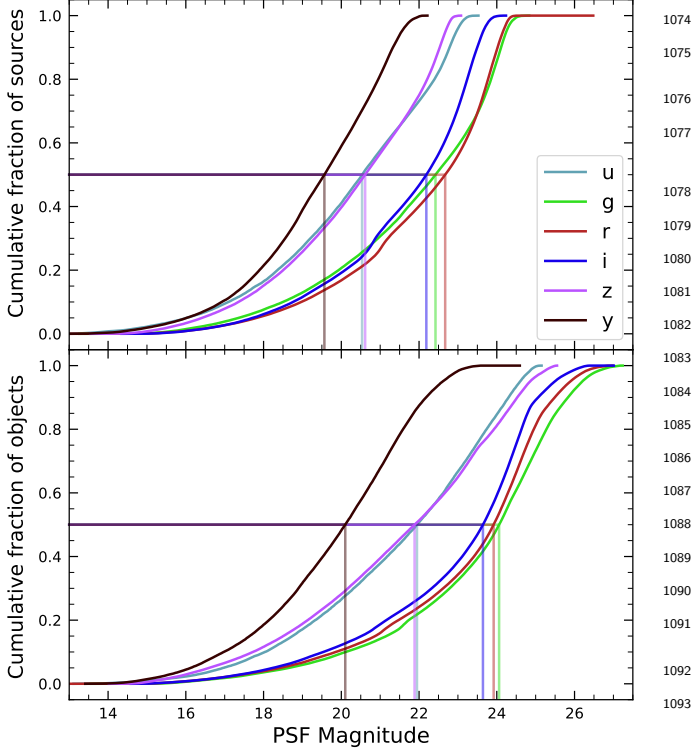


Figure 9. Normalized cumulative histograms of the PSF magnitudes of all $> 5\sigma$ -detected **sources** (top panel) and **objects** (bottom panel) contained in the **Source** and **Object** catalogs, respectively, separated according to band (see legend). The vertical lines indicate the 50th percentile for each band.

associate an object in one band with its counterpart(s) in the other bands. As such, unlike the **Source** catalog, the **Object** catalog contains data from multiple bands. The objects reported in the **Object** catalog have also undergone deblending; in the case of blended detections, only the deblended child objects are included in the catalog. As with the **Source** catalog, the criterion for inclusion in the **Object** catalog is a $> 5\sigma$ detection in one of the **deep_coadds** prior to deblending, yet the positions and fluxes of objects are reported post-deblending. Hence, it is possible for **Object** catalog to contain **objects** whose **flux**-to-error ratios — potentially of all types and in all bands — are less than 5.

In addition to the general information mentioned above (i.e., IDs, positions, fluxes, flags), the **Object** catalog also includes basic **shape** and extendedness information. While they may be included in future data releases, no photometric redshifts, Petrosian magnitudes (V. Petrosian 1976), proper

motions or periodicity information are included in the **DP1** object catalogs.

The **Object** catalog contains data for 2.3 million objects in **DP1**.

- The **ForcedSource** catalog (NSF-DOE Vera C. Rubin Observatory 2025i) contains forced PSF photometry measurements performed on both **difference_images** (i.e., the **psfDiffFlux** column) and **visit_images** (i.e., the **psfFlux** column) at the positions of all the objects in the **Object** catalog, to allow assessment of the time variability of the fluxes. We recommend using the **psfDiffFlux** column when generating light curves because this quantity is less sensitive to **flux** from neighboring sources than **psfFlux**. In addition to **forced photometry PSF** fluxes, a number of boolean flags are also included in the **Forced-Source** catalog.

The **ForcedSource** catalog contains a total of 269 million entries across 2.3 million unique objects.

- The **DiaSource** catalogs (NSF-DOE Vera C. Rubin Observatory 2025j) contains data on all the sources detected at $> 5\sigma$ significance — including those associated with known Solar System objects — in the **difference_images**. Unlike sources detected in **visit_images**, sources detected in **difference images** (hereafter, “**DiaSource**”) have gone through an association step in which an attempt has been made to associate them into underlying objects called “**DiaObject**”. The **DiaSource** catalog consolidates all this information across multiple visits and bands. The detections reported in the **DiaSource** catalog have not undergone deblending.

The **DiaSource** catalog contains data for 3.1 million **DiaSources** in **DP1**.

- The **DiaObject** catalog (NSF-DOE Vera C. Rubin Observatory 2025k) contains the astrophysical objects that **DiaSources** are associated with (i.e., the **DiaObjects**). The **DiaObject** catalog contains only non-Solar System Objects; Solar System Objects are, instead, recorded in the **SSObject** catalog. When a **DiaSource** is identified, the **DiaObject** and **SSObject** catalogs are searched for objects to associate it with. If no association is found, a new **DiaObject** is created and the **DiaSource** is associated to it. Along similar lines, an attempt has been made to associate **DiaObjects** across multiple bands, meaning the **DiaObject** catalog, like

the `Object` catalog, contains data from multiple bands. Since `DiaObjects` are typically `transient` or variable (by the nature of their means of detection), the `DiaObject` catalog contains summary statistics of their fluxes, such as the mean and standard deviation over multiple epochs; users must refer to the `ForcedSourceOnDiaObject` catalog (see below) or the `DiaSource` catalog for single `epoch flux` measurements of `DiaObjects`.

The `DIAObject` catalog contains data for 1.1 million `DiaObjects` in `DP1`.

- The `ForcedSourceOnDiaObject` catalog (NSF-DOE Vera C. Rubin Observatory 2025l) is equivalent to the `ForcedSource` catalog, but contains `forced photometry` measurements obtained at the positions of all the `DiaObjects` in the `DiaObject` catalog.

The `ForcedSourceOnDiaObject` catalog contains a total of 197 million entries across 1.1 million unique `DiaObjects`.

- The `SSObject` catalog (NSF-DOE Vera C. Rubin Observatory 2025m), Minor Planet Center Orbit database (MPCORB) and `SSObject`, carry information about solar system objects. The `MPCORB` table provides the Minor Planet Center-computed orbital elements for all known asteroids, including those that Rubin discovered. For `DP1`, the `SSObject` catalog serves primarily to provide the mapping between the International Astronomical Union (IAU) designation of an object (listed in MPCORB), and the internal `ssObject` identifier, which is used as a key to find solar system object observations in the `DiaSource` and `SSSource` tables. The `SSObject` catalog contains data for 431 `SSObjects` in `DP1`.
- The `SSSource` catalog (NSF-DOE Vera C. Rubin Observatory 2025n) contains data on all `DiaSources` that are either associated with previously-known Solar System Objects, or have been confirmed as newly-discovered Solar System Objects by confirmation of their orbital properties. As entries in the `SSSource` catalog stem from the `DiaSource` catalog, they have all been detected at $> 5\sigma$ significance in at least one band. The `SSSource` catalog contains data for 5988 Solar System Sources.

- The `CcdVisit` catalog (NSF-DOE Vera C. Rubin Observatory 2025o) contains data for each individual processed `visit_image`. In addition to technical information, such as the on-sky coordinates

of the central pixel and measured pixel scale, the `CcdVisit` catalog contains a range of data quality measurements, such as whole-image summary statistics for the `PSF` size, zeropoint, sky `background`, sky noise, and quality of astrometric solution. It provides an efficient method to access `visit_image` properties without needing to access the image data. When combined with the data contained in the `Visit` table described in §??, it provides a full picture of the telescope pointing and sky conditions at the time of observation.

The `CcdVisit` catalog contains entries summarizing data for all 16071 `visit_images`.

- The `Calibration` catalog is the reference catalog that was used to perform astrometric and photometric `calibration`. It is a whole-sky catalog built specifically for `LSST`, as no single prior reference catalog had both the depth and coverage needed to calibrate `LSST` data. It combines data from multiple previous reference catalogs and contains only stellar sources. Full details on how the `Calibration` catalog was built are provided in P. S. Ferguson et al. (2025) ⁹³. We provide a brief summary here.

For the *grizy* bands, the input catalogs were (in order of decreasing priority): Dark Energy Survey (DES) Y6 Calibration Stars (E. S. Rykoff et al. 2023); Gaia-B or R Photometry (Gaia) (XP) Synthetic Magnitudes (Gaia Collaboration et al. 2023a); the Panoramic Survey Telescope and Rapid Response System (Pan-STARRS)1 3PI Survey (K. C. Chambers et al. 2016); Data Release 2 of the SkyMapper survey (C. A. Onken et al. 2019); and Data Release 4 of the VLT Survey Telescope (VST) Asteroid Terrestrial-impact Last Alert System (ATLAS) survey (T. Shanks et al. 2015). For the *u*-band, the input catalogs were (in order of decreasing priority): Standard Stars from Sloan Digital Sky Survey (SDSS) Data Release 16 (R. Ahumada et al. 2020); Gaia-XP Synthetic Magnitudes (Gaia Collaboration et al. 2023a); and synthetic magnitudes generated using Single Lens Reflex (SLR), which estimates the *u*-band `flux` from the *g*-band `flux` and *g-r* colors. This `SLR` estimates were used to boost the number of *u*-band reference sources, as otherwise the

⁹³ In P. S. Ferguson et al. (2025), the calibration reference catalog is referred to as “The Monster”. This terminology is also carried over to the `DP1` Butler.

source density from the *u*-band input catalogs is too low to be useful for the [LSST](#).

Only stellar sources were selected from each input catalog. Throughout, the `Calibration` catalog uses the [DES](#) bandpasses for the *grizy* bands and the [SDSS](#) bandpass for the *u*-band; color transformations derived from high quality sources were used to convert fluxes from the various input catalogs (some of which did not use the [DES/SDSS](#) bandpasses) to the respective bandpasses. All sources from the input catalogs are matched to [Gaia-Data Release 3 \(DR3\)](#) sources for robust astrometric information, selecting only isolated sources (i.e., no neighbors within 1").

After collating the input catalogs and transforming the fluxes to the standard [DES/SDSS](#) bandpasses, the catalog was used to identify sources within a specific region of the sky. This process generated a set of standard columns containing positional and flux information, along with their associated uncertainties.

3.2.1. Source and Object Designations

To refer to individual sources or objects from the DP1 catalogs, one should follow the LSST DP1 naming convention that has been registered with the International Astronomical Union. Because the `Source`, `Object`, `Di-aSource`, `DiaObject`, and `SSObject` tables each have their own unique IDs, their designations should differ. In general, source designations should begin with the string “LSST-DP1” (denoting the Legacy Survey of Space and Time, Data Preview 1), followed by a string specifying the table from which the source was obtained. These strings should be “O” (for the `Object` table), “S” (`Source`), “DO” (`DiaObject`), “DS” (`Di-aSource`), or “SSO” (`SSObject`). Following the table identifier, the designation should contain the full unique numeric identifier from the specified table (i.e., the `objectId`, `sourceId`, `diaObjectId`, `diaSourceId`, or `ssObjectId`). Each component of the identifier should be separated by dashes, resulting in a designation such as “LSST-DP1-TAB-123456789012345678”. In summary, source designations should adhere to the formats listed below:

- Object: LSST-DP1-O-609788942606161356 (for `objectId` 609788942606161356)
- Source: LSST-DP1-S-600408134082103129 (for `sourceId` 600408134082103129)
- DiaObject: LSST-DP1-DO-609788942606140532 (for `diaObjectId` 609788942606140532)

- DiaSource: LSST-DP1-DS-600359758253260853 (for `diaSourceId` 600359758253260853)
- SSObject: LSST-DP1-SSO-21163611375481943 (for `ssObjectId` 21163611375481943)

Tables that were not explicitly mentioned in the description above do not have their own unique IDs, but are instead linked to one of the five tables listed above via a unique ID. For example, the `ForcedSource` table is keyed on `objectId`, `ForcedSourceOnDiaObject` uses `diaObjectId`, `SSSource` is linked to `diaSourceId` and `ssObjectId`, and `MPCORB` uses `ssObjectId`.

3.3. Survey Property Maps

Maps are two-dimensional visualizations of survey data. In DP1, these fall into two categories: Survey Property Maps and [Hierarchical Progressive Survey \(HiPS\)](#) Maps (P. Fernique et al. 2015). Survey Property Maps ([NSF-DOE Vera C. Rubin Observatory 2025p](#)) summarize how properties such as observing conditions or exposure time vary across the observed sky. Each map provides the spatial distribution of a specific quantity at a defined sky position for each band by aggregating information from the images used to make the `deep_coadd`. Maps are initially created per `tract` and then combined to produce a final consolidated map. At each sky location, represented by a spatial pixel in the [Hierarchical Equal-Area iso-Latitude Pixelisation \(HEALPix\)](#) (K. M. Górski et al. 2005) grid, values are derived using statistical operations, such as minimum, maximum, mean, weighted mean, or sum, depending on the property.

DP1 contains 14 survey property maps. The available maps describe total exposure times, observation epochs (one each for the earliest, mean, and latest observation epoch), `PSF` size and `shape` (one for each of the e^1 and e^2 shape parameters; see §5.2), `PSF` magnitude limits, sky `background` and noise levels, as well as astrometric shifts (one each for right ascension and declination) and `PSF` distortions (one for each of the e^1 and e^2 shape parameters) due to wavelength-dependent atmospheric [Differential Chromatic Refraction \(DCR\)](#) effects. They all use the dataset type format `deep_coadd_<PROPERTY>_consolidated_map_-<STATISTIC>`. For example, `deep_coadd_exposure_time_consolidated_map_sum` provides a spatial map of the total exposure time accumulated per sky position in units of seconds. All maps are stored in `HealSparse`⁹⁴

⁹⁴ A sparse `HEALPix` representation that efficiently encodes data values on the celestial sphere. <https://healsparse.readthedocs.io>

format. Survey property maps are only available via the Data Butler (§6.2.2).

Figure 10 presents three survey property maps for exposure time, PSF magnitude limit, and sky noise, computed for representative tracts and bands. Because full consolidated maps cover widely separated tracts, we use clipped per-tract views here to make the spatial patterns more discernible.

3.4. HiPS Maps

HiPS Maps (P. Fernique et al. 2015), offer an interactive way to explore seamless, multi-band tiles of the sky regions covered by DP1, allowing for smooth panning and zooming. DP1 provides multi-band HiPS images created by combining data from individual bands of `deep_coadd` and `template_coadd` images, using an improved version (Lust et al. in prep) of the algorithm presented in R. Lupton et al. (2004). These images are false-color representations generated using various filter combinations for the red, green, and blue channels.

The available filter combinations include *gri*, *izy*, *riz*, and *ugr* for both `deep_coadd` and `template_coadd`. Additionally, for `deep_coadd` only, we provide color blends such as *uug* and *grz*. Post-DP1, we plan to also provide single-band HiPS images for all *ugriz* bands in both Portable Network Graphics (PNG) and Flexible Image Transport System (FITS) formats.

HiPS maps are only accessible through the HiPS viewer in the Rubin Science Platform (RSP) Portal (§6.3) and cannot be accessed via the Data Butler (§6.2.2). All multi-band HiPS images are provided in PNG format.

3.5. Metadata

DP1 also includes metadata about the observations, which are stored in the `Visit` table. We distinguish it from a catalog as the data it contains was produced by the observatory directly, rather than the science pipelines. The `Visit` table contains technical data for each visit, such as telescope pointing, camera rotation, airmass, exposure start and end time, and total exposure time. Some of the information contained within the `Visit` table is also contained in the `CCDVisit` catalogue described in §3.2 (e.g., exposure time), although the latter also includes information produced by the processing pipelines at a per-detector level, such as the PSF size and limiting magnitudes of a given `visit_image`.

3.6. Ancillary Data Products

DP1 also includes several ancillary data products. While we do not expect most users to need these, we describe them here for completeness. All the Data Prod-

ucts described in this section can only be accessed via the Data Butler (§6.2.2).

3.6.1. Standard Bandpasses

Figure 3 shows the full-system throughput of the six LSSTComCam filters. The corresponding transmission curves are provided as a DP1 data product. These datasets tabulate the full-system transmission of the six LSSTComCam filters as a function of wavelength and were used as a reference for the LSSTComCam DP1 photometry. The `standard_passband` dataset is keyed by band and is stored in Astropy Table format.

3.6.2. Task configuration, log, and metadata

DP1 includes provenance-related data products such as task logs, configuration files, and task metadata. Configuration files record the parameters used in each processing task, while logs and metadata contain information output during processing. These products help users understand the processing setup and investigate potential processing failures.

3.6.3. Calibration Data Products

Calibration data products include a variety of images and models that are used to characterize and correct the performance of the camera and other system components. These include bias, dark, and flat-field images, Photon Transfer Curve (PTC) gains, brighter-fatter kernels (P. Antilogus et al. 2014), charge transfer inefficiency (CTI) models, linearizers, and illumination corrections. For flat-field corrections, DP1 processing used combined flats, which are averaged from multiple individual flat-field exposures to provide a stable calibration. These calibration products are essential inputs to Instrument Signal Removal (ISR) (§4.2.1). While these products are included in DP1 for transparency and completeness, users should not need to rerun ISR for their science and are advised to start with the processed `visit_image`.

4. DATA RELEASE PROCESSING

Data Release Processing (DRP) is the systematic processing of all Rubin Observatory data collected up to a certain date to produce the calibrated images, catalogs of detections, and derived data products described in Section 3. DP1 was processed entirely at the United States Data Facility (USDF) at SLAC using 17,024 CPU hours.⁹⁵

⁹⁵ For future Data Releases, data processing will be distributed across the USDF, the French (FrDF) and UK (UKDF) data facilities.

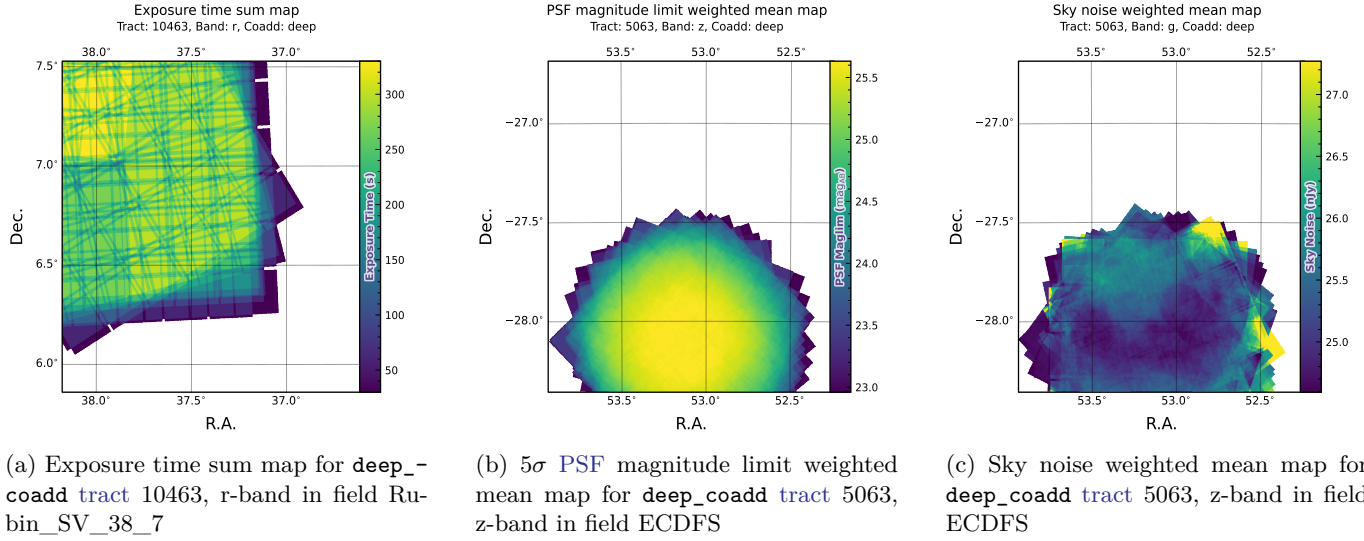


Figure 10. Examples of survey property maps from Rubin DP1 across different bands, clipped to the boundary of a single tract for visual clarity.

1408 This section describes the pipeline algorithms used to
 1409 produce DP1 and how they differ from those planned for
 1410 full-scale LSST data releases. Data Release Production
 1411 consists of four major stages: (1) single-frame process-
 1412 ing, (2) calibration, (3) coaddition, and (4) difference
 1413 image analysis (DIA).

4.1. LSST Science Pipelines Software

1415 The LSST Science Pipelines software (Rubin Observatory
 1416 [Science Pipelines Developers 2025](#); J. D. Swinbank
 1417 [et al. 2020](#)) will be used to generate all Rubin Observatory
 1418 and LSST data products. It provides both the [algorithms](#) and [middleware](#) frameworks necessary to process
 1419 raw data into science-ready products, enabling analysis
 1420 by the Rubin scientific community. Version v29.1 of the
 1421 pipelines was used to produce DP1⁹⁶.

4.2. Single Frame Processing

4.2.1. Instrument Signature Removal

1425 The first step in processing LSSTComCam images is
 1426 to correct for the effects introduced by the telescope and
 1427 detector. Each sensor and its readout amplifiers can
 1428 vary slightly in performance, causing images of even a
 1429 uniformly illuminated focal plane to exhibit discontinu-
 1430 ities and shifts due to detector effects. The [ISR](#) pipeline
 1431 aims to recover the original astrophysical signal as best
 1432 as possible and produce science-ready single-epoch im-
 1433 ages for source detection and measurement. A detailed
 1434 description of the [ISR](#) procedures can be found in P.
 1435 [Fagrelius & E. S. Rykoff \(2025\)](#); A. A. Plazas Malagón

1436 [et al. \(2025\)](#). Figure 11 illustrates the model of detector
 1437 components and readout electronics and their impact
 1438 on the signal, tracing the process from photons incident
 1439 on the detector surface to the final quantized values⁹⁷
 1440 recorded in the image files. The [ISR pipeline](#) essen-
 1441 tially “works backward” through the signal chain, cor-
 1442 recting the integer analog-to-digital units (ADU) raw
 1443 camera output back to a floating-point number of photo-
 1444 electrons created in the silicon. The physical detector,
 1445 shown on the left in Figure 11, is the source of effects
 1446 that arise from the silicon itself, such as the dark current
 1447 and the brighter-fatter effect (A. A. Plazas [et al. 2018](#);
 1448 A. Broughton [et al. 2024](#)). After the integration time
 1449 has elapsed, the charge is shifted to the serial register
 1450 and read out, which can introduce charge transfer inef-
 1451 ficiencies and a clock-injected offset level. The signals
 1452 for all amplifiers are transferred via cables to the [Read-
 1453 out Electronics Board \(REB\)](#), during which crosstalk
 1454 between the amplifiers may occur. The [Analog Signal
 1455 Processing Integrated Circuit \(ASIC\)](#) on the REB con-
 1456 verts the analog signal from the detector into a digital
 1457 signal, adding both quantization and a bias level to the
 1458 image. Although the signal chain is designed to be sta-
 1459 ble and linear, the presence of numerous sources of non-
 1460 linearity indicates otherwise.

1461 The [ISR](#) processing pipeline for DP1 performs, in
 1462 the following order: [Analogue-to-Digital Unit \(ADU\)](#)
 1463 dithering to reduce quantization effects, serial over-
 1464 scan subtraction, saturation masking, gain normaliza-
 1465 tion, crosstalk correction, parallel overscan subtraction,

⁹⁶ Documentation for this version is available at: https://pipelines.lsst.io/v/v29_1_1

⁹⁷ The images written to disk by the camera have values that are integers that come from the ADC converting an analog voltage.

linearity correction, serial **CTI** correction, image assembly, bias subtraction, dark subtraction, brighter-fatter correction, defect masking and interpolation, variance plane construction, flat fielding, and amplifier offset (amp-offset) correction⁹⁸. Flat fielding for **DP1** was performed using combined flats produced from twilight flats acquired with sufficient rotational dithering to mitigate artifacts from print-through stars, as described in §2.3.

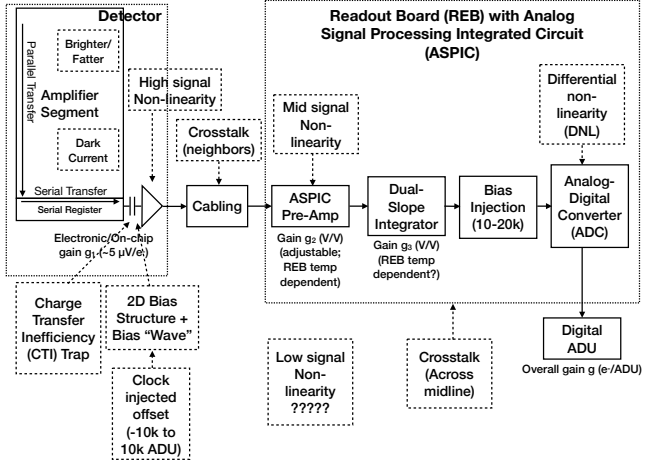


Figure 11. The model of the detector and REB components, labeled with the effects that they impart on signal.

4.2.2. Background Subtraction

The background subtraction algorithms in the LSST Science Pipelines estimate and remove large-scale background signals from science imaging. Such signals may include sky brightness from airglow, moonlight, scattered light instrumental effects, zodiacal light, and diffuse astrophysical emission. In so doing, true astrophysical sources are isolated to allow for accurate detection and measurement.

To generate a **background** model, each post-ISR image is divided into superpixels of 128×128 pixels. Pixels with a mask flag set that indicates that they contain no useful science data or that they contain **flux** from a preliminary source detection are masked. The iterative 3σ clipped mean of the remaining pixels is calculated for each superpixel, constructing a **background** statistics image. A sixth-order Chebyshev polynomial is fit to these values on the scale of a single detector to allow for

⁹⁸ Amp-offset corrections are designed to address systematic discontinuities in background sky levels across amplifier boundaries. The implementation in the LSST Science Pipelines is based on the Pan-STARRS Pattern Continuity algorithm (C. Z. Waters et al. 2020).

an extrapolation back to the native pixel resolution of the post-ISR image.

4.3. Calibration

Stars are detected in each post-ISR image using a 5σ threshold. Detections of the same star across multiple images are then associated to identify a consistent set of isolated stars with repeated observations suitable for use in PSF modeling, photometric **calibration**, and astrometric **calibration**.

Initial astrometric and photometric solutions are derived using only the calibration reference catalogs (see §3.2), and an initial **PSF** model is fit using PSFEx (E. Bertin 2011). These preliminary solutions provide approximate source positions, fluxes, and **PSF** shapes that serve as essential inputs to the **calibration** process, enabling reliable source matching, selection of high-quality stars, and iterative refinement of the final astrometric, photometric, and **PSF** models. These preliminary solutions are subsequently replaced by more accurate fits, as described in the following sections.

4.3.1. PSF Modeling

PSF modeling in **DP1** uses the Piff (M. Jarvis et al. 2021) package. Our configuration of Piff utilizes its **PixelGrid** model with a fourth-order polynomial interpolation per **CCD**, except in the *u*-band, where star counts are insufficient to support a fourth-order fit. In this case, a second-order polynomial is used instead. Details on the choice of polynomial order, overall **PSF** modeling performance, and known issues are discussed in §5.2.

4.3.2. Astrometric Calibration

Starting from the astrometric solution calculated in single frame processing (§4.2), the final astrometric solution is computed using the ensemble of visits in a given band that overlap a given **tract**. This allows the astrometric solution to be further refined by using all of the isolated point sources of sufficient signal-to-noise ratio in an image, rather than only those that appear in the reference catalog, as is done in single frame processing. Using multiple whole visits rather than a single detector also allows us to account for effects that impact the full focal plane, and for the proper motion and parallax of the sources.

In order to perform the fit of the astrometric solution, isolated point sources are associated between overlapping visits and with the Gaia DR3 (Gaia Collaboration et al. 2023b) reference catalog where possible. The model used for **DP1** consists of a static map from pixel space to an intermediate frame (the per-detector model), followed by a per-visit map from the intermediate frame

1541 to the plane tangent to the telescope boresight (the per-
 1542 visit model), then finally a deterministic mapping from
 1543 the tangent plane to the sky. The fit is done using the
 1544 `gbdes` package (G. M. Bernstein et al. 2017), and a full
 1545 description is given in C. Saunders (2024).

1546 The per-detector model is intended to capture quasi-
 1547 static characteristics of the telescope and camera. During
 1548 [Rubin Operations](#), the astrometric solution will al-
 1549 low for separate epochs with different per-detector mod-
 1550 els, to account for changes in the camera due to warm-
 1551 ing and cooling and other discrete events. However, for
 1552 [DP1](#), [LSSTComCam](#) was assumed to be stable enough
 1553 that all visits use the same per-detector model. The
 1554 model itself is a separate two-dimensional polynomial for
 1555 each detector. For [DP1](#), a degree 4 polynomial was used;
 1556 the degree of the polynomial mapping is tuned for each
 1557 instrument and may be different for LSSTCam. Fur-
 1558 ther improvements may be made by including a pixel-
 1559 based astrometric offset mapping, which would be fit
 1560 from the ensemble of astrometric residuals, but this is
 1561 not included in the [DP1](#) processing.

1562 The per-visit model attempts to account for the path
 1563 of a photon from both atmospheric sources and those
 1564 dependent on the telescope orientation. This model is
 1565 also a polynomial mapping, in this case a degree 6 two-
 1566 dimensional polynomial. Correction for [DCR](#) (§5.4) was
 1567 not done for [DP1](#), but will be included in LSSTCam pro-
 1568 cessing during [Rubin Operations](#). Future processing will
 1569 also likely include a Gaussian Process fit to better ac-
 1570 count for atmospheric turbulence, as was demonstrated
 1571 by W. F. Fortino et al. (2021) and P. F. Léget et al.
 1572 (2021).

1573 The final component of the astrometric [calibration](#)
 1574 involves the positions of the isolated point sources in-
 1575 cluded in the fit, which are described by five parameters:
 1576 sky coordinates, proper motion, and parallax. While
 1577 proper motions and parallaxes are not released for [DP1](#),
 1578 they are fitted for these sources in the astrometric solu-
 1579 tion to improve the astrometric calibration.

4.3.3. Photometric Calibration

1580 Photometric [calibration](#) of the [DP1](#) dataset is based
 1581 on the [Forward Global Calibration Method \(FGCM\)](#)
 1582 (FGCM D. L. Burke et al. 2018), adapted for the LSST
 1583 Science Pipelines (H. Aihara et al. 2022; P. Fagrelius &
 1584 E. S. Rykoff 2025). We used the [FGCM](#) to calibrate
 1585 the full [DP1](#) dataset with a forward model that uses a
 1586 parameterized model of the atmosphere as a function of
 1587 airmass along with a model of the instrument through-
 1588 put as a function of wavelength. The [FGCM](#) process
 1589 typically begins with measurements of the instrumental
 1590 throughput, including the mirrors, filters, and detectors.

1591 However, because full scans of the [LSSTComCam](#) as-
 1592 built filters and individual detectors were not available,
 1593 we instead used the nominal reference throughputs for
 1594 the Simonyi Survey Telescope and LSSTCam.⁹⁹ These
 1595 nominal throughputs were sufficient for the [DP1](#) cal-
 1596ibration, given the small and homogeneous focal plane
 1597 consisting of only nine [ITL](#) detectors. The FGCM atmo-
 1598 sphere model, provided by MODTRAN (A. Berk et al.
 1599 1999), was used to generate a look-up table for atmo-
 1600 spheric throughput as a function of zenith distance at
 1601 Cerro Pachón. This model accounts for absorption and
 1602 scattering by molecular constituents of the atmosphere,
 1603 including O_2 and O_3 ; absorption by water vapor; and
 1604 Mie scattering by airborne aerosol particulates. Nightly
 1605 variations in the atmosphere are modeled by minimiz-
 1606 ing the variance in repeated observations of stars with
 1607 a [Signal to Noise Ratio \(SNR\)](#) greater than 10, mea-
 1608 sured using “compensated aperture fluxes”. These fluxes
 1609 include a local [background](#) subtraction (see §4.2.2) to
 1610 mitigate the impact of [background](#) offsets. The model
 1611 fitting process incorporates all six bands (*ugrizy*) but
 1612 does not include any gray (achromatic) terms, except
 1613 for a linear assumption of mirror reflectance degra-
 1614 dation, which is minimal over the short duration of the
 1615 [DP1](#) observation campaign. As an additional constraint
 1616 on the fit, we use a subset of stars from the reference
 1617 catalog (P. S. Ferguson et al. 2025), primarily to con-
 1618 strain the system’s overall throughput and establish the
 1619 “absolute” calibration.

4.4. Visit Images and Source Catalogs

1620 With the final [PSF](#) models, [WCS](#) solutions, and pho-
 1621 tometric calibrations in place, we reprocess each single-
 1622 epoch image to produce a final set of calibrated visit
 1623 images and source catalogs. Source detection is per-
 1624 formed down to a 5σ threshold using the updated [PSF](#)
 1625 models, followed by measurement of [PSF](#) and aperture
 1626 fluxes. These catalogs represent the best single-epoch
 1627 source characterization, but they are not intended for
 1628 constructing light curves. For time-domain analysis,
 1629 we recommend using the [forced photometry](#) tables de-
 1630 scribed in §4.6.2.

4.5. Coaddition Processing

4.5.1. Coaddition

1631 Only exposures with a [seeing](#) better than 1.7 arcsec-
 1632 onds FWHM are included in the deep coadded images.
 1633 For the template coadds, typically only the top third of
 1634 visits with the best [seeing](#) are used (although see §3.1 for

⁹⁹ Available at: <https://github.com/lsst/throughputs/tree/1.9>

more details), resulting in an even tighter image quality cutoff for the template coadds. Exposures with poor PSF model quality, identified using internal diagnostics, are excluded to prevent contamination of the coadds with unreliable PSF estimates. The remaining exposures are combined using an inverse-variance weighted mean stacking algorithm.

To mitigate transient artifacts before coaddition, we apply the artifact rejection procedure described in Y. Al-Sayyad (2018) that identifies and masks features such as satellite trails, optical ghosts, and cosmic rays. It operates on a time series of PSF-matched images resampled onto a common pixel grid (“warps”) and leverages their temporal behavior to distinguish persistent astrophysical sources from transient artifacts.

Artifact rejection uses both direct (where no PSF-matching is performed) and PSF-matched warps, homogenized to a standard PSF of 1.8 arcseconds FWHM, broadly consistent with the 1.7 arcsecond FWHM seeing threshold used in data screening. A sigma-clipped mean of the PSF-matched warps serves as a static sky model, against which individual warps are differenced to identify significant positive and negative residuals. Candidate artifact regions are classified as transient if they appear in less than a small percentage of the total number of exposures, with the threshold based on the number of visits, N , as follows:

- $N = 1$ or 2 : threshold = 0 (no clipping).
- $N = 3$ or 4 : threshold = 1.
- $N = 5$: threshold = 2.
- $N > 5$: threshold = $2 + 0.03N$.

Identified transient regions are masked before coaddition, improving image quality and reducing contamination in derived catalogs.

4.5.2. Detection, Deblending and Measurement

After constructing coadded images, sources are detected in each band, merged across bands, deblended, and measured to generate the final object catalogs (§3.2). For each coadd in all six bands, we perform source detection at a 5σ detection threshold and then adjust the background with a per-patch constant (coadds are built from background-subtracted images, but the deeper detection on coadds redefines what is considered source versus background). Detections across bands are merged in a fixed priority order, *irzygu*, to form a union detection catalog, which serves as input to deblending.

Deblending is performed using the Scarlet Lite algorithm, which implements the same model as Scarlet (P.

Melchior et al. 2018), but operates on a single pixel grid. This allows the use of analytic gradients, resulting in greater computational speed and memory efficiency.

Object measurement is then performed on the deblended detection footprints in each band. Measurements are conducted in three modes: independent per-band measurements, forced measurements in each band, and multiband measurements.

Most measurement algorithms operate through a single-band plugin system, largely as originally described in J. Bosch et al. (2018). The same plugins are run separately for each object on a deblended image, which uses the Scarlet model as a template to re-weight the original noisy coadded pixel values. This effectively preserves the original image in regions where objects are not blended, while dampening the noise elsewhere.

A reference band is chosen for each object based on detection significance and measurement quality using the same priority order as detection merging (*irzygu*) and a second round of measurements is performed in forced mode using the shape and position from the reference band to ensure consistent colors (J. Bosch et al. 2018).

Measurement algorithm outputs include object fluxes, centroids, and higher-order moments thereof like sizes and shapes. A variety of flux measurements are provided, from aperture fluxes and forward modeling algorithms.

Composite model (CModel) magnitudes (K. Abazajian et al. 2004; J. Bosch et al. 2018) are used to calculate the extendedness parameter, which functions as a star-galaxy classifier. Extendedness is a binary classifier that is set to 1 if the PSF model flux is less than 98.5% of the (free, not forced) CModel flux in a given band. Additionally, the extendedness in the reference band is provided as a separate column for convenience as a multiband star-galaxy classification, and is recommended generally but also specifically for objects with low signal-to-noise ratio in some bands.

Gaussian-Aperture-and-PSF (Gaussian Aperture and PSF (GAaP) K. Kuijken 2008; A. Kannawadi 2025) fluxes are provided to ensure consistent galaxy colors across bands. Sérsic model (J. L. Sérsic 1963; J. L. Sersic 1968) fits are run on all available bands simultaneously (MultiProFit, D. S. Taranu 2025). The resulting Sérsic model fluxes are provided as an alternative to CModel and are intended to represent total galaxy fluxes. Like CModel, the Sérsic model is a Gaussian mixture approximation to a true Sérsic profile, convolved with a Gaussian mixture approximation to the PSF. Sérsic model fits also include a free centroid, with all other structural parameters shared across all bands. That is, the intrinsic model has no color gradients, but the convolved

1740 model may have color gradients if the PSF parameters
 1741 vary significantly between bands.

1742 CModel measurements use a double “shapelet” (A.
 1743 Refregier 2003) PSF model with a single shared shape.
 1744 The Sérsic fits are intended to use a double Gaussian
 1745 with independent shape parameters for each component.
 1746 Due to a pipeline misconfiguration, the Sérsic fits actu-
 1747 ally used the shapelet PSF parameters, with the higher-
 1748 order terms ignored (since MultiProFit does not sup-
 1749 port shapelet PSFs). This bug is not expected to im-
 1750 pact the galaxy fluxes significantly, since the higher-
 1751 order shapelet PSF parameters tend to be small, and
 1752 the fix will be applied in future campaigns. Either way,
 1753 the double Gaussian PSF parameters are included for
 1754 each object.

1755 Further details on the performance of these algorithms
 1756 are found in §5.7.

1757 4.6. Variability Measurement

1758 4.6.1. Difference Imaging Analysis

1759 Difference Image Analysis (DIA) uses the decorrelated
 1760 Alard & Lupton image differencing algorithm (D. J.
 1761 Reiss & R. H. Lupton 2016). We detected both pos-
 1762 itive and negative DIASources at 5σ in the difference
 1763 image. Sources with footprints containing both positive
 1764 and negative peaks due to offsets from the template po-
 1765 sition or blending were fit with a dipole centroid code,
 1766 which simultaneously fits offset positive and negative
 1767 PSFs.

1768 We filter a subset of DIASources that have pixel
 1769 flags characteristic of artifacts, non-astrophysical trail
 1770 lengths, and unphysically negative direct fluxes. We
 1771 performed a simple spatial association of DIASources
 1772 into DIAObjects with a one arcsecond matching radius.

1773 The Machine Learning reliability model applied to
 1774 DP1 was developed with the aim to meet the latency
 1775 requirements for Rubin Alert Production when executed
 1776 on CPUs. Accordingly we developed a relatively simple
 1777 model: a Convolutional Neural Network with three con-
 1778 volutional layers, and two fully connected layers. The
 1779 convolutional layers have a 5×5 kernel size, with 16, 32,
 1780 and 64 filters, respectively. A max-pooling layer of size 2
 1781 is applied at the end of each convolutional layer, followed
 1782 by a dropout layer of 0.4 to reduce overfitting. The last
 1783 fully connected layers have sizes of 32 and 1. The ReLU
 1784 activation function is used for the convolutional layers
 1785 and the first fully connected layer, while a sigmoid func-
 1786 tion is used for the output layer to provide a probabilistic
 1787 interpretation. The cutouts are generated by extracting
 1788 postage stamps of 51×51 pixels centered on the detected
 1789 sources. The input data of the model consist of the tem-
 1790 plate, science, and difference image stacked to have an

1791 array of `shape` (3, 51, 51). The model is implemented
 1792 using PyTorch (J. Ansel et al. 2024). The Binary Cross
 1793 Entropy loss function was used, along with the **Adap-
 1794 tive Moment Estimation (Adam)** optimizer with a fixed
 1795 learning rate of 1×10^{-4} , weight decay of 3.6×10^{-2} , and
 1796 a batch size of 128. The final model uses the weights
 1797 that achieved the best precision/purity for the test set.
 1798 Training was done on the **SLAC Shared Scientific Data
 1799 Facility (S3DF)** with an NVIDIA model L40S GPU.

1800 The model was initially trained using simulated data
 1801 from the second DESC Data Challenge (DC2; (LSST
 1802 Dark Energy Science Collaboration (LSST DESC) et al.
 1803 2021)) plus randomly located injections of PSFs to in-
 1804 crease the number of real sources, for a total of 89,066
 1805 real sources. The same number of bogus sources were se-
 1806 lected at random from non-injected DIASources. Once
 1807 the **LSSTComCam** data were available, the model was
 1808 fine-tuned on a subset of the data containing 183,046
 1809 sources with PSF injections. On the **LSSTComCam** test
 1810 set, the model achieved an accuracy of 98.06%, purity
 1811 of 97.87%, and completeness of 98.27%. As discussed
 1812 in §5.8, the injections used to train this model version
 1813 do not capture all types of astrophysical variability, so
 1814 performance on the test set will not be representative
 1815 for variable stars, comets, and other types of variable
 1816 objects.

1817 4.6.2. Light Curves

1818 To produce light curves, we perform multi-epoch
 1819 **forced photometry** on both the direct visit images and
 1820 the difference images. For light curves we recom-
 1821 mend the **forced photometry** on the difference images
 1822 (`psDiffFlux` on the **ForcedSource Table**), as it isolates
 1823 the variable component of the flux and avoids contam-
 1824 ination from static sources. In contrast, **forced pho-**
 1825 **1826 tometry** on direct images includes flux from nearby or
 1827 blended static objects, and this contamination can vary
 1828 with seeing. Centroids used in the multi-epoch **forced**
 1829 **1830 photometry** stage are taken either from object positions
 measured on the coadds or from the DIAObjects (the
 associated DIASources detected on difference images).

1831 4.6.3. Solar System Processing

1832 Solar system processing in DP1 consists of two key
 1833 components: the association of observations (sources)
 1834 with known solar system objects, and the discovery of
 1835 previously unknown objects by linking sets of *track-
 1836 lets*¹⁰⁰.

¹⁰⁰ A tracklet is defined as two or more detections of a moving object candidate taken in close succession in a single night.

To generate expected positions, ephemerides are computed for all objects found in the Minor Planet Center orbit catalog using the `Sorcha` survey simulation toolkit (Merritt et al., in press)¹⁰¹. To enable fast lookup of objects potentially present in an observed visit, we use the `mpsky` package (M. Juric 2025). In each image, the closest DiaSource within 1 arcsecond of a known solar system object’s predicted position is associated to that object.

Solar system discovery uses the `heliolinx` package of asteroid identification and linking tools (A. Heinze et al. 2023). The suite consists of the following tasks:

- Tracklet creation with `make_tracklets`
- Multi-night `tracklet` linking with `heliolinc`
- Linkage post processing (orbit fitting, outlier rejection, and de-duplication) with `link_purify`

The inputs to the `heliolinx` suite included all sources detected in difference images produced by an early processing of the LSSTComCam commissioning data, including some that were later rejected as part of DP1 processing and hence are not part of DP1.

About 10% of all commissioning visits targeted the near-ecliptic field Rubin_SV_38_7 chosen to facilitate asteroid discovery. Rubin_SV_38_7 produced the vast majority of asteroid discoveries in DP1, as expected, but a few were found in off-ecliptic fields as well.

Tracklet creation with `make_tracklets` used an upper limit angular velocity of 1.5 deg/day, faster than any main belt asteroid and in the range of many Near-Earth Object (NEO) discoveries. To minimize false tracklets from fields observed multiple times per night, the minimum `tracklet` length was set to three detections, and a minimum on-sky motion of five arcseconds was required for a valid `tracklet`.

The heart of the discovery pipeline is the `heliolinc` task, which connects (“links”) tracklets belonging to the same object over a series of nights. It employs the Heliolinc3D algorithm (S. Eggl et al. 2020; A. Heinze et al. 2022), a refinement of the original Heliolinc algorithm of M. J. Holman et al. (2018).

The `heliolinc` run tested each `tracklet` with 324 different hypotheses spanning heliocentric distances from 1.5 to 9.8 astronomical unit (au) and radial velocities spanning the full range of possible bound orbits (eccentricity 0.0 to nearly 1.0). This range of distance encompasses all main belt asteroids and Jupiter Trojans, as well as many comets and Mars-crossers and

some NEOs. Smaller heliocentric distances were not attempted here because nearby objects move rapidly across the sky and hence were not likely to remain long enough in an LSSTComCam field to be discovered. Candidate linkages, groups of tracklets whose propagated orbits cluster within a radius of 1.33×10^3 au at 1 au, are identified, then post-processed via `link_purify` to yield a final, non-overlapping set of high-confidence asteroid candidates, ranked by orbit-fit residuals and related metrics.

5. PERFORMANCE CHARACTERIZATION AND KNOWN ISSUES

In this section, we provide an assessment of the DP1 data quality and known issues.

5.1. Sensor Anomalies and ISR

In addition to the known detector features identified before LSSTComCam commissioning, most of which are handled by the ISR processing (see §4.2.1), we discovered a number of new types of anomalies in the DP1 data. Since no corrections are currently available for these anomalies, they are masked and excluded from downstream data products.

5.1.1. Vampire Pixels

“Vampire” pixels are visible on the images as a bright defect surrounded by a region of depressed flux, as though the defect is stealing charge from its neighboring pixels. Figure 12 shows an example of a vampire pixel near the center of R22_S11 on an *r*-band flat.

From studies on evenly illuminated images, vampires appear to conserve charge. Unfortunately, no unique optimum way exists to redistribute this stolen flux so, following visual inspection, a defect mask was created to exclude them from processing. We have found some similar features on the ITL detectors on LSSTCam, and will use the same approach to exclude them.

5.1.2. Phosphorescence

Some regions of the LSSTComCam CCD raft were seen to contain large numbers of bright defects. An example is shown in Figure 13 in a *g*-band flat. On further investigation, it appears that on some detectors a layer of photoresist wax was incompletely removed from the detector surface during production. As this wax is now trapped below the surface coatings, there is no way to physically clean these surfaces. If this wax responded to all wavelengths equally, then it would likely result in quantum efficiency dips, which might be removable during flat correction. However, it appears that this wax is slightly phosphorescent, with a decay time on the order

¹⁰¹ Available at <https://github.com/dirac-institute/sorcha>

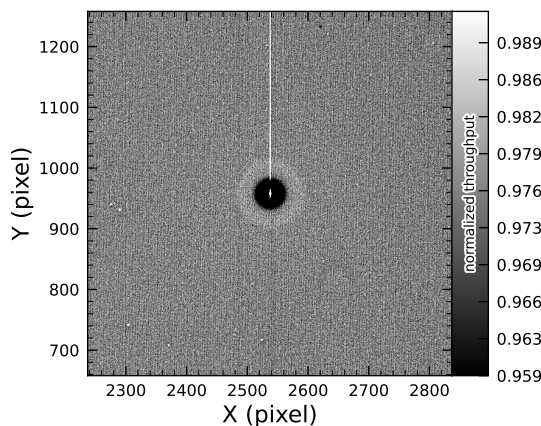


Figure 12. A large vampire pixel near the center of R22_S11, as seen on the *r*-band flat. This clearly shows the central hot "vampire" pixels, surrounded by a region of depressed signal, with a brighter ring surrounding that caused by the local electric field effects. The charge contained in the central pixels is incompletely shifted as the image is read, and that charge leaks out into subsequent rows as they are shifted through the remnant charge. The columns that contain the hot pixels are masked as defects in all processing, as this feature cannot be otherwise corrected.

1933 of minutes, resulting in the brightness of these defects
 1934 being dependent on the illumination of prior exposures.
 1935 The worst of these regions were excluded with manual
 1936 masks.

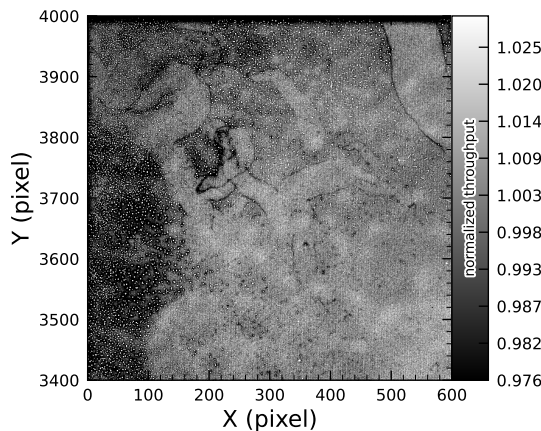


Figure 13. The top left corner of R22_S01 in the *g*-band flat, showing the many small defect features that are caused by the remnant photoresist wax. A single large defect box masks this region from further analysis to prevent these features from contaminating measurements.

1937

1938

5.1.3. Crosstalk

1939 Crosstalk refers to unwanted signal interference between adjacent pixels or amplifiers. We use an average inter-amp crosstalk correction based on laboratory 1940 measurements with LSSTCam. These average corrections 1941 proved satisfactory, and so have been used as-is 1942 for DP1 processing. There are, however, some residual 1943 crosstalk features present post-correction, with a 1944 tendency towards over-subtraction. [Figure 14](#) shows an 1945 example of a bright star with over-subtracted crosstalk 1946 residuals visible on neighboring amplifiers to both sides 1947 on exposure 2024120600239, detector R22_S02. 1948 1949 1950

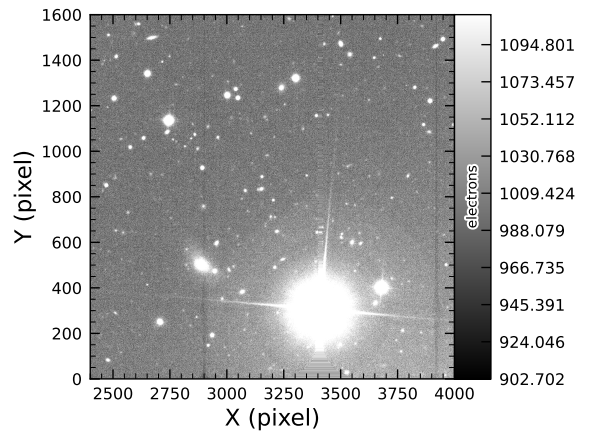


Figure 14. An example of a bright star with over-subtracted crosstalk residuals visible on neighboring amplifiers to both sides (exposure 2024120600239, detector R22_S02). The horizontal banding stretching from the center of the star shows the interpolation pattern covering the saturated core and the ITL edge bleed near the serial register.

5.1.4. Bleed Trails

1951 Bleed trails are produced when charge from saturated 1952 pixels spills into adjacent pixels. Bleed trails were 1953 anticipated on LSSTComCam sensors, but they appear in 1954 more dramatic forms than had been expected. As a 1955 bleed trail nears the serial register, it fans out into a 1956 "trumpet" shaped feature. Although bright, these 1957 features do not have consistently saturated pixels. In DP1 1958 these "edge bleeds" were identified and masked.

1959 Saturated sources can create a second type of bleed, 1960 where the central bleed drops below the background 1961 level. The depressed columns along these trails extend 1962 across the entire readout column of the detector, crossing 1963 the detector mid-line. We developed a model for 1964 these to identify which sources are sufficiently saturated 1965 to result in such a trail, which is then masked. As this 1966 kind of trail appears only on the ITL detectors, we've 1967 1968 1969

named these features “ITL dips”. Figure 15 shows an example of a bright star exhibiting the “ITL dip” phenomenon on exposure: 2024121000503, detector: R22_S21.

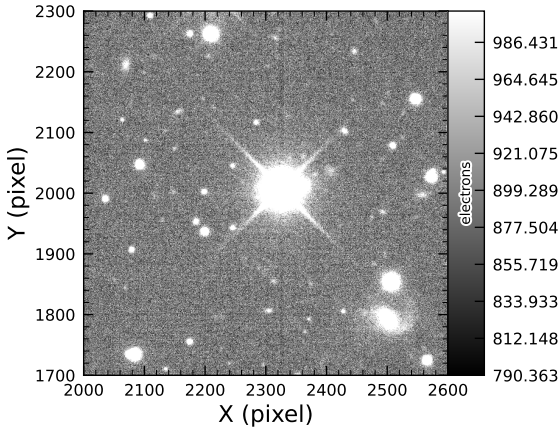


Figure 15. A bright star showing the “ITL dip” phenomenon, in which a dark trail extends out from the star to the top and bottom edges of the detector (exposure: 2024121000503, detector: R22_S21).

1974
1975

5.2. PSF Models

1977 To characterize PSF performance, we use adaptive
1978 second moments (G. M. Bernstein & M. Jarvis 2002)
1979 measured on PSF stars and on the PSF model using
1980 the HSM implementation (C. Hirata & U. Seljak 2003;
1981 R. Mandelbaum et al. 2005). All measurements are ex-
1982 pressed in the pixel coordinate frame of each detector.
1983 We characterize the performance of the PSF using the
1984 classical trace of the second moment matrix T , along
1985 with the ellipticity parameters e^1 and e^2 . Measure-
1986 ments on the observed PSF stars are denoted as
1987 T_{PSF} , e_{PSF}^1 , e_{PSF}^2 , while those from PSF models are de-
1988 noted as T_{model} , e_{model}^1 , e_{model}^2 . We compare two PSF
1989 modeling approaches:

- Piff with second-order polynomial interpolation (Piff O2), the pipeline’s default, and
- Piff with fourth-order polynomial interpolation (Piff O4), which serves as the final DP1 PSF model.

1995 Table 5 summarizes each model’s ability to reconstruct
1996 the mean T , e^1 , and e^2 on LSSTComCam. Both models
1997 exhibit a negative residual bias in the reconstructed PSF
1998 size, with Piff O4 providing improved performance over
1999 Piff O2.

2001 An alternative approach to evaluating the perfor-
2002 mance of the PSF model is to examine the average $\delta T/T$,

Table 5. Observed mean values and comparison of model residuals, across all visits and filters

Quantity	Observed	Piff O2	Piff O4
$\langle T \rangle$ (pixel ²)	11.366 ± 0.003		
$\langle e^1 \rangle$	$(-6.07 \pm 0.05) \times 10^{-3}$		
$\langle e^2 \rangle$	$(-4.57 \pm 0.05) \times 10^{-3}$		
$\langle e \rangle$	$(8.794 \pm 0.004) \times 10^{-2}$		
$\langle \delta T/T \rangle$		-4.0 ± 0.2	-5.0 ± 0.2
$\langle \delta e^1 \rangle$		0.6 ± 0.1	0.5 ± 0.1
$\langle \delta e^2 \rangle$		0.0 ± 0.1	0.0 ± 0.1

2003 where δT is $T_{\text{PSF}} - T_{\text{model}}$, across visits, projected onto
2004 focal-plane coordinates, as shown in Figure 16. Piff re-
2005 veals strong spatial correlations in the residuals, includ-
2006 ing a systematic offset consistent with the results pre-
2007 sented in Table 5. The presence of these spatial struc-
2008 tures motivated the adoption of fourth-order polynomial
2009 interpolation in all bands except u -band. Although not
2010 shown in Figure 16, residual patterns persist even with
2011 third-order interpolation, indicating that it is insuffi-
2012 cient to capture the complexity of the PSF variation.
2013 Increasing the interpolation order to five would nomi-
2014 nally reduce the residuals further, but the limited num-
2015 ber of stars available on some CCDs would not provide
2016 adequate constraints for such a model, while the result-
2017 ing improvement would likely be minimal. Preliminary
2018 analysis of LSSTCam data in the laboratory at SLAC
2019 National Accelerator Laboratory (SLAC) shows that the
2020 ITL sensors exhibit the same pattern as ITL sensors on
2021 LSSTComCam.

2022 Another way to look at the PSF modeling quality is
2023 via whisker plots of the PSF second and fourth moments
2024 and their modeling residuals projected on a part of the
2025 sky. In addition to the second moment, the spin-2 fourth
2026 moments, $e^{(4)}$, are defined as:

$$e_1^{(4)} = M_{40} - M_{04}$$

$$e_2^{(4)} = 2(M_{31} - M_{13}),$$

2028 where M_{pq} are the standardized higher moments as de-
2029 fined in T. Zhang et al. (2023) measured on stars and
2030 PSF models. Figure 17 shows the whisker plots of e ,
2031 $e^{(4)}$ (top rows), and δe , $\delta e^{(4)}$ in the ECDFS field. The
2032 direction of a whisker represents the orientation of the
2033 shape, while the length represents the amplitude $|e|$ or
2034 $|e^{(4)}|$. We observe coherent patterns in both the PSF
2035 moments and the residuals, the latter of which warrants
2036

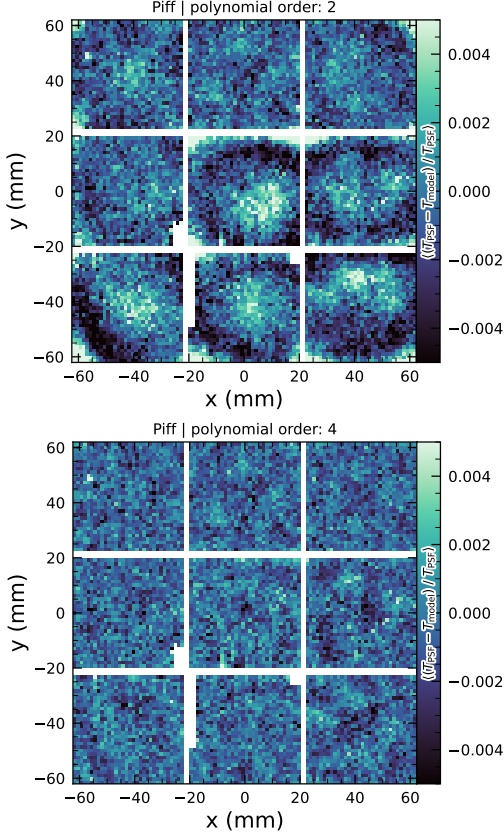


Figure 16. Average across all visits of $\delta T/T$ for Piff O2 and Piff O4 modeling on LSSTComCam. Averages are computed using a 120×120 binning.

further investigation if it persists in future data releases.

2038

2039

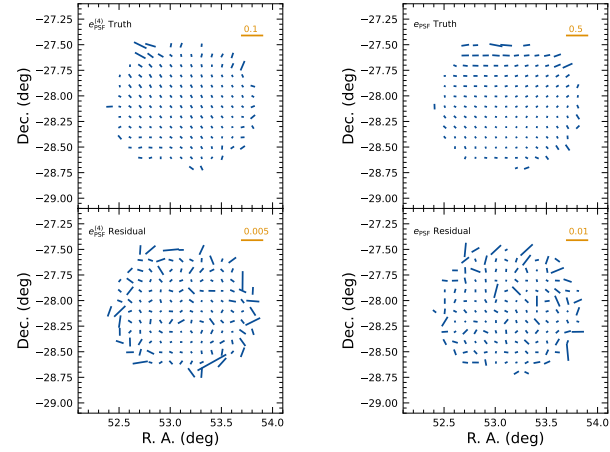


Figure 17. Whisker plots for the ECDFS field for e , $e^{(4)}$ and δe , $\delta e^{(4)}$.

2042
2043
2044
2045
2046
2047
2048
2049
2050
2051

Figure 18 shows a plot of $\delta T/T$ versus stellar magnitude, which can reveal any dependencies between PSF size and flux. We also repeat this analysis in color bins to probe chromatic effects. Binning by color uncovers a clear color dependence, as was also seen in DES (M. Jarvis et al. 2021). The residual is consistent with Table 5 and its cause is unknown. DP1 does not include the color correction implemented in the DES Year 6 analysis, T. Schutt et al. (2025). This will be included in processing of future data releases.

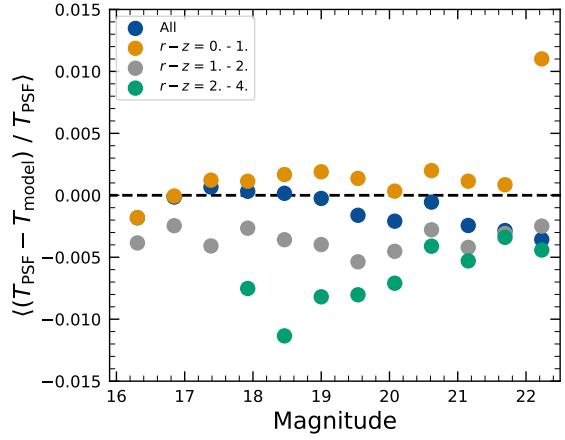


Figure 18. Binned $\delta T/T$ as a function of magnitude across all visits and filters and in bins of stellar colors.

2052
2053
2054
2055
2056
2057
2058
2059
2060
2061

As noted in Rubin Observatory Science Pipelines Developers (2025), two key Piff features were not used in the DP1 processing. PSF color dependence was not implemented, and, while Rubin software allows Piff to work with sky coordinates (including WCS transformations), it does not yet correct for sensor-induced astrometric distortions such as tree rings (H. Y. Park et al. 2017). Both features are planned for upcoming releases.

5.3. Astrometry

2062
2063
2064
2065
2066
2067
2068
2069
2070
2071
2072
2073
2074
2075

To characterize astrometric performance, we evaluate both internal consistency and agreement with an external reference. The primary measure of internal consistency is the repeatability of position measurements for the same object, defined as the RMS of the astrometric distance distribution for stellar pairs having a specified separation in arcminutes. We associate isolated point sources across visits and compute the rms of their fitted positions, rejecting any stars with another star within $2''$. Figure 19 shows the median per-tract rms astrometric error in RA for all isolated point sources, both after the initial calibration and after the final calibration, which includes proper motion corrections. The results indicate that the astrometric solution is already

2077 very good after the initial calibration. Global calibration
 2078 yields only modest improvement, likely due to the
 2079 short time span of DP1 and the minimal distortions
 2080 in the LSSTComCam. In the main survey, the longer
 2081 time baseline and greater distortions near the LSSTCam
 2082 field edges will make global calibration more impactful.
 2083 An additional measure of internal consistency is the re-

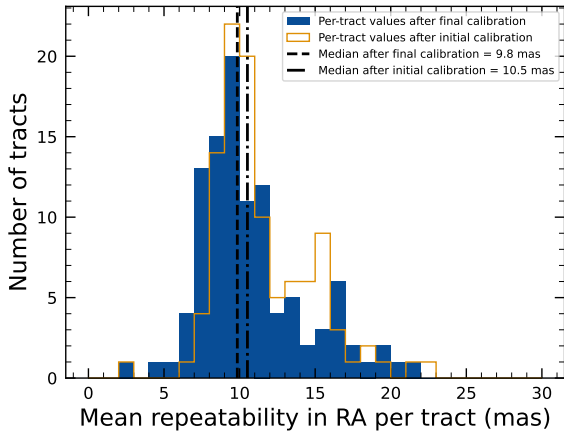


Figure 19. Mean per-tract astrometric repeatability of measurements of isolated point sources in RA in visits across all bands.

2084
 2085
 2086 peatability of separations between objects at a given dis-
 2087 tance. To compute this, we identify pairs of objects that
 2088 are separated by a specified distance and measure their
 2089 precise separation during each visit in which both ob-
 2090 jects are observed. The scatter in these separation mea-
 2091 surements provides an indication of the internal consis-
 2092 tency of the astrometric model. [Figure 20](#) shows the
 2093 median separation for pairs of objects separated by ap-
 2094 proximately 5 arcminutes, computed per tract after the
 2095 final calibration. These values are already approaching
 2096 the design requirement of 10 mas.

2097 To assess external consistency, we consider the median
 2098 separation between sources not included in the astromet-
 2099 ric fit and associated objects from a reference catalog.
 2100 For this, we use the Gaia DR3 catalog, with the object
 2101 positions shifted to the observation epoch using the Gaia
 2102 proper motion parameters. [Figure 21](#) shows the median
 2103 separation for each visit in the *r*-band in tract 4849 in
 2104 the ECDFS fields ([Table 6](#)). The calculated values are
 2105 almost all within 5 mas, well below the design require-
 2106 ment of 50 mas for the main survey. By examining the
 2107 astrometric residuals, we can assess whether there are
 2108 distortions not accounted for by the astrometric model.
 2109 In some cases, residuals from a single visit exhibit behav-
 2110 ior consistent with atmospheric turbulence, as shown in
 2111 [Figure 22](#), which is characterized by a curl-free gradient

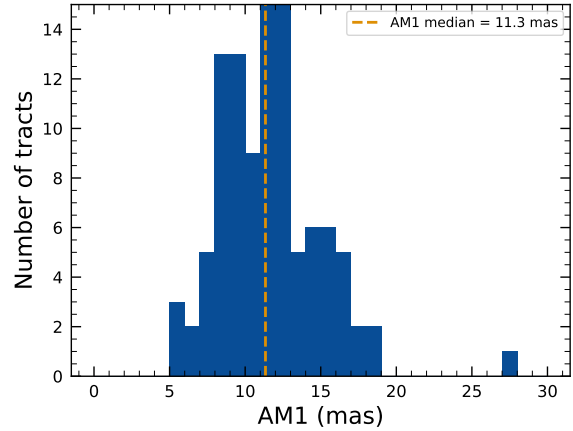


Figure 20. Median per-tract repeatability in separations between isolated point sources 5 arcmin apart in visits across all bands.

2114 field in the two-point correlation function of the resi-
 2115 als (E-mode), P. F. Léget [et al.](#) (2021) and W. F. Fortino
 2116 [et al.](#) (2021). However, as seen in [Figure 23](#), the resi-
 2117 als in many visits also have correlation functions with
 2118 a non-negligible divergence-free B-mode, indicating that
 2119 some of the remaining residuals are due to unmodeled
 2120 instrumental effects, such as rotations between visits.

2121 We can see unmodeled camera distortions by stacking
 2122 the astrometric residuals over many visits as a function
 2123 of the focal plane position. [Figure 24](#) shows the median
 2124 residuals in *x* and *y* directions for 1792 visits. Spatial
 2125 structures are evident at the CCD level, as well as at
 2126 the mid-line break, the discontinuity between the two
 2127 rows of amplifiers, in the *y*-direction residuals. Further
 2128 stacking all the detectors makes certain effects particu-
 2129 larly clear. [Figure 25](#) shows distortions very similar to
 2130 those measured for an LSSTCam ITL sensor in a labo-
 2131 ratory setting in J. H. Esteves [et al.](#) (2023).

2136 5.4. Differential Chromatic Refraction

2137 Differential Chromatic Refraction (DCR) occurs when
 2138 light passes through Earth’s atmosphere, refracting
 2139 more for shorter wavelengths, which causes blue light
 2140 to appear shifted closer to the zenith. This wavelength-
 2141 dependent effect results in the smearing of point sources
 2142 along the zenith direction, specifically parallel to the
 2143 parallactic angle. The DCR effect is observable in
 2144 LSSTComCam data, particularly in the angular offset
 2145 versus *g*–*i* band magnitude difference plots, as shown in
 2146 [Figure 26](#). These plots contain 228 visits chosen to max-
 2147 imize the range of observed airmass. When looking at
 2148 data perpendicular to the parallactic angle, sources ex-
 2149 hibit no discernible DCR effect, which is expected, and

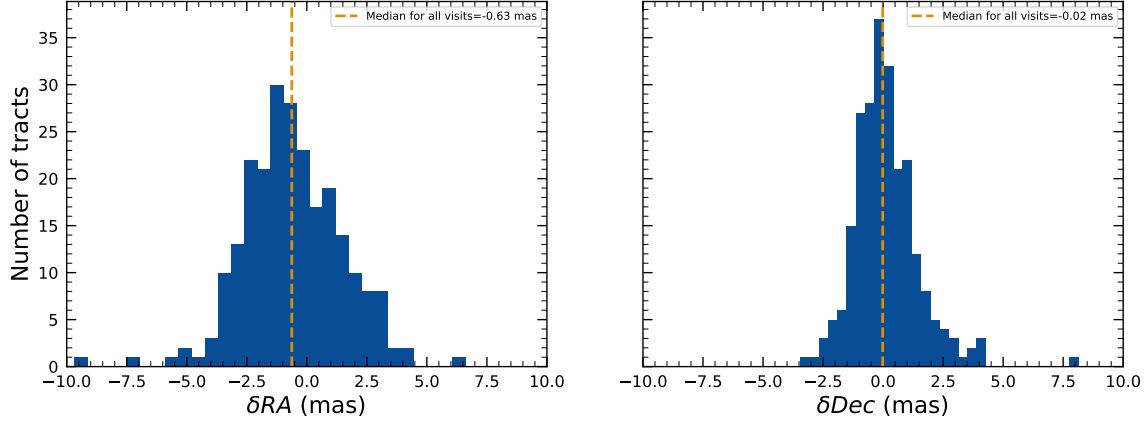


Figure 21. Median absolute offset for all visits in r -band in tract 4849 in the ECDFS field. The offset is the difference between the positions of isolated point sources that were reserved from the astrometric fit and matched objects from the Gaia DR3 catalog.

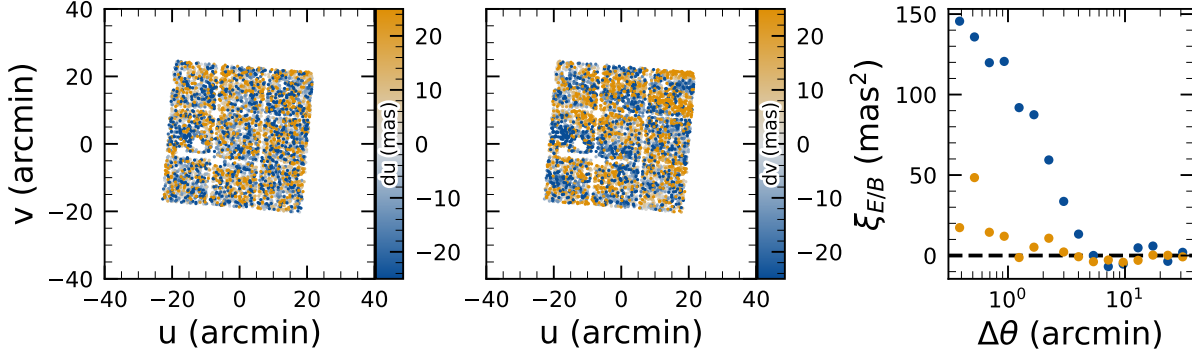


Figure 22. Astrometric residuals in u (left panel) and v (center panel) directions with the E (blue) and B (orange) modes of the two-point correlation function (right panel) seen in visit 2024120200359 in tract 2393 in u band. The residuals show a wave-like pattern characteristic of atmospheric turbulence, and there is significant E-mode and negligible B-mode in the correlation function.

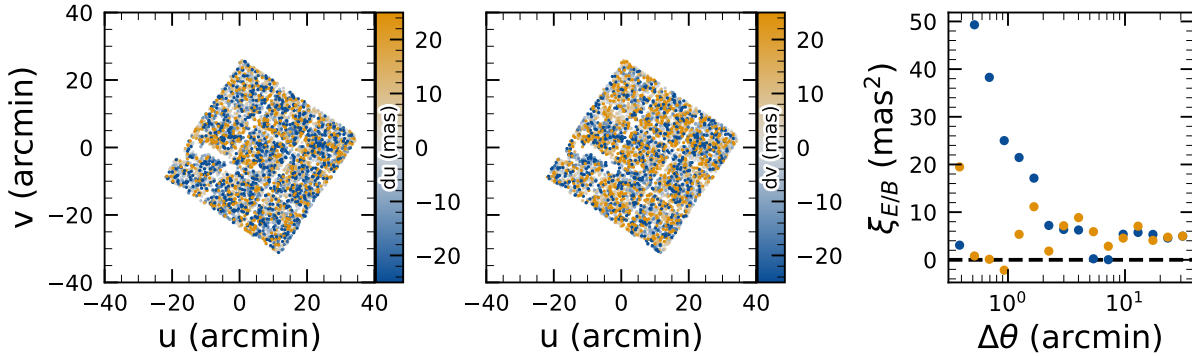


Figure 23. Astrometric residuals in u (left panel) and v (center panel) directions, with the E (blue) and B (orange) modes of the two-point correlation function (right panel) seen in visit 2024120700527 in tract 2393 in u band. There are coherent residuals, but without the wave-like pattern seen in Figure 22, and the correlation function has significant values for both E and B-modes.

2150 form a clear vertical distribution on the two-dimensional density plots in Figure 26.
 2151

2152 In contrast, sources aligned with the parallactic angle
 2153 exhibit a tilted, linear distribution, clearly demonst-

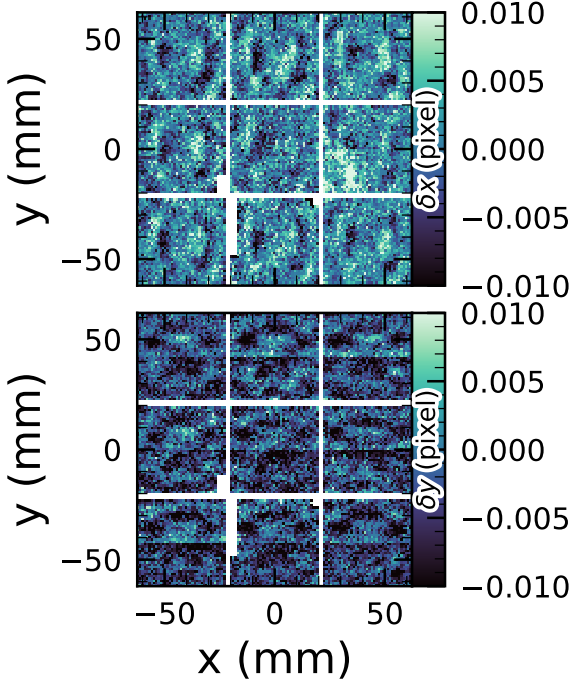


Figure 24. Median astrometric residuals as a function of focal plane position, shown in the left panel for the x direction and in the right panel for the y direction, for all nine LSSTComCam CCDs independently. The range of the color scale is ± 0.01 pixels, corresponding to 2 mas, showing that the effect is small.

ing that the relationship between angular offset and the $g - i$ band magnitude difference, thereby providing a visual indication of the **DCR** effect. The DCR effect will be addressed in future releases.

5.5. Stellar Photometry

The photometric repeatability for isolated bright unresolved sources following the **FGCM** fits was excellent. For the 10% of unresolved sources withheld from the fit and having signal-to-noise ratios greater than 100, the photometric repeatability after applying chromatic correction was 7.1, 5.4, 5.4, 5.1, 5.9, and 6.5 mmag in the *ugrizy* bands respectively, across all fields. After accounting for photometric noise, the intrinsic photometric repeatability was approximately 4.8, 2.7, 1.7, 1.0, 2.0, and 1.1 mmag in *ugrizy*. The DP1 processing does not yet include chromatic corrections in the final photometry. In this case the delivered photometric repeatability was 3–8 mmag for *grizy*.

In Figure 27, we show the stellar loci for *ugriz* for unresolved sources in the DP1 **Object** table (§3.2). These unresolved sources were selected using the extendedness parameter (§3.2) in the **Object** catalog. This parame-

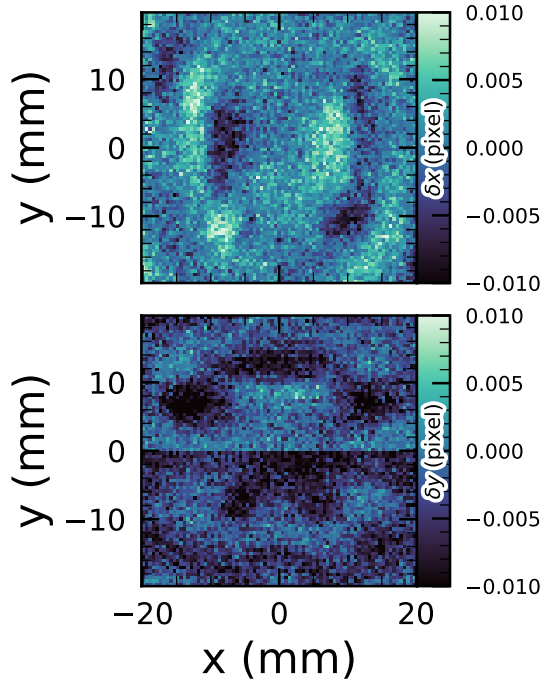


Figure 25. Median residuals as a function of pixel position, shown in the left panel for the x direction and in the right panel for the y direction. These residuals are aggregated across all nine CCDs that comprise the central LSSTComCam raft. The range of the color scale is ± 0.01 pixels, corresponding to 2 mas, showing that the effect is small.

ter is assigned a value of 0 (unresolved) or 1 (resolved) in each band based on the difference between the PSF and CModel magnitudes. The extendedness is set to 1 when this magnitude difference exceeds 0.016 mag, as the PSF flux for extended sources is biased low relative to the CModel flux. This method has been previously employed by the SDSS pipelines, and its statistical properties, including the optimal combination of information from different bands and repeated measurements, are discussed in C. T. Slater et al. (2020).

Figure 28 illustrates the behavior of the extendness parameter. Its behavior in the g and r bands is similar, with unresolved sources scattered around the vertical line centered on zero. The width of the distribution increases towards fainter magnitudes. Resolved sources are found to the right and the dashed lines in the top panels show the adopted “star-galaxy” separation boundary. The morphology of the two color-magnitude diagrams in the bottom panels suggest that the unresolved sample suffers from increasing contamination by galaxies for $r > 24$. This behavior is consistent with simulation-based predictions from C. T. Slater et al. (2020).

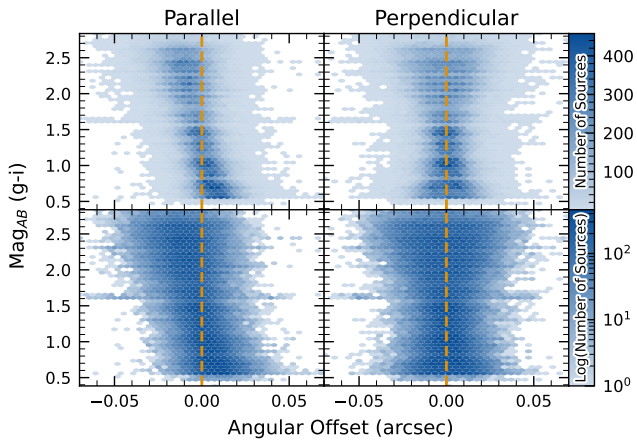


Figure 26. Visualization of Differential Chromatic Refraction (DCR) observed in the LSSTComCam commissioning campaign. The $g - i$ color is computed for every source in the reference catalog that is matched to a direct source in the science image, and the binned density for the full survey is plotted against the angular offset between the reference and detected positions. The angular offset is projected along coordinates parallel and perpendicular to the parallactic angle of the observation, and shows a characteristic correlation along the parallel axis with no correlation along the perpendicular axis. The orange vertical dashed line indicates the expected $g - i$ magnitude distribution at zero angular offset.

5.6. Detection Completeness on Coadds

We characterize completeness by injecting synthetic sources into coadded images, and by comparing source detections to external catalogs. In both cases, we use a greedy, probabilistic matching algorithm that matches reference objects, in order of descending brightness, to the most likely target within a $0.5''$ radius.

We inject sources in 12 of the patches of the ECDFS region with the deepest coverage. The input catalog contains stars and galaxies from part of the Data Challenge 2 (DC2) simulations (LSST Dark Energy Science Collaboration (LSST DESC) et al. 2021), where the galaxies consist of an exponential disk and de Vaucouleurs (G. de Vaucouleurs 1948, 1953) bulge. To avoid deblender failures from excessive increases in object density, stars with a total flux (i.e., summed across all six bands) brighter than 17.5 mag are excluded, as are galaxies whose total flux is brighter than 15 mag or fainter than 26.5 mag. Half of the remaining objects are selected for injection. Afterwards, individual bulge and disk components fainter than 29 mag are also excluded, both for computational expediency and because their structural properties are less likely to be representative of real galaxies.

Figure 29 shows completeness as a function of magnitude for these injected objects in the ECDFS field. These completeness estimates are comparable to results from matching external catalogs. Matching to the Hubble Legacy Field catalog (G. Illingworth et al. 2016; K. E. Whitaker et al. 2019) reaches 50% completeness at $F775W = 26.13$, or about $i = 25.83$ from differences in matched object magnitudes. Similarly, completeness drops below 90% at $VIS = 23.80$ from matching to Euclid Q1 (Euclid Collaboration et al. 2025) objects, equivalent to roughly $i = 23.5$. The Euclid imaging is of comparable or shallower depth, so magnitude limits at lower completeness percentages than 90% are unreliable, whereas the HST images cover too small and irregular of an area to accurately characterize 80-90% completeness limits.

At the 80% completeness limit, nearly 20% of objects, primarily injected galaxies, are incorrectly classified as stars based on their reference band extendedness. Similarly, the fraction of correctly classified injected stars drops to about 50% at $i = 23.8$ (corresponding to 90% completeness).

This analysis has several caveats. The selection of objects for matching in any catalog is not trivial. Some fraction of the detections are spurious, particularly close to bright stars and their diffraction spikes. Additionally, some objects lie in masked regions of one survey but not another, which has not been accounted for. For injected source matching, the reference catalog does not include real on-sky objects. Based on prior analyses of the DC2 simulations, purity is generally greater than completeness at any given magnitude. Similarly, for bright ($i < 23$) objects classified as stars by reference band extendedness, $< 5\%$ are either unmatched to a Euclid or HST object, or misclassified - that is, selecting on extendedness alone yields a fairly pure but incomplete sample of stars. We expect to remedy some of these shortcomings in future releases.

5.7. Model Flux and Shape Measurement

Figure 30 shows i -band magnitude residuals for CModel and Sérsic measurements using the matched injected galaxies described in §5.6. Similar behavior is seen in other bands. Sérsic fluxes show reduced scatter for galaxies with $i < 22.5$, though CModel fluxes are less biased, with median residuals closer to zero and less magnitude-dependent. For fainter objects, Sérsic fluxes are more biased and less accurate. The magnitude of this bias is considerably larger than previously seen in simulated data. Subsequent testing indicates that this bias can be (roughly) halved by fitting an exponential model first, and then using those parameters to initialize

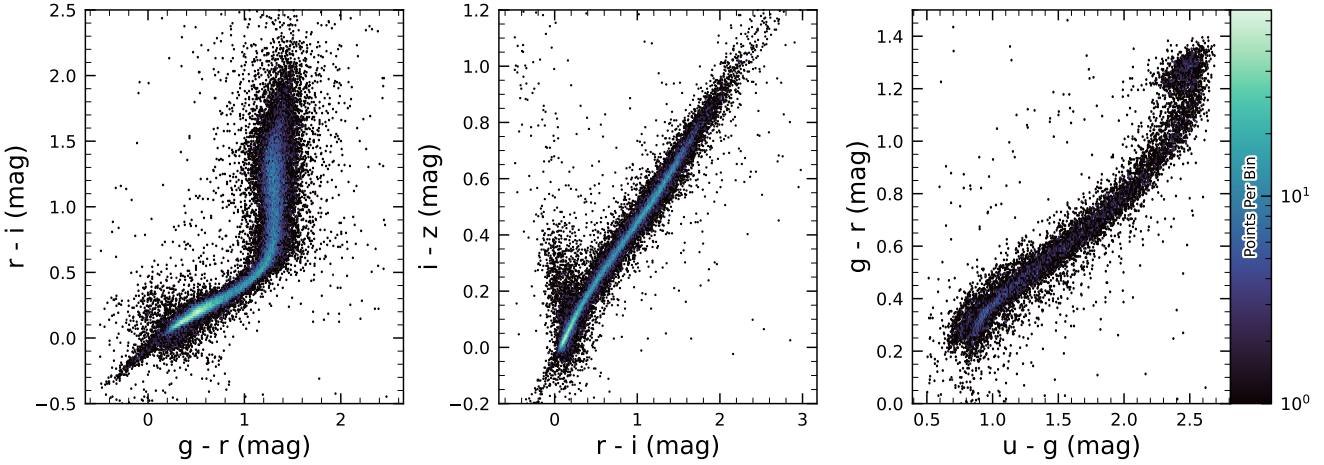


Figure 27. Examples of stellar loci for unresolved sources from the DP1 dataset. From left to right: gri stellar locus containing 63,236 stars with signal-to-noise ratio > 200 in the i band; riz stellar locus containing 46,760 stars with signal-to-noise ratio > 200 in the i band ugr stellar locus containing 12,779 stars with signal-to-noise ratio > 50 in the u band.

2276 a free Sérsic fit. This approach will be adopted in future
 2277 releases. Aperture fluxes - including Kron and [GAaP](#) -
 2278 are not shown as they are not corrected to yield total
 2279 fluxes. The correction for Kron fluxes can be derived
 2280 from the Sérsic index ([A. W. Graham & S. P. Driver](#)
 2281 2005), but this correction is not provided in object ta-
 2282 bles.

2283 [Figure 31](#) shows $g - i$ color residuals versus r -band
 2284 magnitude for the same sample of galaxies as [Figure 30](#).
 2285 For this and most other colors, [GAaP](#) (with a $1''$ aperture)
 2286 and Sérsic colors both yield lower scatter; however,
 2287 the CModel colors have the smallest bias. Curiously,
 2288 the [GAaP](#) bias appears to be magnitude-dependent,
 2289 whereas the Sérsic bias remains stable from $19 < r < 26$.
 2290 Any of these color measurements are suitable for use
 2291 for deriving quantities like photometric redshifts, stellar
 2292 population parameters, etc.

2293 In addition to photometry, some algorithms include
 2294 measurements of structural parameters like size, ellip-
 2295 ticity, and Sérsic index. One particular known issue is
 2296 that many (truly) faint objects have significantly overes-
 2297 timated sizes and fluxes. This was also seen in the Dark
 2298 Energy Survey ([K. Bechtol et al. 2025](#)), who dubbed
 2299 such objects “super-spreaders”. These super-spreaders
 2300 contribute significantly to overestimated fluxes at the
 2301 faint end (see e.g. [Figure 30](#)), and are particularly prob-
 2302 lematic for the Kron algorithm ([R. G. Kron 1980](#)), which
 2303 should only be used with caution.

2304 As mentioned in [§4.5](#), the Sérsic fits include a free
 2305 centroid, which is initialized from the fiducial centroid
 2306 of the object. Preliminary analyses of matched injected
 2307 objects suggest that the Sérsic model galaxy [astrom-](#)
 2308 [etry](#) residuals are somewhat smaller than for the stan-

2309 dard centroids used in other measurements, and so users
 2310 of the Sérsic photometry should also use these centroid
 2311 values. One caveat is that for faint objects and/or in
 2312 crowded regions with unreliable deblending, free cen-
 2313 troids can drift significantly and potentially towards
 2314 other objects, so objects with large differences between
 2315 the fiducial and Sérsic [astrometry](#) should be discarded
 2316 or used with caution.

2317 Sérsic model parameter uncertainties are estimated
 2318 by computing and inverting the Hessian matrix with
 2319 the best-fit parameter values, after replacing the pixel
 2320 data (but not uncertainties) by the best-fit model values.
 2321 Currently, only the on-diagonal dispersion term (square
 2322 root of the variance) is provided as an error estimate for
 2323 each parameter. Future releases may provide more off-
 2324 diagonal terms of the covariance matrix - particularly
 2325 for the structural parameters, which are known to be
 2326 correlated.

2327 A major outstanding issue is that many parameter
 2328 uncertainties - including but not limited to those for
 2329 fluxes - are underestimated. This is at least partly (but
 2330 not wholly) due to the fact that coaddition introduces
 2331 covariance between pixels, which is not captured in per-
 2332 pixel variances.

2333 The degree to which uncertainties are underestimated
 2334 can depend on the parameter in question and on the
 2335 brightness of the object. In plots of uncertainty-scaled
 2336 residuals, the ideal behavior is for the median (i.e. the
 2337 bias) to lie close to zero, and for the $\pm 1\sigma$ lines to lie at
 2338 ± 1 , without any dependence on magnitude. [Figure 32](#)
 2339 shows that flux and color uncertainties for PSF model
 2340 magnitudes of injected stars are both underestimated,
 2341 but by a factor of approximately $1.7 - 2$ that is not very

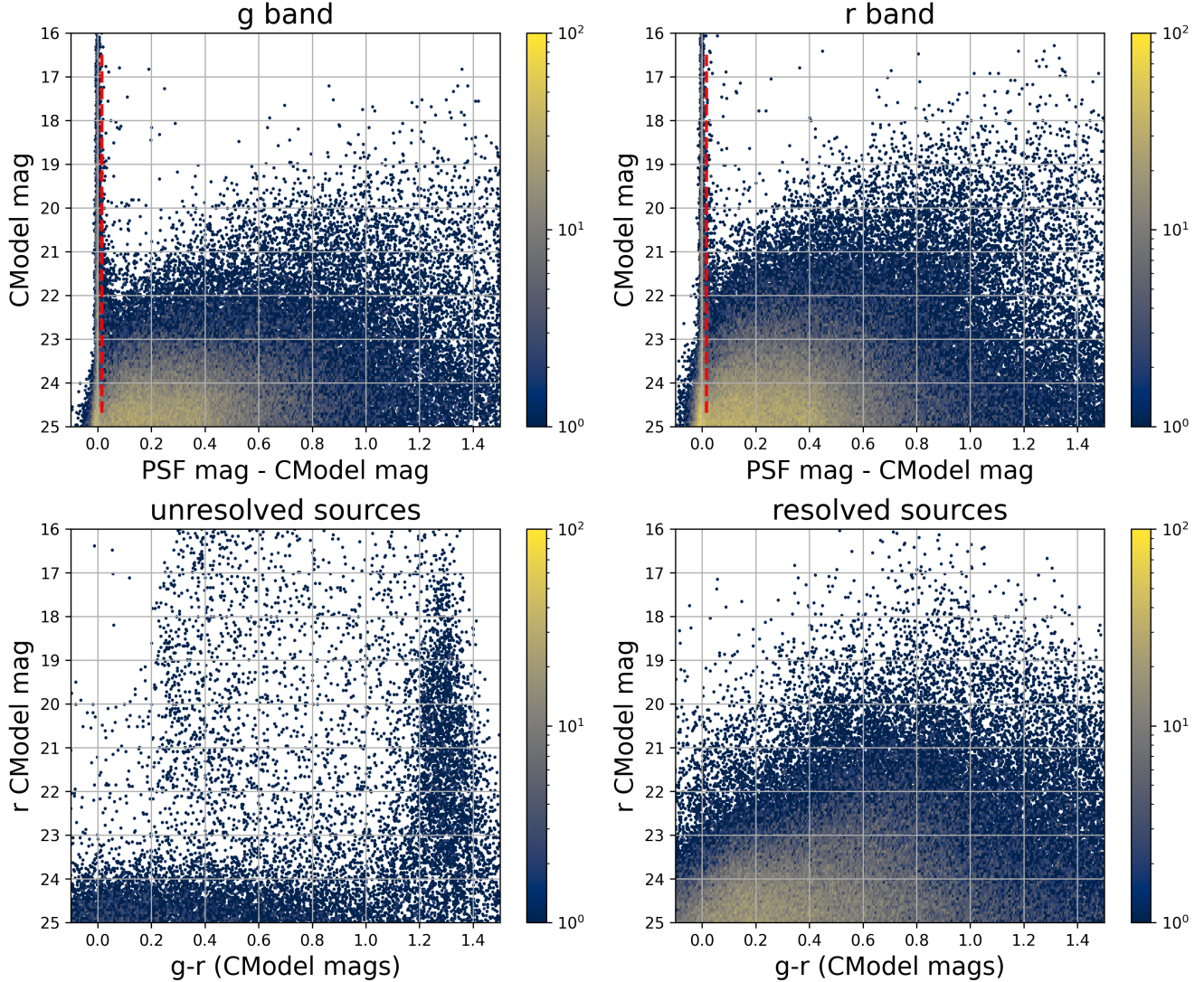


Figure 28. The top two panels shows the difference between the PSF and CModel magnitudes as a function of CModel magnitude in the g and r bands for 178,547 sources with $CModel_r < 25$ from the ECDFS field. The vertical dashed line in each panel marks the minimum value (0.016 mag) for setting the extendedness parameter to 1. The bottom two panels show the r vs. $g - r$ color-magnitude diagrams for 14,701 unresolved (left) and 163,666 resolved (right) sources. Note the unresolved sample suffers from increasing contamination by galaxies for $r > 24$.

2342 sensitive to **SNR**. This holds for astrometric/centroid
 2343 parameters as well.

2344 In turn, Figure 33 shows that CModel color uncertainties
 2345 of galaxies are underestimated by a similar factor at
 2346 the faint end, but with appreciable scaling with mag-
 2347 nitude (and thereby **SNR**). Flux error underestimation
 2348 is both larger than for colors and scales more strongly
 2349 with **SNR**. This indicates that systematic effects domi-
 2350 nate the errors in fluxes, particularly for bright galaxies.
 2351 This is also at least partly but not wholly due to so-
 2352 called model inadequacy - that is, the fact that galaxy
 2353 models, parameteric or otherwise, are insufficiently com-
 2354 plex to capture the structure of real galaxies.

2355 **Figure 34** shows that Sérsic model fluxes and colors
 2356 have similar behavior as CModel, but with a greater
 2357 degree of overestimation. This may be partly due to the
 2358 fact that Sérsic parameter uncertainties are estimated
 2359 along with the free centroid and structural (shape and
 2360 Sérsic index) parameters, whereas the forced CModel
 2361 fluxes and errors are derived from linear flux fits with a
 2362 fixed shape and centroid.

2363 Efforts are underway to investigate and quantify the
 2364 origin of uncertainty underestimates and future releases
 2365 will, at the least, provide recommendations for mitiga-
 2366 tions.

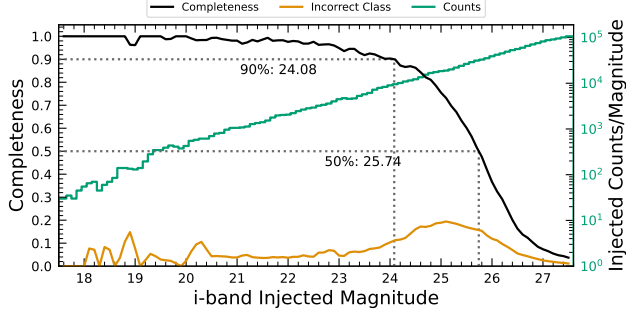


Figure 29. Completeness and incorrect classification fraction as a function of i -band CModel magnitude (Reference Magnitude) for DC2-based injected objects into a portion of the ECDFS field. The “Incorrect Class” line shows the proportion of objects that are matched but classified incorrectly by their reference-band extendedness, i.e. stars with extendedness of 1 or galaxies with extendedness of 0 in the reference band.

5.8. Difference Imaging Purity

We assessed the performance of image differencing using human vetting and source injection (§5.9). Members of the DP1 team labeled more than 9500 DIASource image triplets consisting of cutouts from the science, template, and difference images. We classified these into various real and artifact categories. The raw artifact to real ratio without filtering was roughly 9:1. Bright stars are the main source of artifacts. Correlated noise, primarily in u and g bands, also leads to spurious detections near the flux threshold. We expect to be able to mitigate these effects for LSSTCam.

Applying a reliability threshold improves the purity of transients but not variable stars; technical limitations at the time of model training prevented injection of variable stars into the synthetic training set. Reliability models, described in §4.6.1, for LSSTCam data will be trained on a wider range of input data.

5.9. Difference Imaging Detection Completeness

We assess the performance of our difference imaging pipeline using synthetic source injection on the science images prior to differencing. We construct a catalog of injected sources by joining two different samples of point sources, a set of hosted sources to emulate transients in galaxies and second set of hostless sources. The hosts are selected from the pipeline source catalog that is produced upstream by imposing a cut on their extendedness measurement and selecting $N_{\text{src}} = \min(100, N \times 0.05)$ of the N available sources per detector. For each host we pick a random position angle and radius using its light profile shape to decide where to place the source, and also a random value of brightness for the injected source, with magnitudes higher than the host source.

The hostless sources instead have random positions in the CCD focal plane, and magnitudes chosen from a random uniform distribution with $20 \geq m \geq m_{\text{lim}} + 1$, where m_{lim} is the limiting magnitude of the image. We used the LSST source_injection package¹⁰² to include these sources in our test images. We performed a coordinate cross-match task, with a threshold of $0''.5$ to find which of these sources were detected and which were lost, enabling the calculation of a set of performance metrics.

In Figure 35 we show the detection completeness as a function of the SNR, for sources in the ECDFS field, for filters $griz$. We observe a completeness $> 95\%$ for sources with $\text{SNR} > 6$, with mean completeness $\simeq 99\%$ and standard deviation of $\simeq 0.7\%$. In Figure 36 we show the distribution of the residuals of the recovered sky coordinates for the detected synthetic sources. The marginal distributions are both centered at zero, and for sources of $\text{SNR} > 20$ the residuals are compatible with normal distributions $\mathcal{N}(\mu = 0, \sigma^2 = (0''.02)^2)$. In Figure 37 we show photometry results for our detected synthetic sources in the i filter, using PSF photometry on the difference images. We include both the magnitude residuals as well as the flux pulls, defined as $f_{\text{PSF}} - f_{\text{True}})/\sigma_{f_{\text{PSF}}}$ for PSF flux f_{PSF} and error $\sigma_{f_{\text{PSF}}}$, as a function of the true magnitude of the synthetic sources, including the running median and median absolute deviation (MAD) for the whole brightness range. We also include the true magnitude distribution as well as the detection completeness on the top panel, and for reference the 90% and 50% completeness magnitude values in vertical lines. On the right panels we include the marginal distribution for sources brighter than $mag < 22.5$, splitting the data into hosted and hostless, as well as the robust mean and standard deviation. From this figure we can see that our flux measurements are accurate within a wide range of magnitudes, for both hosted and hostless synthetic sources. We find that the median offset is below 0.002 mag for true magnitudes below 21, and with a maximum σ_{MAD} scatter of about 0.02 mag in this range. For true $m_i < 22.5$, the robust running median PSF magnitudes residuals are < 0.02 mag, and when splitting into hosted and hostless both robust median are well below 0.01, and robust σ , i.e. σ_{MAD} are also well below 0.05. For all sources with $m_i < 21.5$ the running median is always $|\langle \delta \rangle| < 0.1$, and $\text{MAD } \sigma_{\delta} < 1$. Extending to sources with $m_i < 22.5$ then hostless sources have a robust mean pull below 0.02, with a robust standard deviation < 1.15 , while these

¹⁰² <https://pipelines.lsst.io/modules/lsst.source.injection/index.html>

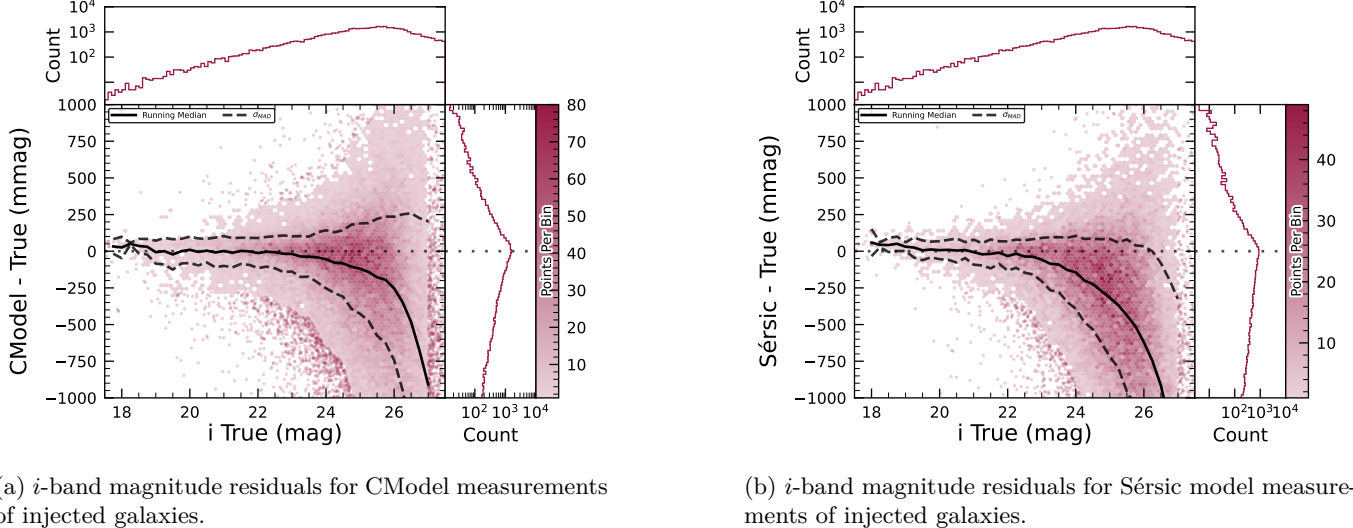


Figure 30. i -band magnitude residuals for matched injected DC2 galaxies with the CModel and Sérsic algorithms in a portion of the ECDFS region, including the median and scatter thereof. The black line is the median.

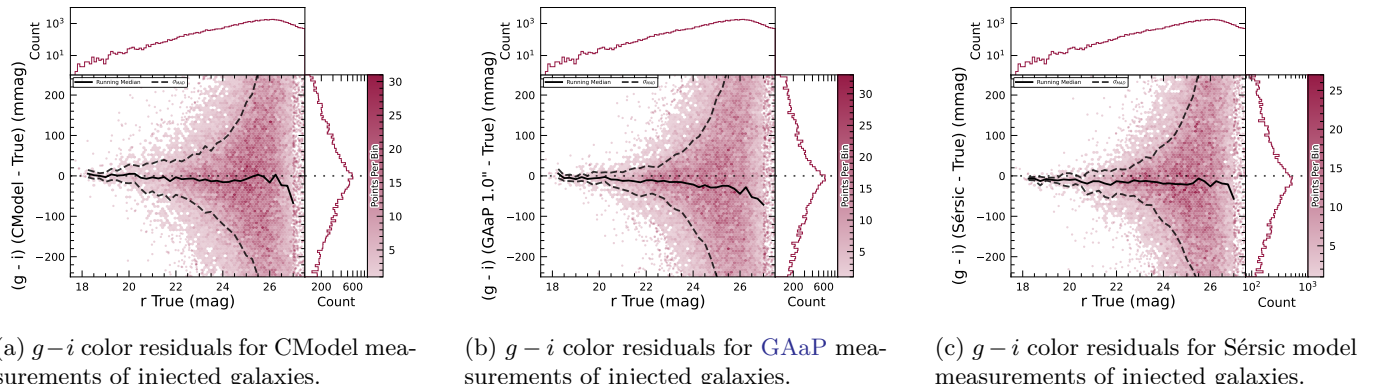


Figure 31. $g - i$ color residuals versus true r -band magnitude for matched injected DC2 galaxies with the CModel, GAAP and Sérsic algorithms in a portion of the ECDFS region.

parameters increase to 0.2 and 1.2 for hosted sources, suggesting that we might have contamination from host background sources potentially biasing our fluxes.

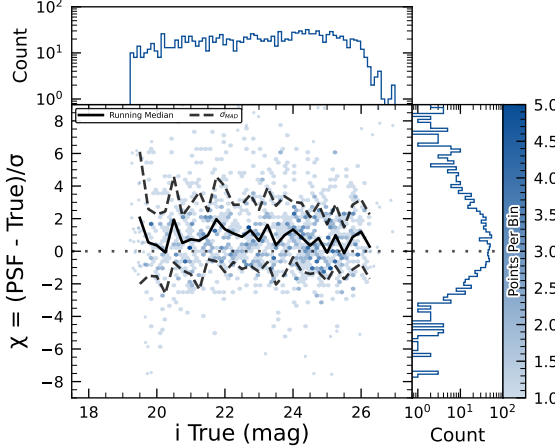
inspection of the linkages indicated that those ranked 0–137 corresponded to unique real asteroids; ranks 138–200 contained additional real objects intermixed with some spurious linkages; and ranks higher than 200 were essentially all spurious. This analysis indicates that it will be possible to identify cuts on quality metrics such as χ^2 to define discovery candidate samples with high purity; determining the exact quantitative cut values requires more data with LSSTCam. We next removed all observations matched to known asteroids (using Minor Planet Center (MPC)’s MPChecker service), reducing the number of candidates to 97. Of these, four had strong astrometric and/or photometric outliers, likely due to self-subtraction in difference images due to the unavoidable limitations of template generation from the limited quantity of data available from LSSTComCam. We suspect these four linkages do correspond to real objects, but have chosen to discard them out of an abundance of caution.

5.10. Solar System

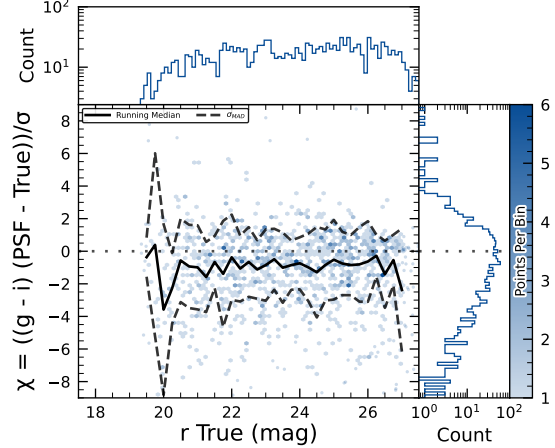
5.10.1. Asteroid Linking Performance

The evaluation of asteroid linking performance in DP1 focused on demonstrating discovery capability. The solar system discovery pipeline produced 269,581 tracklets, 5,691 linkages, and 281 post-processed candidates.

As described in §4.6.3, post-processing of the `heliolinc` output with `link_purify` produced a final set of 281 candidate linkages, ranked with the most promising first. We then used `find_orb` (B. Gray 2025) to derive orbit fits for each candidate, sorting the resulting list by χ_{dof}^2 , a measure of fit quality. A conservative manual investigation of these candidates yielded a curated list of 93 probable new asteroid discoveries. Manual

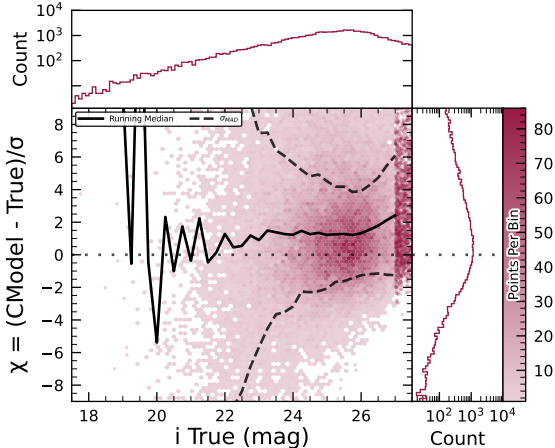


(a) i -band flux uncertainty-scaled residuals for PSF model measurements of injected stars.

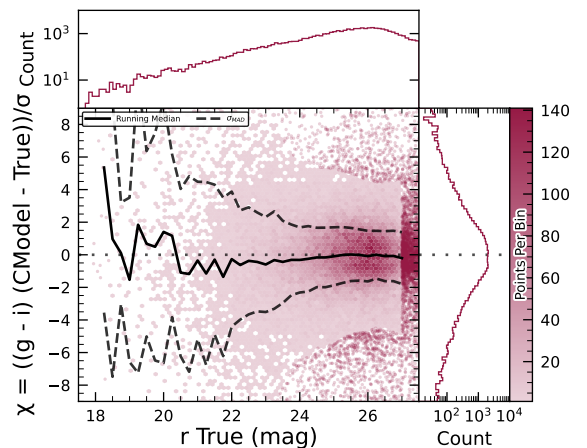


(b) $g - i$ color uncertainty-scaled residuals for PSF model measurements of injected stars.

Figure 32. Color and flux uncertainty-scaled residuals for matched injected DC2 stars' PSF model measurements in a portion of the ECDFS region.



(a) i -band flux uncertainty-scaled residuals for CModel measurements of injected galaxies.



(b) $g - i$ color uncertainty-scaled residuals for CModel measurements of injected galaxies.

Figure 33. Color and flux uncertainty-scaled residuals for matched injected DC2 galaxies' CModel measurements in a portion of the ECDFS region.

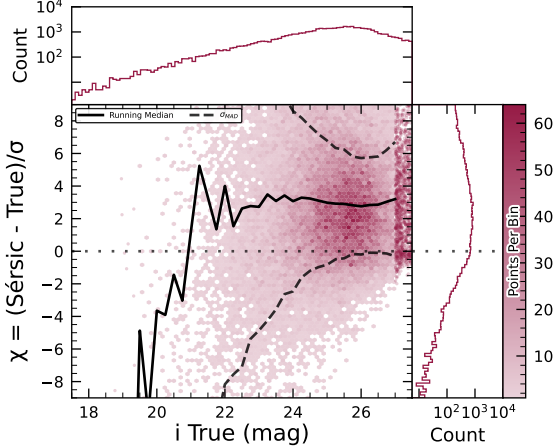
2487 dance of caution. The remaining 93 were submitted to
 2488 the Minor Planet Center and accepted as discoveries,
 2489 demonstrating the LSST pipelines are able to success-
 2490 fully discover new solar system objects.

2500 did not meet the required criteria for tracklet formation,
 2501 specifically the minimum number of detections and/or
 2502 the maximum allowed time span between observations.

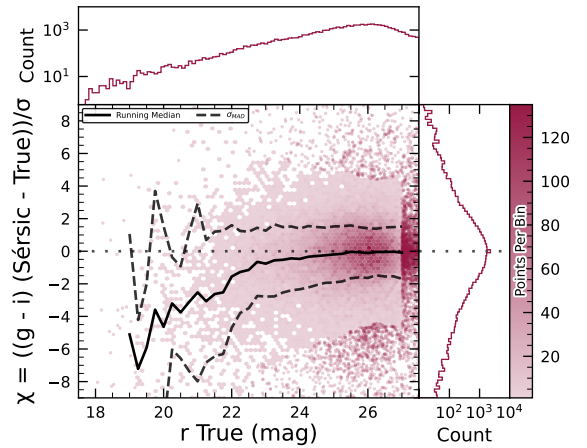
2503 The astrometric residuals of known asteroid associa-
 2504 tions are shown in Figure 38. The astrometric precision
 2505 for solar system sources is excellent, with the majority
 2506 of objects detected within $0.^{\circ}1$ of their expected posi-
 2507 tions. Taking the signed median residuals to search for
 2508 biases, we find that previously-known objects have mean
 2509 residuals of $0.^{\circ}001$ and $-0.^{\circ}016$ in the RA and Dec direc-
 2510 tions respectively, while newly-discovered objects have
 2511 mean residuals of $-0.^{\circ}035$ and $-0.^{\circ}010$ in the RA and
 2512 Dec directions, respectively. These mean residuals are
 2513 small enough to eliminate the possibility of a timing off-

2491 5.10.2. Asteroid Association Performance

2492 During the Solar System association step, 5988 *Di-*
 2493 *aSources* were linked to 431 unique Solar System ob-
 2494 jects. These include 3,934 *DiSources* with 338 previ-
 2495 ously known objects cataloged by the MPC, and 2,054
 2496 *DiSources* with the 93 newly-discovered objects. An
 2497 additional 143 detections of these newly discovered ob-
 2498 jects were also recovered. These detections were not
 2499 initially identified by the discovery pipelines, as they



(a) i -band flux uncertainty-scaled residuals for Sérsic model measurements of injected galaxies.



(b) $g-i$ color uncertainty-scaled residuals for Sérsic model measurements of injected galaxies.

Figure 34. Color and flux uncertainty-scaled residuals for matched injected DC2 galaxies’ Sérsic measurements in a portion of the [ECDFS](#) region.

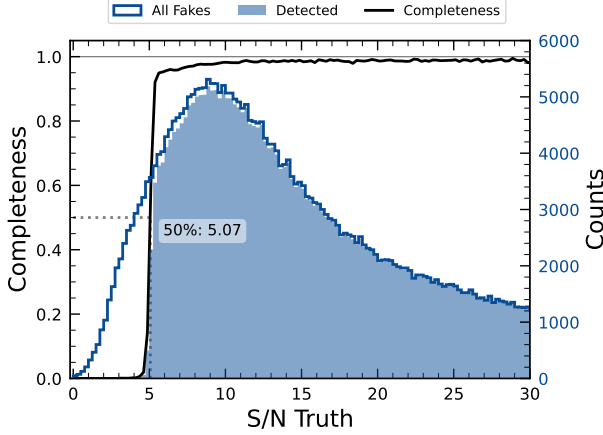


Figure 35. The difference image detection completeness for injected sources in the [ECDFS](#) field, for filters $griz$, as a function of the estimated signal to noise ratio SNR. This completeness is the ratio between the found fake sources (shaded histogram) and all the sources (solid line). The horizontal dashed line represents where the 50% completeness level is reached, at approximately $\text{SNR} \simeq 5.07$.

set greater than the second-scale shutter motion, which is consistent with the timing studies presented in Section 2.2.2.

5.11. Crowded Fields

Among the seven Rubin DP1 target fields, two stand out for their severe stellar crowding: the globular cluster 47 Tucanae (47_Tuc) and the Fornax dwarf spheroidal galaxy (Fornax dSph). These fields were selected in part to stress-test the LSST Science Pipelines under high-density conditions. While both exhibit high stellar den-

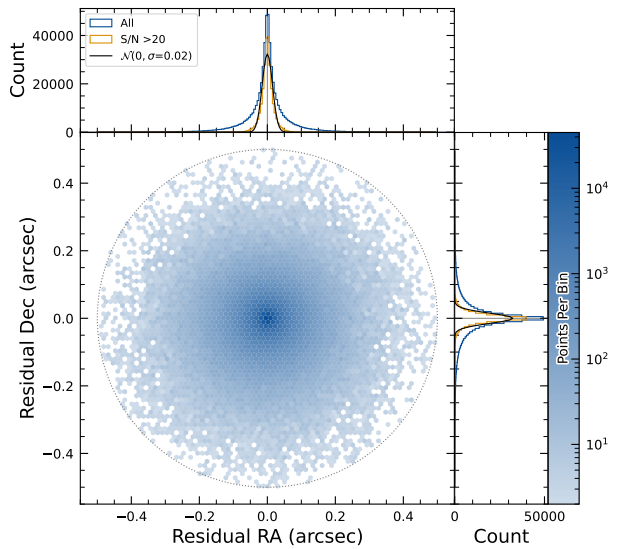


Figure 36. Coordinate residuals for detected synthetic sources in difference images, between recovered and true position of the sources in the [ECDFS](#) field. In the top and right panels we include the distribution of these offsets, for all sources as well as for sources with $\text{SNR} > 20$. These high SNR sources show gaussian coordinate residual distributions with $\sigma = 0''.02$ (black solid lines). The circle reflects the matching radius of $0''.5$.

sities, the nature and spatial extent of the crowding differ significantly.

47 Tuc presents extreme crowding across much of the field, encompassing its dense core and the eastern regions influenced by the Small Magellanic Cloud (SMC).

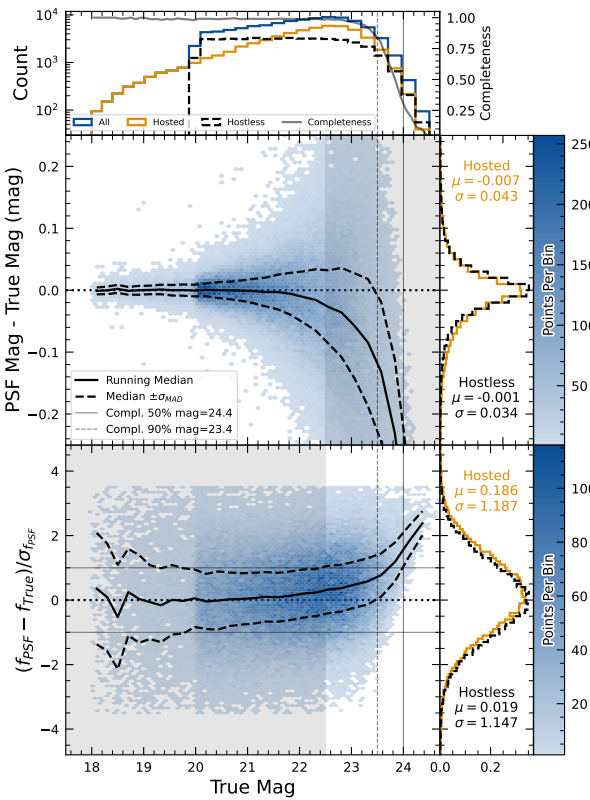


Figure 37. Magnitude residuals and flux pulls for i -band PSF photometry on difference images for ECDFS field in i for detected injected sources. Top panel: Distribution of true magnitudes for injected sources (blue), and split into hostless (black dash) and hosted (orange) sources, with detection completeness as a function of true magnitude (gray line). Vertical dashed lines indicate the 90% and 50% completeness magnitude limits. Center left panel: 2D hexbin plot of PSF magnitude residuals (measured minus true) versus true magnitude for detected sources, with running median (solid black) and σ_{MAD} (dashed black) overlaid. Center right panel: Marginalized distributions of PSF magnitude residuals for hostless (blue) and hosted (orange) sources with true magnitude $m_i < 22.5$, annotated with robust mean and standard deviation. Bottom left panel: 2D hexbin plot of PSF flux pulls versus true magnitude for detected sources, with running median (solid black) and σ_{MAD} (dashed black) overlaid. Bottom right panel: Marginalized distributions of PSF flux pulls for hostless (blue) and hosted (orange) sources with true magnitude $m_i < 22.5$, annotated with robust mean and standard deviation.

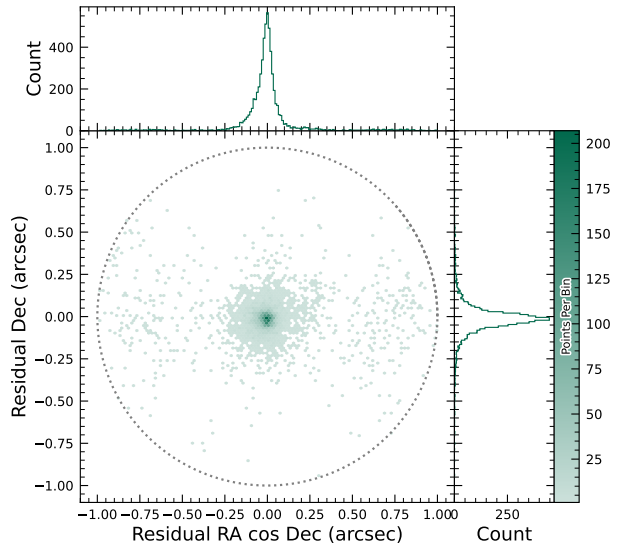


Figure 38. Astrometric residuals between expected and observed positions of Solar System Objects in DP1. The median residuals are $0.^{\prime\prime}001$ and $-0.^{\prime\prime}016$ in R.A./Dec direction, with standard deviations of $0.^{\prime\prime}19$ and $0.^{\prime\prime}10$, respectively. No detectable systematic offset from zero indicates there are no major errors in either timing or astrometry delivered by the Rubin system. The wider scatter in the RA direction is due to objects whose measured orbital elements are less well constrained, translating to larger along-track positional errors in the predicted positions.

2529 This pervasive crowding leads to persistent challenges
 2530 for deblending and reliable source detection, exposing
 2531 field-wide limitations in the current pipeline perform-
 2532 ance (Y. Choi et al. 2025). In contrast, Fornax dSph
 2533 shows significant crowding only in its central region,
 2534 with outer areas remaining well resolved and easier to
 2535 process.

2536 In both 47 Tuc and Fornax, extreme crowding led
 2537 to the deblending step being skipped frequently when
 2538 memory or runtime limits were exceeded, typically due
 2539 to an excessive number of peaks, or large parent foot-
 2540 prints. However, the impact of these limitations dif-
 2541 fered: in 47 Tuc, deblending was often skipped across the
 2542 entire field, resulting in large gaps and substantially re-
 2543 duced completeness. In Fornax, these issues were largely
 2544 confined to the central region, with much better recov-
 2545 ery in the outskirts. This contrast highlights how the
 2546 pipeline’s limitations depend on the spatial extent of
 2547 high-density regions: 47 Tuc exposed systematic, field-
 2548 wide challenges, whereas Fornax revealed more localized,
 2549 density-driven limits.

2550 T. M. Wainer et al. (2025) explored the Rubin DP1
 2551 **DiaObject** catalog (§3.2) in the 47 Tuc field, which
 2552 contains sources detected in difference images. Because
 2553 forced photometry is performed at these positions across
 2554 all single-epoch images, this dataset bypasses the coadd-
 2555 based detection and deblending stages that often fail
 2556 in crowded regions. By computing the median of the
 2557 forced photometry for each **DiaObject** across available
 2558 visits, they recovered approximately three times more
 2559 candidate cluster members than found in the standard
 2560 **Object table** (Y. Choi et al. 2025). This result un-
 2561 derscores the value of difference-imaging-based catalogs
 2562 for probing dense stellar regions inaccessible to standard
 2563 coadd processing in DP1.

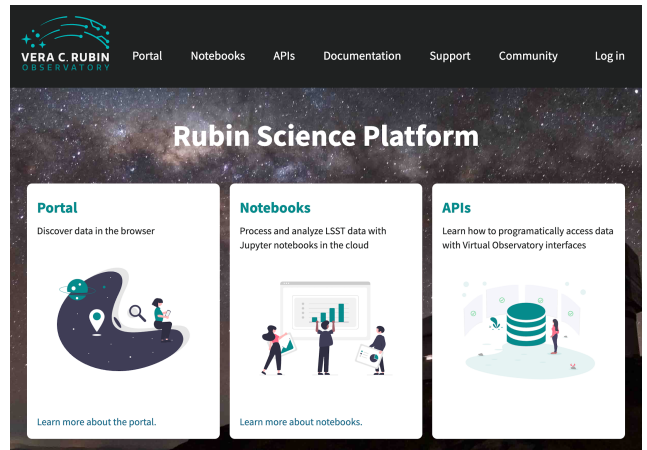
2564 Although the DP1 pipeline was not optimized for
 2565 crowded-field photometry, these early studies of 47 Tuc
 2566 and Fornax provide critical benchmarks. They highlight
 2567 both the limitations and opportunities for science with
 2568 Rubin data in crowded environments, and they inform
 2569 future pipeline development aimed at robust source re-
 2570 covery in complex stellar fields.

2571 6. RUBIN SCIENCE PLATFORM

2572 The **RSP** (M. Jurić et al. 2019) is a powerful, cloud-
 2573 based environment for scientific research and analysis
 2574 of petascale-scale astronomical survey data. It serves
 2575 as the primary interface for scientists to access, visual-
 2576 ize, and conduct next-to-the-data analysis of Rubin and
 2577 **LSST** data. The **RSP** is designed around a “bring the
 2578 compute to the data” principle, eliminating the need for
 2579 users to download massive datasets. Although **DP1** is
 2580 much smaller in size (3.5 TB) than many current sur-
 2581 vey datasets, future **LSST** datasets will be far larger and
 2582 more complex, making it crucial to co-locate data and
 2583 analysis for effective scientific discovery.

2584 The **RSP** provides users with access to data and
 2585 services through three distinct user-facing Aspects: a
 2586 *Portal*, which facilitates interactive exploration of the
 2587 data; a JupyterLab-based *Notebook* environment for
 2588 data analysis using Python; and an extensive set of
 2589 *Application Programming Interfaces (APIs)* that enable
 2590 programmatic access to both data and services. The
 2591 three Aspects are designed to be fully integrated, en-
 2592 abling seamless workflows across the **RSP**. The data
 2593 products described in §3 are accessible via all three
 2594 Aspects, and the system facilitates operations such as
 2595 starting a query in one Aspect and retrieving its results
 2596 in another. Figure 39 shows the Rubin **Science Platform**
 2597 landing page in the Google cloud.

2598 The **RSP** is supported by a number of back-end ser-
 2599 vices, including databases, files, and batch comput-



2601 **Figure 39.** The Rubin Science Platform landing page at
 2602 <https://data.lsst.cloud/> showing the three user-facing As-
 2603 pects as well as links to documentation and support infor-
 2604 mation.

2605 ing. Support for collaborative work through shared
 2606 workspaces is also included in the **RSP**.

2607 A preview of the **RSP** was launched on Google Cloud
 2608 in 2022, operating under a shared-risk model to support
 2609 **Data Preview 0** (W. O’Mullane et al. 2024a). This
 2610 allowed the community to test the platform, begin prepa-
 2611 rations for science, and provide valuable feedback to in-
 2612 form ongoing development. It was the first time an as-
 2613 tronomical research environment was hosted in a **cloud**
 2614 environment. The DP1 release brings major updates to
 2615 **RSP** services, enhancing scientific analysis capabilities.
 2616 The **RSP** remains under active development, with incre-
 2617 mental improvements being rolled out as they mature.
 2618 During the Rubin Early Science Phase, the **RSP** will
 2619 continue to operate under a shared-risk model. This
 2620 section outlines the **RSP** functionality available at the
 2621 time of the DP1 release and provides an overview of
 2622 planned future capabilities.

2623 6.1. Rubin Data Access Center

2624 The Rubin US Data Access Center (US DAC) utilizes
 2625 a novel hybrid on-premises-**cloud** architecture, which
 2626 combines on-premises infrastructure at the **USDF** at
 2627 SLAC with flexible and scalable resources in the Google
 2628 **cloud**. This architecture has been deployed and tested
 2629 using the larger simulated data set of DP0.2 (W.
 2630 O’Mullane et al. 2024b).

2631 In this hybrid model, user-facing services are deployed
 2632 in the **cloud** to support dynamic scaling in response to
 2633 user demand and to simplify the provisioning and man-
 2634 agement of large numbers of science user accounts. The
 2635 majority of the static data products described in §3 are
 2636 stored on-premises at the **USDF** to benefit from cost-
 2637 effective mass storage and close integration with Ru-

bin data processing infrastructure, also located at the [USDF](#). For imaging data, the Data Butler ([§6.2.2](#)) provides the interface between the [cloud](#)-based users and data services, and the on-premises data. For catalog data, a [cloud](#)-based [TAP](#) client ([§6.2.1](#)) submits queries to the on-premises [Qserv](#) database cluster ([§6.5](#)) and retrieves the results. In the initial DP1 deployment, catalog data is hosted at the [USDF](#) while image data is stored in the cloud. The full hybrid model will be rolled out and further tested following the release of [DP1](#). The RSP features a single-sign-on authentication and authorization system to provide secure access for Rubin data rights holders ([R. Blum & the Rubin Operations Team 2020](#)).

6.2. API Aspect

The [API](#) Aspect provides a comprehensive set of user-facing interfaces for programmatic access to the [DP1](#) data products, through both [IVOA](#)-compliant services and the Rubin Data Butler. [IVOA](#) services enable standard queries and integration with existing tools, while the Butler facilitates advanced data processing within the LSST Science Pipelines.

At the time of the [DP1](#) release, some [IVOA](#) services are unavailable, and certain data products are only accessible via the Butler. This section provides an overview of the available [IVOA](#) services and Butler access.

6.2.1. IVOA Services

Rubin has adopted a [Virtual Observatory \(VO\)](#)-first design philosophy, prioritizing compliance with [IVOA](#) standard interfaces to foster interoperability, standardization, and collaboration. In cases where standardized protocols have yet to be established, additional services have been introduced to complement these efforts. This approach ensures that the RSP can be seamlessly integrated with community-standard tools such as [Tool for Operations on Catalogues And Tables \(TOPCAT\)](#) ([M. Taylor 2011](#)) and [Aladin](#) ([F. Bonnarel et al. 2000; T. Boch & P. Fernique 2014; M. Baumann et al. 2022](#)), as well as libraries such as [PyVO](#) ([M. Graham et al. 2014](#)).

The user-facing [APIs](#) are also used internally within the [RSP](#), creating a unified design that ensures consistent and reproducible workflows across all three Aspects. This reduces code duplication, simplifies maintenance, and ensures all users, both internal and external, access data in the same way. For example, an [Astronomical Data Query Language \(IVOA standard\) \(ADQL\)](#) query on the [Object](#) catalog via [TAP](#) yields identical results whether run from the [Portal](#), [Notebook](#), or an external client.

The following [IVOA](#) services are available at the time of the DP1 release:

- **Table Access Protocol (TAP) Service:** A [TAP](#) service ([P. Dowler et al. 2019](#)) enables queries of catalog data via the [IVOA](#)-standard [ADQL](#), a dialect of [SQL92](#) with spherical geometry extensions. The main [TAP](#) service for [DP1](#) runs on the Rubin-developed [Qserv](#) database ([§ 6.5](#)), which hosts the core science tables described in [§3.2](#), as well as the [Visit](#) database. It also provides image metadata in the [IVOA](#) [ObsCore](#) format via the standard [ivoa.ObsCore](#) table, making it an “ObsTAP” service ([ObsTAP; M. Louys et al. 2017](#)). The [TAP](#) service is based on the [Canadian Astronomy Data Centre \(CADC\)](#)’s open-source Java [TAP](#) implementation¹⁰³, modified for the exact query language accepted by [Qserv](#). It currently supports a large subset of [ADQL](#), with limitations documented in the data release materials (see [§7.1](#)) and exposed via the [TAP](#) **capabilities** endpoint where possible.

The [TAP](#) service provides metadata annotations consistent with the standard, including table and column descriptions, indications of foreign-key relationships between tables, and column metadata such as units and [IVOA](#) Unified Content Descriptors (UCDs).

- **Image Access Services:** Rubin image access services are compliant with [IVOA](#) [SIAv2](#) (Simple Image Access Protocol, version 2; [T. Jenness et al. 2024; P. Dowler et al. 2015](#)) for discovering and accessing astronomical images based on [metadata](#). [SIAv2](#) is a [REpresentational State Transfer \(REST\)](#)-based protocol designed for the discovery and retrieval of image data. It allows, for instance, querying all images in a given band over a defined sky region and time period.

Users identify an image or observation of interest and query the service. The result set includes [metadata](#) about the image, such as the sky position, time, or band, and a data access URL, which includes an [IVOA](#) Identifier uniquely identifying the dataset ([T. Jenness & G. P. Dubois-Felmann 2025](#)), allowing the dataset to be retrieved or a cutout requested via [Server-side Operations for Data Access \(IVOA standard\) \(SODA\)](#).

¹⁰³ <https://github.com/opencadc/tap>

- **Image Cutout Service:** The Rubin Cutout Service (R. Allbery 2023, 2024) is based on the IVOA SODA standard (F. Bonnarel et al. 2017). Users submit requests specifying sky coordinates and the cutout size as the radius from the coordinates, and the service performs the operation on the full image and returns a result set. For DP1, the cutout service is a single cutout service only where N cutout requests will require N independent synchronous calls. We expect some form of bulk cutout service by mid 2026.
- **HiPS Data Service:** An authenticated HiPS (P. Fernique et al. 2017) data service for seamless pan-and-zoom access to large-scale co-adds. It supports fast interactive progressive image exploration at a range of resolutions.
- **WebDAV:** A Web Distributed Authoring and Versioning (WebDav) service is provided to enable users to remotely manage, edit, and organize files and directories on the RSP as if they were local files on their own computer. This is especially useful for local development.

6.2.2. Data Butler

The Rubin Data Butler (T. Jenness et al. 2022; N. B. Lust et al. 2023), is a high-level interface designed to facilitate seamless access to data for both users and software systems. This includes managing storage formats, physical locations, data staging, and database mappings. A Butler repository contains two components:

- the *Data Store*: A physical storage system for datasets, e.g., a Portable Operating System Interface (POSIX) file system or S3 object store; and
- the *Registry*: An Structured Query Language (SQL)-compatible database that stores metadata about the datasets in the data store.

For DP1, the Butler repository is hosted in the Google Cloud, using an (Amazon) Simple Storage Service (S3)-compatible store for datasets and AlloyDB, a PostgreSQL-compatible database, for the registry.

In the context of the Butler, a *dataset* refers to a unique data product, such as an image, catalog or map, generated by the observatory or processing pipelines. Datasets belong to one of the various types of data products, described in §3. The Butler ensures that each dataset is uniquely identifiable by a combination of three pieces of information: a data coordinate, a dataset type, and a run collection. For example,

Table 6. Tract coverage of each DP1 field. The size of a tract is larger than the LSSTComCam field of view; however, since each observed field extends across more than one tract, each field covers multiple tracts.

Field Code	Tract ID
47_Tuc	453, 454
ECDFS	4848, 4849, 5062, 5063, 5064
EDFS_comcam	2234, 2235, 2393, 2394
Fornax_dSph	4016, 4017, 4217, 4218
Rubin_SV_095_-25	5305, 5306, 5525, 5526
Rubin_SV_38_7	10221, 10222, 10463, 10464, 10704, 10705
Seagull	7610, 7611, 7849, 7850

a dataset that represents a single raw image in the i band taken on the night starting 2024-11-11 with exposure ID 2024111100074 would be represented as `dataId='exposure':2024111100074, 'band':'i', 'instrument':'LSSTComCam'` and is associated with the `raw` DatasetType. For a deep coadd on a `patch` of sky in the Seagull field, there would be no exposure dimensions and instead the tract, `patch` and band would be specified as `dataId='tract':7850, 'patch':6, 'band':'g', 'instrument':'LSSTComCam', skymap='lsst_cells_v1'` and is associated with the `deep_coadd` DatasetType. The tract identification numbers and corresponding target names for these tracts are listed in Table 6.

The data coordinate is used to locate a dataset in multi-dimensional space, where dimensions are defined in terms of scientifically meaningful concepts, such as instrument, visit, detector or band. For example, a calibrated single-visit image (§3.1) has dimensions including band, instrument, and detector. In contrast, the visit table (§3.2), a catalog of all calibrated single-epoch visits in DP1, has only the instrument dimension. The main dimensions used in DP1 are listed, together with a brief description, in Table 7. To determine which dimensions are relevant for a specific dataset, the Butler defines dataset types, which associate each dataset with its specific set of relevant dimensions, as well as the associated Python type representing the dataset. The dataset type defines the kind of data a dataset represents, such as a raw image (`raw`), a processed catalog (`object_forced_source`), or a sky map (`skyMap`). Table 8 lists all the dataset types available via the Butler in DP1, together with the dimensions needed to uniquely identify a specific dataset and the number of unique datasets of each type.

Table 7. Descriptions of and valid values for the key data dimensions in DP1. YYYYMMDD signifies date and # signifies a single 0–9 digit.

Dimension	Format/Valid values	Description
day_obs	YYYYMMDD	A day and night of observations that rolls over during daylight hours.
visit	YYYYMMDD#####	A sequence of observations processed together; synonymous with “exposure” in DP1.
exposure	YYYYMMDD#####	A single exposure of all nine ComCam detectors.
instrument	LSSTComCam	The instrument name.
detector	0–8	A ComCam detector.
skymap	lsst_cells_v1	A set of tracts and patches that subdivide the sky into rectangular regions with simple projections and intentional overlaps.
tract	See Table 6	A large rectangular region of the sky.
patch	0–99	A rectangular region within a tract.
physical_filter	u_02, g_01, i_06, r_03, z_03, y_04	A physical filter.
band	u, g, r, i, z, y	An conceptual astronomical passband.

2813 It is important to highlight a key difference between 2846 accessing catalog data via the [TAP](#) service versus the 2847 Butler. While the [TAP](#) service contains entire catalogs, 2848 many of the same catalogs in the Butler are split into 2849 multiple separate catalogs. This is partly due to how 2850 these catalogs are generated, but also because of the 2851 way data is stored within and retrieved from the Butler 2852 repository – it is inefficient to retrieve the entire [Source](#) 2853 catalog, for example, from the file system. Instead, 2854 because the [Source](#) catalog contains data for sources 2855 detected in the [visit_images](#), there is one [Source](#) catalog 2856 in the Butler for each [visit_image](#). Similarly, there is 2857 one [Object](#) catalog for each [deep_coadd](#). All the 2858 catalogs described in §3.2, aside from the [CcdVisit](#), [SSObject](#), 2859 [SSSource](#), and [Calibration](#) catalogs, are split 2860 within the Butler.

2861 A dataset is associated with one or more *Collections*; 2862 logical groupings of datasets within the [Butler](#) system 2863 that were created or processed together by the same 2864 batch operation. Collections allow multiple datasets 2865 with the same data coordinate to coexist without 2866 conflict. Collections support flexible, parallel processing by 2867 enabling repeated analyses of the same input data using 2868 different configurations.

2869 For [DP1](#), a subset of the consolidated database 2870 contents (§6.5.2) is accessible through the Data Butler. 2871 However, not all metadata from the [Visit](#) table (§3.5) 2872 are available. The [DP1](#) Butler is read-only; a writeable 2873 Butler is expected by mid-2026.

6.2.3. Remote Programmatic Access

2874 The Rubin [RSP API](#) can be accessed from a local 2875 system by data rights holders outside of the [RSP](#), by creat-

2876 ing a user security token. This token can then be used 2877 as a bearer token for [API](#) calls to the [RSP](#) TAP service. 2878 This capability is especially useful for remote data 2879 analysis using tools such as [TOPCAT](#), as well as enabling 2880 third-party systems, e.g., Community Alert Brokers, to 2881 access Rubin data. Additionally, it supports remote 2882 development, allowing for more flexible workflows and 2883 integration with external systems.

6.3. Portal Aspect

2884 The Portal Aspect provides an interactive web-based 2885 environment for exploratory data discovery, filtering, 2886 querying, and visualization of both image and catalog 2887 data, without requiring programming expertise. It 2888 enables users to access and analyze large datasets via tools 2889 for catalog queries, image browsing, time-series inspection, 2890 and cross-matching.

2891 The Portal is built on [Firefly](#) (X. Wu et al. 2019), 2892 a web application framework developed by the Infrared 2893 Processing and Analysis Center (IPAC). [Firefly](#) provides 2894 interactive capabilities such as customizable table views, 2895 image overlays, multi-panel visualizations, and synchronized 2896 displays linking catalog and image data.

2897 Designed to support both exploratory data access and 2898 detailed scientific investigation, the Portal delivers an 2899 intuitive user experience, allowing users to visually analyze 2900 data while retaining access to underlying metadata 2901 and query controls.

6.4. Notebook Aspect

2902 The Notebook Aspect provides an interactive, web-based 2903 environment built on Jupyter Notebooks, enabling 2904 users to write and execute Python code directly

Table 8. The name and number of each type of data product in the Butler and the dimensions required to identify a specific dataset.

Data Product	Name in Butler	Required Dimensions	Number in DP1
Image Data Products			
raw	raw	instrument, detector, exposure	16125
visit_image	visit_image	instrument, detector, visit	15972
deep_coadd	deep_coadd	band, skymap, tract, patch	2644
template_coadd	template_coadd	band, skymap, tract, patch	2730
difference_image	difference_image	instrument, detector, visit	15972
Catalog Data Products			
Source	source	instrument, visit	1786
Object	object	skymap, tract	29
ForcedSource	object_forced_source	skymap, tract, patch	636
DiaSource	dia_source	skymap, tract	25
DiaObject	dia_object	skymap, tract	25
ForcedSourceOnDiaObject	dia_object_forced_source	skymap, tract, patch	597
SSSource	ss_source	—	1
SSObject	ss_object	—	1
Visit	visit_table	instrument	1
CCDVisit	visit_detector_table	instrument	1

2877 on Rubin and [LSST](#) data without downloading it locally. 2903 It offers programmatic access to Rubin and LSST data
 2878 products, allowing users to query and retrieve datasets,
 2879 manipulate and display images, compute derived properties,
 2880 plot results, and reprocess data using the LSST
 2881 Science Pipelines ([§4.1](#)). The environment comes pre-
 2882 installed with the pipelines and a broad set of widely
 2883 used astronomical software tools, supporting immediate
 2884 and flexible data analysis.

2886 6.5. Databases

2887 The user-facing Aspects of the [RSP](#) are supported by
 2888 several backend databases that store catalog data products,
 2889 image metadata, and other derived datasets. The
 2890 schema for DP1 and other Rubin databases are available
 2891 online at <https://sdm-schemas.lsst.io>.

2892 6.5.1. *Qserv*

2893 The final 10-year [LSST](#) catalog is expected to reach
 2894 15 PB and contain measurements for billions of stars
 2895 and galaxies across trillions of detections. To support
 2896 efficient storage, querying, and analysis of this dataset,
 2897 Rubin Observatory developed Qserv (D. L. Wang et al.
 2898 2011; F. Mueller et al. 2023) – a scalable, parallel, dis-
 2899 tributed SQL database system. [Qserv](#) partitions data
 2900 over approximately equal-area regions of the celestial
 2901 sphere, replicates data to ensure resilience and high
 2902 availability, and uses shared scanning to reduce overall

2903 I/O load. It also supports a package of scientific user-
 2904 defined functions (SciSQL: <https://smonkewitz.github.io/scisql/>) simplifying complex queries involving spherical
 2905 geometry, statistics, and photometry. [Qserv](#) is built on robust production-quality components, includ-
 2906 ing MariaDB (<https://www.mariadb.org/>) and XRootD
 2907 (<https://xrootd.org/>). Qserv runs at the [USDF](#) and user
 2908 access to catalog data is via the TAP service ([§6.2.1](#)).
 2909 This enables catalog-based analysis through both the
 2910 [RSP](#) Portal and Notebook Aspects.

2911 Although the small [DP1](#) dataset does not require
 2912 Qserv’s full capabilities, we nevertheless chose to use
 2913 it for [DP1](#) to accurately reflect the future data access
 2914 environment and to gain experience with scientifically-
 2915 motivated queries ahead of full-scale deployment. [Qserv](#)
 2916 is open-source and available on GitHub: <https://github.com/lsst/qserv>.

2920 6.5.2. *Consolidated Database*

2921 The Consolidated Database (ConsDB) (K.-T. Lim
 2922 2025) is an SQL-compatible database designed to store
 2923 and manage metadata for Rubin Observatory science
 2924 and calibration images. Metadata are recorded on a per-
 2925 exposure basis and includes information such as the tar-
 2926 get name, pointing coordinates, observation time, physi-
 2927 cal filter and band, exposure duration, and environmen-
 2928 tal conditions (e.g., temperature, humidity, and wind
 2929 speed). These key image metadata are also stored in

2930 the Butler Registry (§6.2.2), however the ConsDB stores
 2931 additional information including derived metrics from
 2932 image processing and information from the [Engineering](#)
 2933 and [Facility Database \(EFD\)](#) transformed from the time
 2934 dimension to the exposure dimension.

2935 The ConsDB schema is organized into instrument-
 2936 specific tables, e.g., [LSSTComCam](#) and LSSTCam, fa-
 2937 cilitating instrument-specific queries. Within the [LSST-](#)
 2938 [ComCam](#) schema, data is further structured into ta-
 2939 bles for individual exposures and detectors. An example
 2940 query on the [DP1](#) dataset might retrieve all visits within
 2941 a specified time range in the r-band for a given [DP1](#) tar-
 2942 get.

2943 The ConsDB is hosted at the [USDF](#). Following the
 2944 initial release of DP1, a release of the DP1 exposure-
 2945 specific ConsDB data will be made available through the
 2946 [RSP](#), and accessible externally via TAP. The detailed
 2947 [LSSTComCam](#) schema can be found at: [https://sdm-](https://sdm-schemas.lsst.io/cdb_lsstcomcam.html)
 2948 [schemas.lsst.io/cdb_lsstcomcam.html](#)

2949 7. SUPPORT FOR COMMUNITY SCIENCE

2950 The Rubin Observatory has a science community that
 2951 encompasses thousands of individuals worldwide, with
 2952 a broad range of experience and expertise in astronomy
 2953 in general, and in the analysis of optical imaging data
 2954 specifically.

2955 Rubin’s model to support this diverse community to
 2956 access and analyze [DP1](#) emphasizes self-help via docu-
 2957 mentation and tutorials, and employs an open platform
 2958 for asynchronous issue reporting that enables crowd-
 2959 sourced solutions. These two aspects of community sup-
 2960 port are augmented by virtual engagement activities. In
 2961 addition, Rubin supports its Users Committee to advo-
 2962 cate on behalf of the science community, and supports
 2963 the eight [LSST](#) Science Collaborations (§7.6).

2964 All of the resources for scientists that are discussed in
 2965 this section are discoverable by browsing the For Scien-
 2966 tists pages of the Rubin Observatory website¹⁰⁴.

2967 7.1. Documentation

2968 The data release documentation for DP1¹⁰⁵ provides
 2969 an overview of the LSSTComCam observations, detailed
 2970 descriptions of the data products, and a high-level sum-
 2971 mary of the processing pipelines. Although much of its
 2972 content overlaps significantly with this paper, the doc-
 2973 umentation is presented as a searchable, web-based re-
 2974 source built using Sphinx¹⁰⁶, with a focus on enabling
 2975 scientific use of the data products.

2976 7.2. Tutorials

2977 A suite of tutorials ([N.-D. V. C. R. Observatory 2021](#))
 2978 that demonstrate how to access and analyze [DP1](#) using
 2979 the RSP accompanies the [DP1](#) release¹⁰⁷. Jupyter Note-
 2980 book tutorials are available via the “Tutorials” drop-
 2981 down menu within the Notebook aspect of the [RSP](#).
 2982 Tutorials for the Portal and API aspects of the [RSP](#) can
 2983 be found in the data release documentation.

2984 These tutorials are designed to be inclusive, accessi-
 2985 ble, clear, focused, and consistent. Their format and
 2986 contents follow a set of guidelines ([M. L. Graham et al.](#)
 2987 2025) that are informed by modern standards in techni-
 2988 cal writing.

2989 7.3. Community Forum

2990 The venue for all user support is the Rubin Commu-
 2991 nity Forum¹⁰⁸.

2992 Questions about any and all aspects of the Rubin
 2993 data products, pipelines, and services – including [DP1](#)
 2994 – should be posted as new topics in the Support cate-
 2995 gory. This includes beginner-level and “how-to” ques-
 2996 tions, advanced scientific analysis questions, technical
 2997 bug reports, account and data access issues, and every-
 2998 thing in between. The Support category of the Forum
 2999 is monitored by Rubin staff, who follow an established
 3000 internal workflow for following-up and resolving all re-
 3001 ported issues.

3002 The Rubin Community Forum is built on the open-
 3003 source Discourse platform. It was chosen because, for
 3004 a worldwide community of ten thousand Rubin users, a
 3005 traditional (i.e., closed) help desk represents a risk to
 3006 Rubin science (e.g., many users with the same question
 3007 having to wait for responses). The open nature of the
 3008 Forum enables self-help by letting users search for sim-
 3009 ilar issues, and enables crowd-sourced problem solving
 3010 (and avoids knowledge bottlenecks) by letting users help
 3011 users.

3012 The Rubin Community Forum, and the internal staff
 3013 workflows for user support, were set up, tested, and re-
 3014 fined with /glsDP0 so that it was ready for use with
 3015 [DP1](#).

3016 7.4. Engagement Activities

3017 A variety of live virtual and in-person workshops and
 3018 seminars offer learning opportunities to scientists and
 3019 students working with the Rubin data products, ser-
 3020 vices, and tools.

¹⁰⁴ <https://rubinobservatory.org/for-scientists>

¹⁰⁵ <https://dp1.lsst.io>

¹⁰⁶ <https://www.sphinx-doc.org/>

¹⁰⁷ <https://dp1.lsst.io/tutorials>

¹⁰⁸ <https://community.lsst.org/>

- Rubin Science Assemblies (weekly, virtual, 1 hour): alternates between hands-on tutorials based on the most recent data release and open drop-in “office hours” with Rubin staff.
- Rubin Data Academy (annual, virtual, 3-4 days): an intense set of hands-on tutorials based on the most recent data release, along with co-working and networking sessions.
- Rubin Community Workshop (annual, virtual, 5 days), a science-focused conference of contributed posters, talks, and sessions led by members of the Rubin science community and Rubin staff.

Following the release of [DP1](#), all of these engagement activities focused on use of [DP1](#) by the science community. In particular, the 2025 Rubin Data Academy was run the week of the [DP1](#) release, in order to immediately facilitate community access. The 2025 Rubin Community Workshop had several sessions to introduce people to the [DP1](#) dataset and demonstrate how to access and analyze it with the [RSP](#).

For schedules, connection information, zoom recordings, and associated materials, visit the For Scientists pages of the Rubin Observatory website¹⁰⁹. Requests for custom tutorials and presentations for research groups are also accommodated.

7.5. *Users Committee*

This committee is charged with soliciting feedback from the science community, advocating on their behalf, and recommending science-driven improvements to the [LSST](#) data products and the Rubin Science Platform tools and services. Community members are encouraged to attend their virtual meetings and raise issues to their attention, so they can be included in the committee’s twice-yearly reports to the Rubin Observatory Director.

Like the Forum, the Users Committee was established and began its work with [DP0](#), and that feedback was implemented for [DP1](#). The community’s response to [DP1](#) will be especially valuable input to [DP2](#) and [Data Release 1 \(DR1\)](#), and the Users Committee encourages all users to interact with them. For a list of members and contact information, visit the For Scientists pages of the Rubin Observatory website.

7.6. *Science Collaborations*

The eight [LSST](#) Science Collaborations are independent, worldwide communities of scientists, self-organized

into collaborations based on their research interests and expertise. Members work together to apply for funding, build software infrastructure and analysis algorithms, and incorporate external data sets into their [LSST](#)-based research.

The Science Collaborations also provide valuable advice to Rubin Observatory on the operational strategies and data products to accomplish specific science goals, and Rubin Observatory supports the collaborations via staff liaisons and regular virtual meetings with Rubin operations leadership.

The Science Collaborations have been functioning for many years, and their engagement and feedback on [DP0](#) was implemented into the community science model for [DP1](#), as it will for future data releases.

8. SUMMARY AND FUTURE RELEASES

[Rubin Data Preview 1 \(DP1\)](#) offers an initial look at the first on-sky data products and access services from the Vera C. Rubin Observatory. [DP1](#) forms part of Rubin’s Early Science Program, and provides the scientific community with an early opportunity to familiarize themselves with the data formats and access infrastructure for the forthcoming Legacy Survey of Space and Time. This early release has a proprietary period of two years, during which time it is available to Rubin data rights holders only via the cloud-based Rubin Science Platform ([RSP](#)).

In this paper we have described the completion status of the observatory at the time of data acquisition, the commissioning campaign that forms the basis of [DP1](#), and the processing pipelines used to produce early versions of data products. We provide details on the data products, their characteristics and known issues, and describe the Rubin Science Platform for access to and analysis of [DP1](#).

The data products described in this paper derive from observations obtained by [LSSTComCam](#). [LSSTComCam](#) contains only around 5% the number of CCDs as the full LSST Science Camera (LSSTCam), yet the [DP1](#) dataset that it has produced will already enable a very broad range of science. At 3.5 TB in size, [DP1](#) covers a total area of $\sim 15 \text{ deg}^2$ and contains 1792 single-epoch images, 2644 deep coadded images and 2.3 million distinct astrophysical objects, including 93 new asteroid discoveries.

While some data products anticipated from the [LSST](#) are not yet available, e.g., cell-based coadds, [DP1](#) includes several products that will not be provided in future releases. Notably, difference images are included in [DP1](#) as pre-generated products; in future releases, these will instead be generated on demand via dedicated ser-

¹⁰⁹ <https://rubinobservatory.org/for-scientists/events-deadlines>

3118 vices. The inclusion of pre-generated difference images
 3119 in DP1 is feasible due to the relatively small size of the
 3120 dataset, an approach that will not scale to the signifi-
 3121 cantly larger data volumes expected in subsequent re-
 3122 leases.

3123 The [RSP](#) is continually under development, and new
 3124 functionality will continue to be deployed incrementally
 3125 as it becomes available, and independent of the future
 3126 data release schedule. User query history capabilities,
 3127 context-aware documentation and a bulk cutout services
 3128 are just a few of the services currently under develop-
 3129 ment.

3130 Coincident with the release of DP1, Rubin Obser-
 3131 vatory begins its Science Validation Surveys with the
 3132 LSST Science Camera. This final commissioning phase
 3133 will produce a dataset that will form the foundation for
 3134 the second Rubin Data Preview, [DP2](#). Full operations,
 3135 marking the start of the [LSST](#), are expected to com-
 3136 mence in 2026.

ACKNOWLEDGMENTS

3137 . This material is based upon work supported in part by
 3138 the National Science Foundation through Cooperative
 3139 Agreements AST-1258333 and AST-2241526 and Co-
 3140 operative Support Agreements AST-1202910 and AST-
 3141 2211468 managed by the Association of Universities for
 3142 Research in Astronomy (AURA), and the Department of
 3143

3144 Energy under Contract No. DE-AC02-76SF00515 with
 3145 the SLAC National Accelerator Laboratory managed
 3146 by Stanford University. Additional Rubin Observatory
 3147 funding comes from private donations, grants to univer-
 3148 sities, and in-kind support from LSST-DA Institutional
 3149 Members.

3150 This work has been supported by the French Na-
 3151 tional Institute of Nuclear and Particle Physics (IN2P3)
 3152 through dedicated funding provided by the National
 3153 Center for Scientific Research (CNRS).

3154 This work has been supported by STFC fund-
 3155 ing for UK participation in LSST, through grant
 3156 ST/Y00292X/1.

3157 *Facilities:* Rubin:Simonyi (LSSTComCam), Ru-
 3158 bin:USDAC

3159 *Software:* Rubin Data Butler ([T. Jenness et al.](#)
 3160 2022), LSST Science Pipelines ([Rubin Observatory Sci-](#)
 3161 [ence Pipelines Developers 2025](#)), LSST Feature Based
 3162 Scheduler v3.0 ([P. Yoachim et al. 2024](#); [E. Naghib et al.](#)
 3163 2019) Astropy ([Astropy Collaboration et al. 2013, 2018,](#)
 3164 2022) PIFF ([M. Jarvis et al. 2021](#)), GBDES ([G. M.](#)
 3165 [Bernstein 2022](#)), Qserv ([D. L. Wang et al. 2011](#); [F.](#)
 3166 [Mueller et al. 2023](#)), Slurm, HTCondor, CVMFS, FTS3,
 3167 ESNet

APPENDIX

REFERENCES

3169 Abazajian, K., Adelman-McCarthy, J. K., Agüeros, M. A.,
 3170 et al. 2004, AJ, 128, 502, doi: [10.1086/421365](https://doi.org/10.1086/421365)

3171 Ahumada, R., Allende Prieto, C., Almeida, A., et al. 2020,
 3172 ApJS, 249, 3, doi: [10.3847/1538-4365/ab929e](https://doi.org/10.3847/1538-4365/ab929e)

3173 Aihara, H., AlSayyad, Y., Ando, M., et al. 2022, PASJ, 74,
 3174 247, doi: [10.1093/pasj/psab122](https://doi.org/10.1093/pasj/psab122)

3175 Allbery, R. 2023, IVOA SODA implementation experience,
 3176 SQuaRE Technical Note SQR-063, NSF-DOE Vera C.
 3177 Rubin Observatory. <https://sqr-063.lsst.io/>

3178 Allbery, R. 2024, Draft IVOA SODA web service
 3179 specification, SQuaRE Technical Note SQR-093,
 3180 NSF-DOE Vera C. Rubin Observatory.
 3181 <https://sqr-093.lsst.io/>

3182 AlSayyad, Y. 2018, Coaddition Artifact Rejection and
 3183 CompareWarp, Data Management Technical Note
 3184 DMTN-080, NSF-DOE Vera C. Rubin Observatory,
 3185 doi: [10.71929/rubin/2583441](https://doi.org/10.71929/rubin/2583441)

3186 Ansel, J., Yang, E., He, H., et al. 2024, in 29th ACM
 3187 International Conference on Architectural Support for
 3188 Programming Languages and Operating Systems, Volume
 3189 2 (ASPLOS '24) (ACM), doi: [10.1145/3620665.3640366](https://doi.org/10.1145/3620665.3640366)

3190 Antilogus, P., Astier, P., Doherty, P., Guyonnet, A., &
 3191 Regnault, N. 2014, Journal of Instrumentation, 9,
 3192 C03048, doi: [10.1088/1748-0221/9/03/C03048](https://doi.org/10.1088/1748-0221/9/03/C03048)

3193 Astropy Collaboration, Robitaille, T. P., Tollerud, E. J.,
 3194 et al. 2013, A&A, 558, A33,
 3195 doi: [10.1051/0004-6361/201322068](https://doi.org/10.1051/0004-6361/201322068)

3196 Astropy Collaboration, Price-Whelan, A. M., Sipőcz, B. M.,
 3197 et al. 2018, AJ, 156, 123, doi: [10.3847/1538-3881/aabc4f](https://doi.org/10.3847/1538-3881/aabc4f)

3198 Astropy Collaboration, Price-Whelan, A. M., Lim, P. L., et al. 2022, ApJ, 935, 167, doi: [10.3847/1538-4357/ac7c74](https://doi.org/10.3847/1538-4357/ac7c74)

3199 Baumann, M., Boch, T., Pineau, F.-X., et al. 2022, in Astronomical Society of the Pacific Conference Series, Vol. 532, Astronomical Data Analysis Software and Systems XXX, ed. J. E. Ruiz, F. Pierfederici, & P. Teuben, 7

3200 Bechtol, K., Sevilla-Noarbe, I., Drlica-Wagner, A., et al. 2025, arXiv e-prints, arXiv:2501.05739, doi: [10.48550/arXiv.2501.05739](https://doi.org/10.48550/arXiv.2501.05739)

3201 Berk, A., Anderson, G. P., Bernstein, L. S., et al. 1999, in Society of Photo-Optical Instrumentation Engineers (SPIE) Conference Series, Vol. 3756, Optical Spectroscopic Techniques and Instrumentation for Atmospheric and Space Research III, ed. A. M. Larar, 348–353, doi: [10.1117/12.366388](https://doi.org/10.1117/12.366388)

3202 Bernstein, G. M. 2022, gbdes: DECam instrumental signature fitting and processing programs,, Astrophysics Source Code Library, record ascl:2210.011 <http://ascl.net/2210.011>

3203 Bernstein, G. M., & Jarvis, M. 2002, AJ, 123, 583, doi: [10.1086/338085](https://doi.org/10.1086/338085)

3204 Bernstein, G. M., Armstrong, R., Plazas, A. A., et al. 2017, PASP, 129, 074503, doi: [10.1088/1538-3873/aa6c55](https://doi.org/10.1088/1538-3873/aa6c55)

3205 Bertin, E. 2011, in Astronomical Society of the Pacific Conference Series, Vol. 442, Astronomical Data Analysis Software and Systems XX, ed. I. N. Evans, A. Accomazzi, D. J. Mink, & A. H. Rots, 435

3206 Bianco, F. B., Ivezić, Ž., Jones, R. L., et al. 2022, ApJS, 258, 1, doi: [10.3847/1538-4365/ac3e72](https://doi.org/10.3847/1538-4365/ac3e72)

3207 Blum, R., & the Rubin Operations Team. 2020, Vera C. Rubin Observatory Data Policy, Data Management Operations Controlled Document RDO-013, NSF-DOE Vera C. Rubin Observatory. <https://ls.st/RDO-013>

3208 Boch, T., & Fernique, P. 2014, in Astronomical Society of the Pacific Conference Series, Vol. 485, Astronomical Data Analysis Software and Systems XXIII, ed. N. Manset & P. Forshay, 277

3209 Bonnarel, F., Dowler, P., Demleitner, M., Tody, D., & Dempsey, J. 2017, IVOA Server-side Operations for Data Access Version 1.0., IVOA Recommendation 17 May 2017 doi: [10.5479/ADS/bib/2017ivoa.spec.0517B](https://doi.org/10.5479/ADS/bib/2017ivoa.spec.0517B)

3210 Bonnarel, F., Fernique, P., Bienaymé, O., et al. 2000, A&AS, 143, 33, doi: [10.1051/aas:2000331](https://doi.org/10.1051/aas:2000331)

3211 Bosch, J., Armstrong, R., Bickerton, S., et al. 2018, PASJ, 70, S5, doi: [10.1093/pasj/pss080](https://doi.org/10.1093/pasj/pss080)

3212 Broughton, A., Utsumi, Y., Plazas Malagón, A. A., et al. 2024, PASP, 136, 045003, doi: [10.1088/1538-3873/ad3aa2](https://doi.org/10.1088/1538-3873/ad3aa2)

3213 Burke, D. L., Rykoff, E. S., Allam, S., et al. 2018, AJ, 155, 41, doi: [10.3847/1538-3881/aa9f22](https://doi.org/10.3847/1538-3881/aa9f22)

3214 Chambers, K. C., Magnier, E. A., Metcalfe, N., et al. 2016, arXiv e-prints, arXiv:1612.05560, doi: [10.48550/arXiv.1612.05560](https://doi.org/10.48550/arXiv.1612.05560)

3215 Choi, Y., Olsen, K. A. G., Carlin, J. L., et al. 2025, arXiv e-prints, arXiv:2507.01343, doi: [10.48550/arXiv.2507.01343](https://doi.org/10.48550/arXiv.2507.01343)

3216 de Vaucouleurs, G. 1948, Annales d’Astrophysique, 11, 247

3217 de Vaucouleurs, G. 1953, MNRAS, 113, 134, doi: [10.1093/mnras/113.2.134](https://doi.org/10.1093/mnras/113.2.134)

3218 Dowler, P., Bonnarel, F., & Tody, D. 2015, IVOA Simple Image Access Version 2.0., IVOA Recommendation 23 December 2015 doi: [10.5479/ADS/bib/2015ivoa.spec.1223D](https://doi.org/10.5479/ADS/bib/2015ivoa.spec.1223D)

3219 Dowler, P., Rixon, G., Tody, D., & Demleitner, M. 2019, Table Access Protocol Version 1.1., IVOA Recommendation 27 September 2019 doi: [10.5479/ADS/bib/2019ivoa.spec.0927D](https://doi.org/10.5479/ADS/bib/2019ivoa.spec.0927D)

3220 Eggli, S., Juric, M., Moeyens, J., & Jones, L. 2020, in AAS/Division for Planetary Sciences Meeting Abstracts, Vol. 52, AAS/Division for Planetary Sciences Meeting Abstracts, 211.01

3221 Esteves, J. H., Utsumi, Y., Snyder, A., et al. 2023, PASP, 135, 115003, doi: [10.1088/1538-3873/ad0a73](https://doi.org/10.1088/1538-3873/ad0a73)

3222 Euclid Collaboration, Romelli, E., Kümmel, M., et al. 2025, arXiv e-prints, arXiv:2503.15305, doi: [10.48550/arXiv.2503.15305](https://doi.org/10.48550/arXiv.2503.15305)

3223 Fagrelius, P., & Rykoff, E. S. 2025, Rubin Observatory Baseline Calibration Plan, Commissioning Technical Note SITCOMTN-086, NSF-DOE Vera C. Rubin Observatory, doi: [10.71929/rubin/2583850](https://doi.org/10.71929/rubin/2583850)

3224 Ferguson, P. S., Rykoff, E. S., Carlin, J. L., Saunders, C., & Parejko, J. K. 2025, The Monster: A reference catalog with synthetic ugrizy-band fluxes for the Vera C. Rubin observatory, Data Management Technical Note DMTN-277, NSF-DOE Vera C. Rubin Observatory, doi: [10.71929/rubin/2583688](https://doi.org/10.71929/rubin/2583688)

3225 Fernique, P., Allen, M. G., Boch, T., et al. 2015, A&A, 578, A114, doi: [10.1051/0004-6361/201526075](https://doi.org/10.1051/0004-6361/201526075)

3226 Fernique, P., Allen, M., Boch, T., et al. 2017, HiPS - Hierarchical Progressive Survey Version 1.0., IVOA Recommendation 19 May 2017 doi: [10.5479/ADS/bib/2017ivoa.spec.0519F](https://doi.org/10.5479/ADS/bib/2017ivoa.spec.0519F)

3227 Fortino, W. F., Bernstein, G. M., Bernardinelli, P. H., et al. 2021, AJ, 162, 106, doi: [10.3847/1538-3881/ac0722](https://doi.org/10.3847/1538-3881/ac0722)

3228 Gaia Collaboration, Montegriffo, P., Bellazzini, M., et al. 2023a, A&A, 674, A33, doi: [10.1051/0004-6361/202243709](https://doi.org/10.1051/0004-6361/202243709)

3229 Gaia Collaboration, Vallenari, A., Brown, A. G. A., et al. 2023b, A&A, 674, A1, doi: [10.1051/0004-6361/202243940](https://doi.org/10.1051/0004-6361/202243940)

3297 Górski, K. M., Hivon, E., Banday, A. J., et al. 2005, ApJ,
 3298 622, 759, doi: [10.1086/427976](https://doi.org/10.1086/427976)

3299 Graham, A. W., & Driver, S. P. 2005, PASA, 22, 118,
 3300 doi: [10.1071/AS05001](https://doi.org/10.1071/AS05001)

3301 Graham, M., Plante, R., Tody, D., & Fitzpatrick, M. 2014,
 3302 PyVO: Python access to the Virtual Observatory,,
 3303 Astrophysics Source Code Library, record ascl:1402.004

3304 Graham, M. L., Carlin, J. L., Adair, C. L., et al. 2025,
 3305 Guidelines for User Tutorials, Technical Note RTN-045,
 3306 NSF-DOE Vera C. Rubin Observatory,
 3307 doi: [10.71929/rubin/2584020](https://doi.org/10.71929/rubin/2584020)

3308 Gray, B. 2025, find_orb: Orbit determination from
 3309 observations, https://github.com/Bill-Gray/find_orb

3310 Guy, L. P., Bechtol, K., Bellm, E., et al. 2026, Rubin
 3311 Observatory Plans for an Early Science Program,
 3312 Technical Note RTN-011, NSF-DOE Vera C. Rubin
 3313 Observatory, doi: [10.71929/rubin/2584021](https://doi.org/10.71929/rubin/2584021)

3314 Heinze, A., Eggel, S., Juric, M., et al. 2022, in AAS/Division
 3315 for Planetary Sciences Meeting Abstracts, Vol. 54,
 3316 AAS/Division for Planetary Sciences Meeting Abstracts,
 3317 504.04

3318 Heinze, A., Juric, M., & Kurlander, J. 2023, heliolinx: Open
 3319 Source Solar System Discovery Software,
 3320 <https://github.com/heliolinx/heliolinx>

3321 Hirata, C., & Seljak, U. 2003, MNRAS, 343, 459,
 3322 doi: [10.1046/j.1365-8711.2003.06683.x](https://doi.org/10.1046/j.1365-8711.2003.06683.x)

3323 Holman, M. J., Payne, M. J., Blankley, P., Janssen, R., &
 3324 Kuindersma, S. 2018, AJ, 156, 135,
 3325 doi: [10.3847/1538-3881/aad69a](https://doi.org/10.3847/1538-3881/aad69a)

3326 Howard, J., Reil, K., Claver, C., et al. 2018, in Society of
 3327 Photo-Optical Instrumentation Engineers (SPIE)
 3328 Conference Series, Vol. 10700, Ground-based and
 3329 Airborne Telescopes VII, ed. H. K. Marshall &
 3330 J. Spyromilio, 107003D, doi: [10.1117/12.2312684](https://doi.org/10.1117/12.2312684)

3331 Illingworth, G., Magee, D., Bouwens, R., et al. 2016, arXiv
 3332 e-prints, arXiv:1606.00841,
 3333 doi: [10.48550/arXiv.1606.00841](https://doi.org/10.48550/arXiv.1606.00841)

3334 Ingraham, P., Fagrelius, P., Stubbs, C. W., et al. 2022, in
 3335 Society of Photo-Optical Instrumentation Engineers
 3336 (SPIE) Conference Series, Vol. 12182, Ground-based and
 3337 Airborne Telescopes IX, ed. H. K. Marshall,
 3338 J. Spyromilio, & T. Usuda, 121820R,
 3339 doi: [10.1117/12.2630185](https://doi.org/10.1117/12.2630185)

3340 Ivezić, Ž., Kahn, S. M., Tyson, J. A., et al. 2019a, ApJ,
 3341 873, 111, doi: [10.3847/1538-4357/ab042c](https://doi.org/10.3847/1538-4357/ab042c)

3342 Ivezić, Ž., Kahn, S. M., Tyson, J. A., et al. 2019b, ApJ,
 3343 873, 111, doi: [10.3847/1538-4357/ab042c](https://doi.org/10.3847/1538-4357/ab042c)

3344 Jarvis, M., et al. 2021, Mon. Not. Roy. Astron. Soc., 501,
 3345 1282, doi: [10.1093/mnras/staa3679](https://doi.org/10.1093/mnras/staa3679)

3346 Jenness, T., & Dubois-Felsmann, G. P. 2025, IVOA
 3347 Identifier Usage at the Rubin Observatory, Data
 3348 Management Technical Note DMTN-302, NSF-DOE Vera
 3349 C. Rubin Observatory, doi: [10.71929/rubin/2583848](https://doi.org/10.71929/rubin/2583848)

3350 Jenness, T., Voutsinas, S., Dubois-Felsmann, G. P., &
 3351 Salnikov, A. 2024, arXiv e-prints, arXiv:2501.00544,
 3352 doi: [10.48550/arXiv.2501.00544](https://doi.org/10.48550/arXiv.2501.00544)

3353 Jenness, T., Bosch, J. F., Salnikov, A., et al. 2022, in
 3354 Society of Photo-Optical Instrumentation Engineers
 3355 (SPIE) Conference Series, Vol. 12189, Software and
 3356 Cyberinfrastructure for Astronomy VII, 1218911,
 3357 doi: [10.1117/12.2629569](https://doi.org/10.1117/12.2629569)

3358 Jones, R. L., Yoachim, P., Ivezić, Ž., Neilsen Jr., E. H., &
 3359 Ribeiro, T. 2021, Survey Strategy and Cadence Choices
 3360 for the Vera C. Rubin Observatory Legacy Survey of
 3361 Space and Time (LSST), Project Science Technical Note
 3362 PSTN-051, NSF-DOE Vera C. Rubin Observatory,
 3363 doi: [10.71929/rubin/2584084](https://doi.org/10.71929/rubin/2584084)

3364 Juric, M. 2025, mpsky: Multi-purpose sky catalog
 3365 cross-matching, <https://github.com/mjuric/mpsky>

3366 Jurić, M., Ciardi, D., Dubois-Felsmann, G., & Guy, L.
 3367 2019, LSST Science Platform Vision Document, Systems
 3368 Engineering Controlled Document LSE-319, NSF-DOE
 3369 Vera C. Rubin Observatory, doi: [10.71929/rubin/2587242](https://doi.org/10.71929/rubin/2587242)

3370 Jurić, M., Axelrod, T. S., Becker, A. C., et al. 2023, Data
 3371 Products Definition Document, Systems Engineering
 3372 Controlled Document LSE-163, NSF-DOE Vera C. Rubin
 3373 Observatory, doi: [10.71929/rubin/2587118](https://doi.org/10.71929/rubin/2587118)

3374 Kannawadi, A. 2025, Consistent galaxy colors with
 3375 Gaussian-Aperture and PSF photometry, Data
 3376 Management Technical Note DMTN-190, NSF-DOE Vera
 3377 C. Rubin Observatory, doi: [10.71929/rubin/2583849](https://doi.org/10.71929/rubin/2583849)

3378 Kron, R. G. 1980, ApJS, 43, 305, doi: [10.1086/190669](https://doi.org/10.1086/190669)

3379 Kuijken, K. 2008, A&A, 482, 1053,
 3380 doi: [10.1051/0004-6361:20066601](https://doi.org/10.1051/0004-6361:20066601)

3381 Lange, T., Nordby, M., Pollek, H., et al. 2024, in Society of
 3382 Photo-Optical Instrumentation Engineers (SPIE)
 3383 Conference Series, Vol. 13096, Ground-based and
 3384 Airborne Instrumentation for Astronomy X, ed. J. J.
 3385 Bryant, K. Motohara, & J. R. D. Vernet, 130961O,
 3386 doi: [10.1117/12.3019302](https://doi.org/10.1117/12.3019302)

3387 Léget, P. F., Astier, P., Regnault, N., et al. 2021, A&A,
 3388 650, A81, doi: [10.1051/0004-6361/202140463](https://doi.org/10.1051/0004-6361/202140463)

3389 Lim, K.-T. 2023, Proposal and Prototype for Prompt
 3390 Processing, Data Management Technical Note
 3391 DMTN-219, NSF-DOE Vera C. Rubin Observatory,
 3392 doi: [10.71929/rubin/2585429](https://doi.org/10.71929/rubin/2585429)

3393 Lim, K.-T. 2025, The Consolidated Database of Image
 3394 Metadata, Data Management Technical Note
 3395 DMTN-227, NSF-DOE Vera C. Rubin Observatory,
 3396 doi: [10.71929/rubin/2586436](https://doi.org/10.71929/rubin/2586436)

3397 Louys, M., Tody, D., Dowler, P., et al. 2017, Observation
 3398 Data Model Core Components, its Implementation in the
 3399 Table Access Protocol Version 1.1., IVOA
 3400 Recommendation 09 May 2017
 3401 doi: [10.5479/ADS/bib/2017ivoa.spec.0509L](https://doi.org/10.5479/ADS/bib/2017ivoa.spec.0509L)

3402 LSST Dark Energy Science Collaboration (LSST DESC),
 3403 Abolfathi, B., Alonso, D., et al. 2021, ApJS, 253, 31,
 3404 doi: [10.3847/1538-4365/abd62c](https://doi.org/10.3847/1538-4365/abd62c)

3405 Lupton, R., Blanton, M. R., Fekete, G., et al. 2004, PASP,
 3406 116, 133, doi: [10.1086/382245](https://doi.org/10.1086/382245)

3407 Lust, N. B., Jenness, T., Bosch, J. F., et al. 2023, arXiv
 3408 e-prints, arXiv:2303.03313,
 3409 doi: [10.48550/arXiv.2303.03313](https://doi.org/10.48550/arXiv.2303.03313)

3410 Mandelbaum, R., Hirata, C. M., Seljak, U., et al. 2005,
 3411 MNRAS, 361, 1287,
 3412 doi: [10.1111/j.1365-2966.2005.09282.x](https://doi.org/10.1111/j.1365-2966.2005.09282.x)

3413 Megias Homar, G., Kahn, S. M., Meyers, J. M., Crenshaw,
 3414 J. F., & Thomas, S. J. 2024, The Astrophysical Journal,
 3415 974, 108, doi: [10.3847/1538-4357/ad6cdc](https://doi.org/10.3847/1538-4357/ad6cdc)

3416 Megias Homar, G., Tighe, R., Thomas, S., et al. 2024, in
 3417 Ground-based and Airborne Telescopes X, ed. H. K.
 3418 Marshall, J. Spyromilio, & T. Usuda, Vol. 13094,
 3419 International Society for Optics and Photonics (SPIE),
 3420 130943C, doi: [10.1117/12.3019031](https://doi.org/10.1117/12.3019031)

3421 Melchior, P., Moolekamp, F., Jerdee, M., et al. 2018,
 3422 Astronomy and Computing, 24, 129,
 3423 doi: [10.1016/j.ascom.2018.07.001](https://doi.org/10.1016/j.ascom.2018.07.001)

3424 Mueller, F., et al. 2023, in ASP Conf. Ser., Vol. TBD,
 3425 ADASS XXXII, ed. S. Gaudet, S. Gwyn, P. Dowler,
 3426 D. Bohlender, & A. Hincks (San Francisco: ASP), in
 3427 press. <https://dmtn-243.lsst.io>

3428 Naghib, E., Yoachim, P., Vanderbei, R. J., Connolly, A. J.,
 3429 & Jones, R. L. 2019, The Astronomical Journal, 157, 151,
 3430 doi: [10.3847/1538-3881/aafece](https://doi.org/10.3847/1538-3881/aafece)

3431 NSF-DOE Vera C. Rubin Observatory. 2025a, Legacy
 3432 Survey of Space and Time Data Preview 1 [Data set],
 3433 NSF-DOE Vera C. Rubin Observatory,
 3434 doi: [10.71929/RUBIN/2570308](https://doi.org/10.71929/RUBIN/2570308)

3435 NSF-DOE Vera C. Rubin Observatory. 2025b, Legacy
 3436 Survey of Space and Time Data Preview 1: raw dataset
 3437 type [Data set], NSF-DOE Vera C. Rubin Observatory,
 3438 doi: [10.71929/RUBIN/2570310](https://doi.org/10.71929/RUBIN/2570310)

3439 NSF-DOE Vera C. Rubin Observatory. 2025c, Legacy
 3440 Survey of Space and Time Data Preview 1: visit_image
 3441 dataset type [Data set], NSF-DOE Vera C. Rubin
 3442 Observatory, doi: [10.71929/RUBIN/2570311](https://doi.org/10.71929/RUBIN/2570311)

3443 NSF-DOE Vera C. Rubin Observatory. 2025d, Legacy
 3444 Survey of Space and Time Data Preview 1: deep_coadd
 3445 dataset type [Data set], NSF-DOE Vera C. Rubin
 3446 Observatory, doi: [10.71929/RUBIN/2570313](https://doi.org/10.71929/RUBIN/2570313)

3447 NSF-DOE Vera C. Rubin Observatory. 2025e, Legacy
 3448 Survey of Space and Time Data Preview 1:
 3449 template_coadd dataset type [Data set], NSF-DOE Vera
 3450 C. Rubin Observatory, doi: [10.71929/RUBIN/2570314](https://doi.org/10.71929/RUBIN/2570314)

3451 NSF-DOE Vera C. Rubin Observatory. 2025f, Legacy
 3452 Survey of Space and Time Data Preview 1:
 3453 difference_image dataset type [Data set], NSF-DOE Vera
 3454 C. Rubin Observatory, doi: [10.71929/RUBIN/2570312](https://doi.org/10.71929/RUBIN/2570312)

3455 NSF-DOE Vera C. Rubin Observatory. 2025g, Legacy
 3456 Survey of Space and Time Data Preview 1: Source
 3457 searchable catalog [Data set], NSF-DOE Vera C. Rubin
 3458 Observatory, doi: [10.71929/RUBIN/2570323](https://doi.org/10.71929/RUBIN/2570323)

3459 NSF-DOE Vera C. Rubin Observatory. 2025h, Legacy
 3460 Survey of Space and Time Data Preview 1: Object
 3461 searchable catalog [Data set], NSF-DOE Vera C. Rubin
 3462 Observatory, doi: [10.71929/RUBIN/2570325](https://doi.org/10.71929/RUBIN/2570325)

3463 NSF-DOE Vera C. Rubin Observatory. 2025i, Legacy
 3464 Survey of Space and Time Data Preview 1: ForcedSource
 3465 searchable catalog [Data set], NSF-DOE Vera C. Rubin
 3466 Observatory, doi: [10.71929/RUBIN/2570327](https://doi.org/10.71929/RUBIN/2570327)

3467 NSF-DOE Vera C. Rubin Observatory. 2025j, Legacy
 3468 Survey of Space and Time Data Preview 1: DiaSource
 3469 searchable catalog [Data set], NSF-DOE Vera C. Rubin
 3470 Observatory, doi: [10.71929/RUBIN/2570317](https://doi.org/10.71929/RUBIN/2570317)

3471 NSF-DOE Vera C. Rubin Observatory. 2025k, Legacy
 3472 Survey of Space and Time Data Preview 1: DiaObject
 3473 searchable catalog [Data set], NSF-DOE Vera C. Rubin
 3474 Observatory, doi: [10.71929/RUBIN/2570319](https://doi.org/10.71929/RUBIN/2570319)

3475 NSF-DOE Vera C. Rubin Observatory. 2025l, Legacy
 3476 Survey of Space and Time Data Preview 1:
 3477 ForcedSourceOnDiaObject searchable catalog [Data set],
 3478 NSF-DOE Vera C. Rubin Observatory,
 3479 doi: [10.71929/RUBIN/2570321](https://doi.org/10.71929/RUBIN/2570321)

3480 NSF-DOE Vera C. Rubin Observatory. 2025m, Legacy
 3481 Survey of Space and Time Data Preview 1: SSOBJect
 3482 searchable catalog [Data set], NSF-DOE Vera C. Rubin
 3483 Observatory, doi: [10.71929/RUBIN/2570335](https://doi.org/10.71929/RUBIN/2570335)

3484 NSF-DOE Vera C. Rubin Observatory. 2025n, Legacy
 3485 Survey of Space and Time Data Preview 1: SSSource
 3486 searchable catalog [Data set], NSF-DOE Vera C. Rubin
 3487 Observatory, doi: [10.71929/RUBIN/2570333](https://doi.org/10.71929/RUBIN/2570333)

3488 NSF-DOE Vera C. Rubin Observatory. 2025o, Legacy
 3489 Survey of Space and Time Data Preview 1: CcdVisit
 3490 searchable catalog [Data set], NSF-DOE Vera C. Rubin
 3491 Observatory, doi: [10.71929/RUBIN/2570331](https://doi.org/10.71929/RUBIN/2570331)

3492 NSF-DOE Vera C. Rubin Observatory. 2025p, Legacy
 3493 Survey of Space and Time Data Preview 1: survey
 3494 property dataset type [Data set], NSF-DOE Vera C.
 3495 Rubin Observatory, doi: [10.71929/RUBIN/2570315](https://doi.org/10.71929/RUBIN/2570315)

3496 Observatory, N.-D. V. C. R. 2021, Rubin Observatory
 3497 LSST Tutorials [Computer Software], NSF-DOE Vera C.
 3498 Rubin Observatory, doi: [10.11578/rubin/dc.20250909.20](https://doi.org/10.11578/rubin/dc.20250909.20)

3499 Oke, J. B., & Gunn, J. E. 1983, *ApJ*, 266, 713,
 3500 doi: [10.1086/160817](https://doi.org/10.1086/160817)

3501 O'Mullane, W., Economou, F., Huang, F., et al. 2024a, in
 3502 Astronomical Society of the Pacific Conference Series,
 3503 Vol. 535, Astromical Data Analysis Software and Systems
 3504 XXXI, ed. B. V. Hugo, R. Van Rooyen, & O. M.
 3505 Smirnov, 227, doi: [10.48550/arXiv.2111.15030](https://doi.org/10.48550/arXiv.2111.15030)

3506 O'Mullane, W., AlSayyad, Y., Chiang, J., et al. 2024b, in
 3507 Society of Photo-Optical Instrumentation Engineers
 3508 (SPIE) Conference Series, Vol. 13101, Software and
 3509 Cyberinfrastructure for Astronomy VIII, ed. J. Ibsen &
 3510 G. Chiozzi, 131012B, doi: [10.1117/12.3018005](https://doi.org/10.1117/12.3018005)

3511 Onken, C. A., Wolf, C., Bessell, M. S., et al. 2019, *PASA*,
 3512 36, e033, doi: [10.1017/pasa.2019.27](https://doi.org/10.1017/pasa.2019.27)

3513 Park, H. Y., Nomerotski, A., & Tsybychev, D. 2017,
 3514 *Journal of Instrumentation*, 12, C05015,
 3515 doi: [10.1088/1748-0221/12/05/C05015](https://doi.org/10.1088/1748-0221/12/05/C05015)

3516 Petrosian, V. 1976, *ApJL*, 210, L53,
 3517 doi: [10.1086/18230110.1086/182253](https://doi.org/10.1086/18230110.1086/182253)

3518 Plazas, A. A., Shapiro, C., Smith, R., Huff, E., & Rhodes,
 3519 J. 2018, *Publications of the Astronomical Society of the
 3520 Pacific*, 130, 065004, doi: [10.1088/1538-3873/aab820](https://doi.org/10.1088/1538-3873/aab820)

3521 Plazas Malagón, A. A., Digel, S. W., Roodman, A.,
 3522 Broughton, A., & LSST Camera Team. 2025, LSSTCam
 3523 and LSSTComCam Focal Plane Layouts, Camera
 3524 Technical Note CTN-001, NSF-DOE Vera C. Rubin
 3525 Observatory, doi: [10.71929/rubin/2584019](https://doi.org/10.71929/rubin/2584019)

3526 Plazas Malagón, A. A., Waters, C., Broughton, A., et al.
 3527 2025, *Journal of Astronomical Telescopes, Instruments,
 3528 and Systems*, 11, 011209,
 3529 doi: [10.1117/1.JATIS.11.1.011209](https://doi.org/10.1117/1.JATIS.11.1.011209)

3530 Refregier, A. 2003, *ARA&A*, 41, 645,
 3531 doi: [10.1146/annurev.astro.41.111302.102207](https://doi.org/10.1146/annurev.astro.41.111302.102207)

3532 Reiss, D. J., & Lupton, R. H. 2016, Implementation of
 3533 Image Difference Decorrelation, Data Management
 3534 Technical Note DMTN-021, NSF-DOE Vera C. Rubin
 3535 Observatory, doi: [10.71929/rubin/2586490](https://doi.org/10.71929/rubin/2586490)

3536 Roodman, A., Rasmussen, A., Bradshaw, A., et al. 2024, in
 3537 Society of Photo-Optical Instrumentation Engineers
 3538 (SPIE) Conference Series, Vol. 13096, Ground-based and
 3539 Airborne Instrumentation for Astronomy X, ed. J. J.
 3540 Bryant, K. Motohara, & J. R. D. Vernet, 130961S,
 3541 doi: [10.1117/12.3019698](https://doi.org/10.1117/12.3019698)

3542 Rubin, V. C., & Ford, Jr., W. K. 1970, *ApJ*, 159, 379,
 3543 doi: [10.1086/150317](https://doi.org/10.1086/150317)

3544 Rubin, V. C., Ford, Jr., W. K., & Thonnard, N. 1980, *ApJ*,
 3545 238, 471, doi: [10.1086/158003](https://doi.org/10.1086/158003)

3546 Rubin Observatory Science Pipelines Developers. 2025, The
 3547 LSST Science Pipelines Software: Optical Survey
 3548 Pipeline Reduction and Analysis Environment, Project
 3549 Science Technical Note PSTN-019, NSF-DOE Vera C.
 3550 Rubin Observatory, doi: [10.71929/rubin/2570545](https://doi.org/10.71929/rubin/2570545)

3551 Rubin's Survey Cadence Optimization Committee, Bauer,
 3552 F. E., Brough, S., et al. 2022, Survey Cadence
 3553 Optimization Committee's Phase 1 Recommendation,
 3554 Project Science Technical Note PSTN-053, NSF-DOE
 3555 Vera C. Rubin Observatory, doi: [10.71929/rubin/2584276](https://doi.org/10.71929/rubin/2584276)

3556 Rubin's Survey Cadence Optimization Committee, Bauer,
 3557 F. E., Bianco, F. B., et al. 2023, Survey Cadence
 3558 Optimization Committee's Phase 2 Recommendations,
 3559 Project Science Technical Note PSTN-055, NSF-DOE
 3560 Vera C. Rubin Observatory, doi: [10.71929/rubin/2585249](https://doi.org/10.71929/rubin/2585249)

3561 Rubin's Survey Cadence Optimization Committee, Bianco,
 3562 F. B., Jones, R. L., et al. 2025, Survey Cadence
 3563 Optimization Committee's Phase 3 Recommendations,
 3564 Project Science Technical Note PSTN-056, NSF-DOE
 3565 Vera C. Rubin Observatory, doi: [10.71929/rubin/2585402](https://doi.org/10.71929/rubin/2585402)

3566 Rykoff, E. S., Tucker, D. L., Burke, D. L., et al. 2023, arXiv
 3567 e-prints, arXiv:2305.01695,
 3568 doi: [10.48550/arXiv.2305.01695](https://doi.org/10.48550/arXiv.2305.01695)

3569 Saunders, C. 2024, Astrometric Calibration in the LSST
 3570 Pipeline, Data Management Technical Note DMTN-266,
 3571 NSF-DOE Vera C. Rubin Observatory,
 3572 doi: [10.71929/rubin/2583846](https://doi.org/10.71929/rubin/2583846)

3573 Schutt, T., Jarvis, M., Roodman, A., et al. 2025, The Open
 3574 Journal of Astrophysics, 8, 26, doi: [10.33232/001c.132299](https://doi.org/10.33232/001c.132299)

3575 Sérsic, J. L. 1963, Boletin de la Asociacion Argentina de
 3576 Astronomia La Plata Argentina, 6, 41

3577 Sersic, J. L. 1968, *Atlas de Galaxias Australes* (Cordoba,
 3578 Argentina: Observatorio Astronomico)

3579 Shanks, T., Metcalfe, N., Chehade, B., et al. 2015,
 3580 *MNRAS*, 451, 4238, doi: [10.1093/mnras/stv1130](https://doi.org/10.1093/mnras/stv1130)

3581 SLAC National Accelerator Laboratory, & NSF-DOE Vera
 3582 C. Rubin Observatory. 2024, LSST Commissioning
 3583 Camera, SLAC National Accelerator Laboratory (SLAC),
 3584 Menlo Park, CA (United States),
 3585 doi: [10.71929/RUBIN/2561361](https://doi.org/10.71929/RUBIN/2561361)

3586 Slater, C. T., Ivezić, Ž., & Lupton, R. H. 2020, *AJ*, 159, 65,
 3587 doi: [10.3847/1538-3881/ab6166](https://doi.org/10.3847/1538-3881/ab6166)

3588 Smith, G. E. 2010, *Rev. Mod. Phys.*, 82, 2307,
 3589 doi: [10.1103/RevModPhys.82.2307](https://doi.org/10.1103/RevModPhys.82.2307)

3590 Stalder, B., Reil, K., Claver, C., et al. 2020, in Society of
3591 Photo-Optical Instrumentation Engineers (SPIE)
3592 Conference Series, Vol. 11447, Ground-based and
3593 Airborne Instrumentation for Astronomy VIII, ed. C. J.
3594 Evans, J. J. Bryant, & K. Motohara, 114470L,
3595 doi: [10.1117/12.2561132](https://doi.org/10.1117/12.2561132)

3596 Stalder, B., Reil, K., Aguilar, C., et al. 2022, in Society of
3597 Photo-Optical Instrumentation Engineers (SPIE)
3598 Conference Series, Vol. 12184, Ground-based and
3599 Airborne Instrumentation for Astronomy IX, ed. C. J.
3600 Evans, J. J. Bryant, & K. Motohara, 121840J,
3601 doi: [10.1117/12.2630184](https://doi.org/10.1117/12.2630184)

3602 Stalder, B., Munoz, F., Aguilar, C., et al. 2024, in Society
3603 of Photo-Optical Instrumentation Engineers (SPIE)
3604 Conference Series, Vol. 13094, Ground-based and
3605 Airborne Telescopes X, ed. H. K. Marshall, J. Spyromilio,
3606 & T. Usuda, 1309409, doi: [10.1117/12.3019266](https://doi.org/10.1117/12.3019266)

3607 Swinbank, J. D., Axelrod, T. S., Becker, A. C., et al. 2020,
3608 Data Management Science Pipelines Design, Data
3609 Management Controlled Document LDM-151, NSF-DOE
3610 Vera C. Rubin Observatory, doi: [10.71929/rubin/2587108](https://doi.org/10.71929/rubin/2587108)

3611 Taranu, D. S. 2025, The MultiProFit astronomical source
3612 modelling code, Data Management Technical Note
3613 DMTN-312, NSF-DOE Vera C. Rubin Observatory,
3614 doi: [10.71929/rubin/2584108](https://doi.org/10.71929/rubin/2584108)

3615 Taylor, M. 2011, TOPCAT: Tool for Operations on
3616 Catalogues And Tables,, Astrophysics Source Code
3617 Library, record ascl:1101.010

3618 Thomas, S., Connolly, A., Crenshaw, J. F., et al. 2023, in
3619 Adaptive Optics for Extremely Large Telescopes
3620 (AO4ELT7), 67, doi: [10.13009/AO4ELT7-2023-069](https://doi.org/10.13009/AO4ELT7-2023-069)

3621 Tonry, J. L., Denneau, L., Heinze, A. N., et al. 2018, PASP,
3622 130, 064505, doi: [10.1088/1538-3873/aabadf](https://doi.org/10.1088/1538-3873/aabadf)

3623 Wainer, T. M., Davenport, J. R. A., Bellm, E. C., et al.
3624 2025, Research Notes of the American Astronomical
3625 Society, 9, 171, doi: [10.3847/2515-5172/adecef](https://doi.org/10.3847/2515-5172/adecef)

3626 Wang, D. L., Monkewitz, S. M., Lim, K.-T., & Becla, J.
3627 2011, in State of the Practice Reports, SC '11 (New
3628 York, NY, USA: ACM), 12:1–12:11,
3629 doi: [10.1145/2063348.2063364](https://doi.org/10.1145/2063348.2063364)

3630 Waters, C. Z., Magnier, E. A., Price, P. A., et al. 2020,
3631 ApJS, 251, 4, doi: [10.3847/1538-4365/abb82b](https://doi.org/10.3847/1538-4365/abb82b)

3632 Whitaker, K. E., Ashas, M., Illingworth, G., et al. 2019,
3633 ApJS, 244, 16, doi: [10.3847/1538-4365/ab3853](https://doi.org/10.3847/1538-4365/ab3853)

3634 Wu, X., Roby, W., Goldian, T., et al. 2019, in Astronomical
3635 Society of the Pacific Conference Series, Vol. 521,
3636 Astronomical Data Analysis Software and Systems
3637 XXVI, ed. M. Molinaro, K. Shortridge, & F. Pasian, 32

3638 Xin, B., Claver, C., Liang, M., et al. 2015, ApOpt, 54,
3639 9045, doi: [10.1364/AO.54.009045](https://doi.org/10.1364/AO.54.009045)

3640 Yoachim, P. 2022, Survey Strategy: Rolling Cadence,
3641 Project Science Technical Note PSTN-052, NSF-DOE
3642 Vera C. Rubin Observatory, doi: [10.71929/rubin/2584109](https://doi.org/10.71929/rubin/2584109)

3643 Yoachim, P., Jones, L., Eric H. Neilsen, J., & Becker, M. R.
3644 2024, lsst/rubin_scheduler: v3.0.0, v3.0.0 Zenodo,
3645 doi: [10.5281/zenodo.13985198](https://doi.org/10.5281/zenodo.13985198)

3646 Zhang, T., Almoubayyed, H., Mandelbaum, R., et al. 2023,
3647 MNRAS, 520, 2328, doi: [10.1093/mnras/stac3350](https://doi.org/10.1093/mnras/stac3350)